CHAPTER 31

Carbon Black

Manfred Klüppel*, Andreas Schröder†, and Gert Heinrich‡

*Deutsches Institut für Kautschuktechnologie eV, Eupener Str. 33, D-30519 Hannover, Germany
†Rheinchemie Rheinan GmbH, Düsseldorfer str. 23–27, D-68219 Mannheim, Germany
‡Leibniz Institut für Polymerforschung Dresden eV, Hohe Str. 6, D-01069 Dresden, Germany

31.1 INTRODUCTION

Carbon black (c.b.) plays an important role in the improvement of the mechanical and/or electrical properties of high performance rubber materials. The reinforcing potential is mainly attributed to two effects: (i) the formation of a physically bonded flexible filler network and (ii) strong polymer filler couplings. Both of these effects refer to a high surface activity and specific surface of the filler particles [1–3].

So far, the formation and structure of the c.b. network and the mechanical response is not fully understood. Considerable progress has been obtained in the past in relating the pronounced drop of the elasticity modulus with increasing dynamical strain (Payne effect) to a cyclic breakdown and reagglomeration of filler–filler bonds [3–6]. Thereby, different geometrical arrangements of particles in a particular filler network structures, resulting e.g., from percolation [6] or kinetic cluster–cluster aggregation [7–9], have been considered. Nevertheless, a full micromechanical description of energy storage and -dissipation in reinforced rubbers is still outstanding. Reviews of the different attempts are given in [10,11] (see also Chapter ''Reinforcement Theories'' of this book).

Useful hints concerning the structure and properties of conducting c.b. networks in elastomers can be obtained from examinations of the electrical percolation threshold and the dielectric properties in a broad frequency range [8,11–13]. In particular, the percolation threshold decreases with increasing specific surface and/or structure of the c.b. particles and decreasing compatibility between polymer and filler. This emphasizes the role of the mean particle distance or gap size between particles or particle clusters. It refers to a thermally activated hopping of charge carriers across the gaps that governs the conductivity of c.b. filled polymers above the percolation threshold [11–13].

The dielectric properties are closely related to the hopping conductivity mechanism, as well. At low frequencies a delayed charge carrier motion across the gaps that may also be combined with a polarization of dead ends of the c.b. network leads to extraordinary high values of the relative dielectric constant (permittivity) $\varepsilon' \cong 10^3$–10^4. With increasing frequencies a polarization transition takes place and the permittivity falls off drastically [14]. At high frequencies the permittivity approaches a low plateau value and the conductivity σ' increases according to a power law. The conductivity exponent in the high frequency regime can be related to the anomalous diffusion exponent on fractal c.b. clusters [11–13].

For a deeper understanding of the mechanical and electrical properties of c.b. filled rubbers it is necessary to consider the morphology of the c.b. particles (primary aggregates) more closely. Due to the disordered nature of c.b. formation during processing in a furnace reactor, the morphology of furnace blacks is well described by referring to a fractal analysis. Recent investigations of the surface roughness of c.b. by static gas adsorption point out that all furnace

blacks exhibit a pronounced surface roughness with an almost unique surface fractal dimension $D_s \approx 2.6$ on atomic length scales below 6 nm [15]. This universality can be related to a particular random deposition mechanism of carbon nuclei on the particles that governs the surface growth of the particles during processing [16]. It will be considered more closely in the following two sections. According to the universal surface roughness of furnace blacks independent of grade number one can expect that the reinforcing potential and electrical effects owing to the surface roughness of c.b. are similar.

Specific effects of the different grades of furnace blacks on the mechanical and electrical properties result mainly from differences in the specific surface and/or structure of the primary aggregates. The specific surface depends strongly on the size of the primary particles and differs from about $10\,m^2/g$ up to almost $200\,m^2/g$. The structure of the primary aggregates describes the amount of void volume and is measured e.g., by oil (DBP) absorption. It typically varies between $0.3\,cm^3/g$ and $1.7\,cm^3/g$ for furnace blacks [1]. The typical shape of c.b. aggregates is illustrated in Fig. 31.1, where transmission electron micrographs (TEM) of three different grades of furnace blacks (N220, N330, N550) are shown. The various sizes of the primary particles, increasing from top to bottom, become apparent. It implies a decline of the specific surface from $113\,m^2/g$ for N220, $83\,m^2/g$ for N330 up to $39\,m^2/g$ for N550. The structure or amount of specific voids of the three grades is almost the same and differs between $1\,cm^3/g$ and $1.2\,cm^3/g$, only [8]. Since the specific weight of c.b. is almost twice of that for DBP, this corresponds to a factor two for the void volume as compared to the solid volume of the aggregates. It means that about 2/3 of the aggregate volume is empty space, i.e., the solid fraction $\phi_{A,1}$ of the primary aggregates is relative small ($\phi_{A,1} \approx 0.33$). It is shown in [8,11] that $\phi_{A,1}$ fulfills a scaling relation which involves the size and mass fractal dimension of the primary aggregates. Due to the significant deviation of the solid fraction $\phi_{A,1}$ from one, the filler volume fraction ϕ has to be treated as an effective one in most applications, i.e., $\phi_{eff} = \phi/\phi_{A,1}$.

The fractal nature of the primary c.b. aggregates and flocculated clusters can be quantified by TEM-techniques [1] or dielectric measurements [8,11]. A further technique that gives information about the morphological arrangement of filler particles in elastomers is small angle X-ray scattering (SAXS). Figure 31.2 shows results of scattering investigations obtained for natural rubber (NR) samples filled with different c.b. grades of varying specific surface. The concentration of c.b. is kept constant (46 phr). The double logarithmic plot in Fig. 31.2 demonstrates that in all cases two scaling regimes are obtained. For small values of the scattering vector q the slope is larger than -3, indicating that the scattering is initiated by mass fractals. The mass fractal dimension D_f equals the negative value of the slope β ($D_f = -\beta$). It is found to vary between $D_f \approx 2.1$–2.4. This is in fair agreement with TEM-estimates for the primary aggregates [1,8]. The lower cut off length L_c is obtained from the cross-over points of Fig. 31.2 and increases some what with decreasing specific surface ($50\,nm < L_c < 80\,nm$). Its value is of the order of the primary particle diameters, which appears reasonable since the primary particles represent the smallest units of the primary aggregates.

For large values of q the slope β in Fig. 31.2 is almost constant and smaller than -3. This refers to a surface scattering by the filler particles. Accordingly, the surface fractal dimension $D_s = 6 + \beta$ is found to be almost independent of specific surface ($D_s \approx 2.5$). This is evaluated in the length scale regime between 60 nm and 20 nm, roughly.

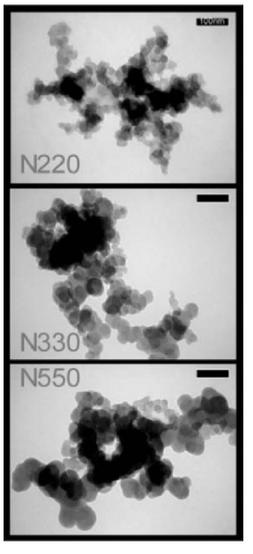

FIGURE 31.1. Transmission electron micrographs (TEM) of three different grades of furnace blacks (N220, N330, N550). The bar indicates a size of 100 nm. Reprinted from [11] with kind permission of Springer Science + Business Media.

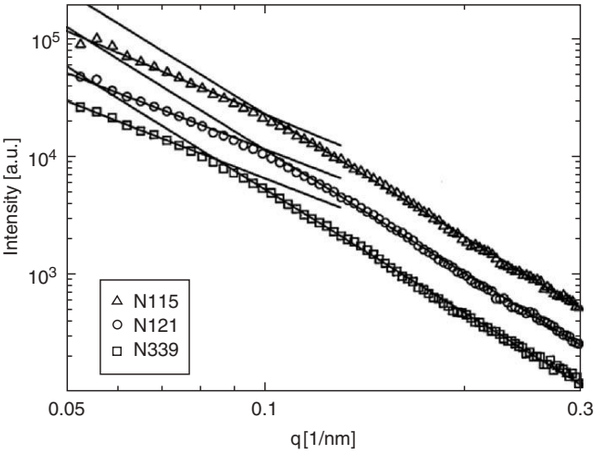

FIGURE 31.2. SAXS-data for the carbon black grades N115, N121, and N339.

It compares to scattering results investigated in [17]. Note however, that for smaller length scales at about 6 nm one observes again a cross-over of the scattering intensity. Hence, the surface fractal dimension $D_s \approx 2.5$ is related to the surface roughness on a mesoscopic length scale regime and doesn't reflect the surface roughness on atomic length scales, as obtained, e.g., by gas adsorption technique [15].

31.2 SURFACE ROUGHNESS FROM STATIC GAS ADSORPTION

In this section we will demonstrate in some detail, how the surface roughness of c.b. aggregates can be estimated by gas adsorption techniques in the mono- and multilayer regime. For this purpose, a classical volumetric adsorption apparatus equipped with absolute capacitance pressure transducers has been used for the estimation of adsorption isotherms in the pressure range $10^{-3}\,\text{mbar} < p < 10^{3}\,\text{mbar}$. Before adsorption measurements the c.b. samples were extracted with toluene and water/methanol (1:1) and after drying degassed at 300°C at a pressure below 10^{-4} mbar overnight. The time allowed for equilibrium of each point of the isotherm was between five and ninety minutes depending on the sample and the adsorbed amount.

For the morphological surface characterization in the monolayer regime we refer to a variation of the estimated BET-surface area with the size of adsorbed probe molecules (yardstick method). On smooth flat surfaces the BET-area is independent of the adsorbed probe size or applied yardstick, while on rough surfaces it decreases with increasing probe (yardstick) size due to the inability of the large molecules to explore smaller cavities. This behavior is shown schematically in Fig. 31.3. A closer analysis shows that in the case of c.b. a power law behavior of the BET-surface area with varying yardstick size is observed, indicating a self-similar structure of the c.b. surface. Double logarithmic ''yardstick-plots'' of the BET-monolayer amount N_m vs. cross-section σ of the probe molecules are shown in Fig. 31.4 for the original furnace black N220 and a graphitized (T = 2,500 °C) sample N220g. It demonstrates that the roughness exponent or surface fractal dimension D_s differs for the two c.b. samples. By using the relation introduced by Mandelbrot [18]:

$$N_m \sim \sigma^{-\frac{D_s}{2}} \tag{31.1}$$

one obtains from the slopes of the two regression lines of Fig. 31.4 a surface fractal dimension $D_s \approx 2.56$ for the N220-sample and $D_s \approx 2.32$ for the graphitized N220g sample. An extrapolation of both regression lines yields an intersection at an ultimate cross-section that corresponds to a yardstick length of about 1 nm, indicating that graphitization reduces the roughness of c.b. on small length scales below 1 nm, only. Figure 31.4 also demonstrates that the reduction of BET-surface area due to graphitization is length scale (yardstick) dependent, proving that it is related to a change of surface morphology and not e.g., a result of reduced energetic surface activity.

An important point in the above evaluation of c.b. surface morphology is the correct estimation of the cross-section σ of the applied probe molecules. This is done by referring to the mass density ρ of the probe molecules in the bulk liquid state that are considered as spheres in a hexagonal close packing:

$$\sigma = 1.091\left(\frac{M}{N_A \rho}\right)^{2/3}. \tag{31.2}$$

Here, M is the molar mass of the probe molecules and N_A is the Avogadro number. Note that any other close packing of

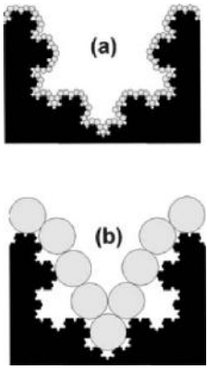

FIGURE 31.3. Schematic presentation of a fractal surface covered with monolayers of (a) small and (b) large gas molecules, demonstrating the impact of the yardstick on the estimated surface area. Reprinted from [11] with kind permission of Springer Science + Business Media.

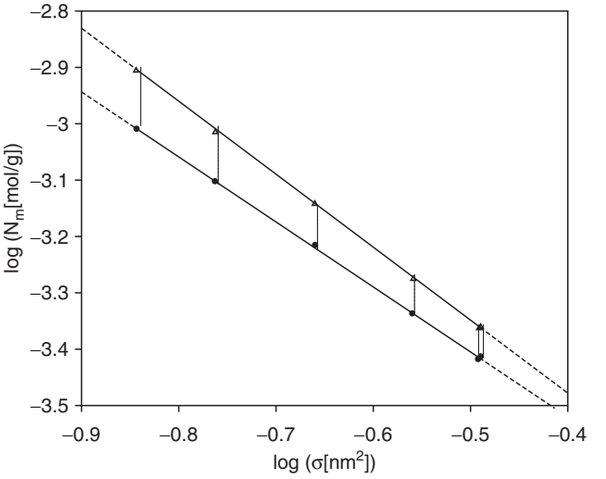

FIGURE 31.4. Yardstick-plot of N220 (△) and a graphitized N220g (●) with adsorption cross section σ determined from the bulk liquid density ρ according to Equ. (31.2); Applied gasses are: 1 argon, 2 methane, 3 ethane, 4 propane, 5 isobutane, 6 *n*-butane; The slopes yield for N220: $D_s = 2.56 \pm 0.04$, for N220g: $D_s = 2.32 \pm 0.03$. Reprinted from [11] with kind permission of Springer Science + Business Business Media.

probe molecules can be used since it doesn't alter the scaling exponent 2/3 of Eqn. (31.2). The crucial point is the temperature dependence of ρ that differ for the different probe molecules, mainly due to variations in the characteristic temperatures, e.g., the evaporation points.

It was found [15] that Eq. (31.2) can be applied without further corrections and high correlation coefficients of the "yardstick-plots" in Figs. 31.4 and 31.5 are obtained, only if: (i) the temperature during the adsorption experiments is chosen according to the theory of corresponding states and (ii) a series of chemically similar gases is used. Fig. 31.5 shows that for the same c.b. (N220g) a different scaling factor is obtained for the "yardstick-plots", if the adsorption temperatures are chosen with respect to different reference pressures, i.e., the evaporation temperatures at $p_0 = 10^3$ mbar and $p_0 = 10^4$ mbar, respectively. A different scaling factor is also observed in Fig. 31.5 for the two homological series of gases, i.e., the alkanes and alkenes, respectively. However, the scaling exponent and hence the surface fractal dimension $D_s \approx 2.3$ is unaffected by the choice of the reference pressure or applied series of adsorption gases.

An alternative approach to the characterization of surface morphology of c.b. is the consideration of film formation of adsorbed molecules in the multilayer regime. In this case, the surface roughness is evaluated with respect to a fractal extension of the classical Frenkel-, Halsey-, Hill (FHH)-theory, where beside the van der Waals surface potential the vapor–liquid surface tension has to be taken into account [19,20]. Then the Helmholtz free energy of the adsorbed film is given as the sum of the van der Waals attraction potential of all molecules in the film with all atoms in the adsorbent, the vapor–liquid surface free energy and the free energy of all molecules in the bulk liquid film. This leads to

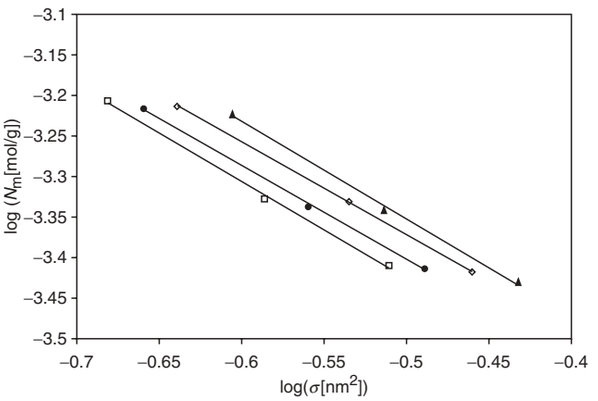

FIGURE 31.5. Yardstick-plots of the graphitized black N220g obtained with alkenes (ethylene, propylene, isobutylene) (hollow symbols) and alkanes (ethane, propane, isobutane) (filled symbols); Adsorption temperatures are chosen as evaporation points at vapor pressures $p_0 \approx 1{,}000$ mbar (lower curves) and $p_0 \approx 1{,}000$ mbar (upper curves) of the condensed gases, respectively. Reprinted from [11] with kind permission of Springer Science + Business Media.

the following relation between the adsorbed amount N and the relative pressure p/p_0 [19,20]:

$$N \sim \left(ln\frac{p_0}{p}\right)^{-\vartheta}$$

with:

$$\vartheta = \frac{3 - D_s}{3} \quad \text{FHH-regime} \tag{31.3a}$$

$$\vartheta = 3 - D_s. \quad \text{CC-regime} \tag{31.3b}$$

The different exponents for the FHH- and capillary condensation (CC)-regime consider the two cases where adsorption is dominated by the van der Waals potential and the vapor–liquid surface tension, respectively. Note that in the CC-regime a flat vapor–liquid surface is obtained due to a minimization of curvature by the surface tension. In the FHH-regime the vapor–liquid surface is curved, since it is located on equipotential lines of the van der Waals potential with constant distance to the adsorbent surface.

At low relative pressures p/p_0 or thin adsorbate films, adsorption is expected to be dominated by the van der Waals attraction of the adsorbed molecules due to the solid potential that falls off with the third power of the distance to the surface (FHH-regime, Eq. (31.3a)). At higher relative pressures p/p_0 or thick adsorbate films the adsorbed amount N is expected to be determined by the surface tension γ of the adsorbate vapor interface (CC-regime, Eq. (31.3b)), because the corresponding surface potential falls off less rapidly with the first power of the distance to the surface, only. The cross-over length $z_{\text{crit.}}$ between both regimes depends on the number density n, the surface tension γ, the van der Waals interaction parameter α as well as on the surface fractal dimension D_s [19,20]:

$$z_{\text{crit.}} = \sqrt{\frac{\alpha n}{(D_s - 2)\gamma}}. \tag{31.4}$$

Note, that the cross-over length $z_{\text{crit.}}$ decreases with increasing surface fractal dimension D_s, implying that the FHH-regime may not be observed on very rough surfaces, i.e., the film formation may be governed by the surface tension γ on all length scales $z > a$ (compare Fig. 31.7).

The film thickness z is related to the surface relative coverage N/N_m and the mean thickness $a \approx 0.35$ nm of one layer of nitrogen molecules [21] according to the scaling law [18]:

$$\frac{N}{N_m} = \left(\frac{z}{a}\right)^{3-D_s} \tag{31.5}$$

The monolayer amount N_m can be estimated from a classical BET-plot and hence the film thickness z can be obtained directly from the adsorbed amount N if the surface fractal dimension D_s is known.

So called FHH-plots of the nitrogen adsorption isotherms at 77 K of two graphitized furnace blacks are shown in Fig. 31.6. The graphitized furnace blacks have three linear

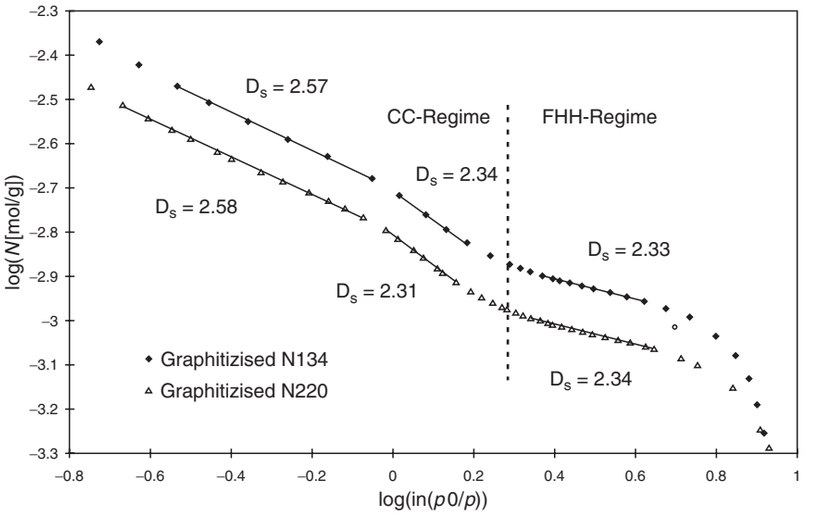

FIGURE 31.6. FHH-plot of nitrogen adsorption isotherms at 77 K for the two graphitized blacks N134g and N220g.

ranges. Starting from low pressures the first linear range is fitted by Eq. (31.3a), because the film is not very thick and the van der Waals attraction of the molecules by the solid governs the adsorption process (FHH-regime). With rising pressure, at a critical film thickness of about $z_{\text{crit.}} \approx 0.5$ nm, the vapor–liquid surface tension γ becomes dominant and a second linear range appears that is fitted according to Eq. (31.3b). The fractal FHH-theory claims almost identical fractal dimensions of $D_s \approx 2.3$ for both linear regimes up to a length scale of $z \approx 1$ nm. At this length scale a geometrical cut-off appears and the surface becomes rougher. In the final linear regime ($z > 1$ nm) the fractal dimension takes the value $D_s \approx 2.6$ (CC-regime). This linear range has an upper cut off length of approximately $z \approx 6$ nm.

Figure 31.7 shows that, contrary to the graphitized blacks, the untreated furnace blacks have only one linear range with a fractal dimension of $D_s \approx 2.6$ (CC-regime, Eq. (31.3b)). Obviously the van der Waals attraction can be neglected and the surface tension γ controls the adsorption process on all length scales. This is due to the larger surface fractal dimension D_s as compared to the graphitized furnace blacks that shifts the cross-over length $z_{\text{crit.}}$ to smaller values (Eq. (31.4)). Assuming that the number density n, the surface tension γ of the adsorbate and the van der Waals interaction parameter α are approximately the same for a nitrogen adsorbate film on graphitized and untreated furnace blacks, a cross-over length of $z_{\text{crit.}} \approx 0.35$ nm can be estimated from Eq. (31.4) with the experimental values of the fractal

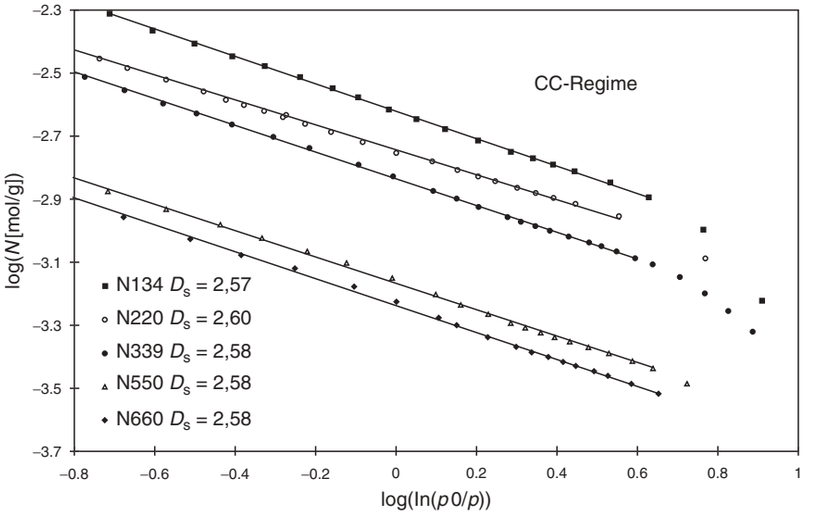

FIGURE 31.7. FHH-plot of nitrogen adsorption isotherms at 77 K for several furnace blacks. Reprinted from [11] with kind permission of Springer Science + Business Media.

dimensions and the crossover length $z_{\text{crit.}} \approx 0.5\,\text{nm}$ on a graphitized c.b. The value $z_{\text{crit.}} \approx 0.35\,\text{nm}$ is already in the range of the detection limit given by the layer thickness $a \approx 0.35$ nm. Hence, the nitrogen adsorption on furnace c.b.s is dominated by the vapor–liquid surface tension on all length scales and a cross over between the FHH- and the CC-regime does not appear. More details of these investigations are found in [15,22,23].

It must be noted that these results obtained by a rigorous gas adsorption analysis are not contradictory to recent small angle X-ray scattering results [17,24,25] that indicate a nonuniversal surface roughness of furnace blacks with significantly smaller values for D_s. The scattering results were obtained in a complementary length scale regime for scattering vectors $q < 1\,\text{nm}^{-1}$. This corresponds to length scales larger than about 6 nm. Below this length scale the scattering data show a cross-over to a different scaling behavior indicative for sheet like structures consistent with graphitic layers [24]. Obviously, on atomic length scales smaller than 6 nm the scattering from the surface is shielded by that of the graphitic crystallite structures.

In the following we present a hypothetical mechanism of c.b. formation that explains the universal value $D_s \approx 2.6$ of c.b. surface topography on atomic length scales. The model is based on physical concepts of disordered surface growth, which were recently applied in many different fields in nature.

31.3 SURFACE GROWTH DURING CARBON BLACK FORMATION

The morphology of c.b. is closely related to the conditions of surface and primary aggregate growth during c.b. processing, which is now discussed in some detail. Figure 31.8 shows a schematic representation of c.b. formation in a furnace reactor, where a jet of gas and oil is combusted and quenched, afterwards. Beside the aggregate growth, resulting from the collision of neighboring aggregates, surface growth due to the deposition of carbon nuclei on the aggregates takes place during the formation of primary c.b. aggregates. Due to the high temperature in the reactor, aggregate as well as surface growth take place under ballistic conditions, i.e., the mean free path length of both growth mechanisms is large compared to the characteristic size of the resulting structures [11,32]. Then the trajectories of colliding aggregates (or nuclei) can be considered to be linear. Numerical simulations of ballistic cluster-cluster aggregation yield a mass fractal dimension $D_f \approx 1.9$–1.95 [37]. This prediction is somewhat smaller than the SAXS-result shown in Fig.31.2. However, the assumption of ballistic cluster–cluster aggregation during c.b. processing should hold only in the asymptotic limit of large aggregates and for the relatively fine blacks. For the more coarse blacks, with a typically small primary particle number, finite size effects can lead to a more compact morphology that differs from the scaling prediction of ballistic cluster aggregation. A further deviation can result from electrostatic repulsion effects due to the application of processing agents (alkali metal ions) for designing the coarse blacks.

It is a challenging problem to model chemical and physical phenomena that take place in a few milliseconds of the c.b. formation process. These processes go so quickly from a hydrocarbon with a few carbon atoms to an aggregate made of several millions of carbon atoms. This is a kind of gaseous–solid phase transition where the solid phase exhibits no unique chemical and physical structure. The c.b.

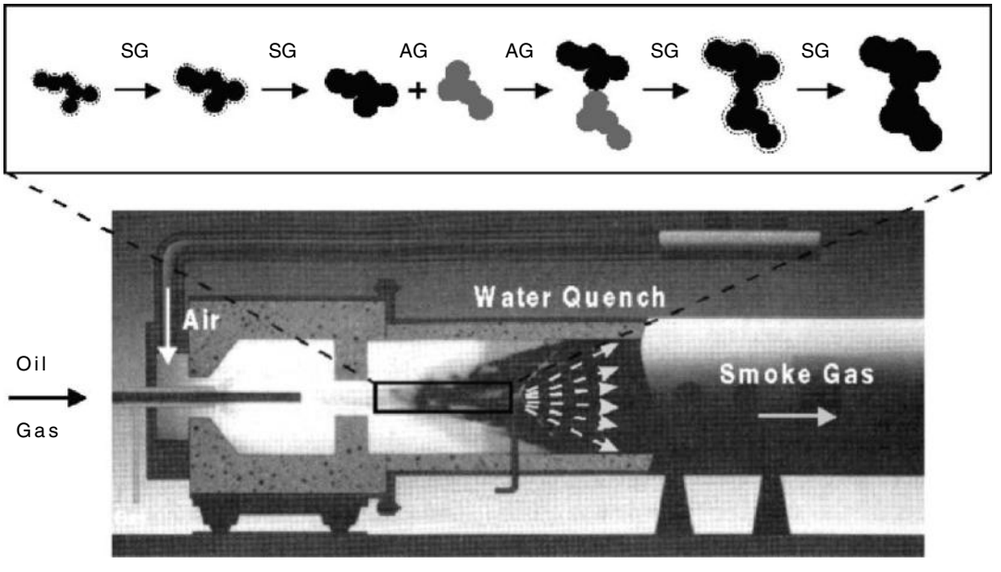

FIGURE 31.8. Schematic view of c.b. processing in a furnace reactor. Primary aggregates are built by two simultaneous growth processes: (i) surface growth (SG) and (ii) aggregate growth (AG). Reprinted from [11] with kind permission of Springer Science + Business Media.

or soot formation[1] mechanism generally described can be summarized by the following steps [26–30]: inception (nucleation), growth (by picking up growth components from the gas phase through c.b. inelastic collision and deposition), and oxidation. It is believed that either fullerenes or fullerene precursors could play an important role in c.b. black formation, especially in the inception step [29,30]. Note that recent studies on the formation of c.b. have even resulted in finding of fullerene (C60) in trace quantities in the toluene extractable materials [31]. High-resolution transmission electron microscopy experiments indicate the molecule may be functioning as a nucleation site in the formation of primary particles of c.b. [31]. The inception of c.b. particles is a key process in c.b. formation. The hydrocarbon fuel in premixed flames is degraded during oxidation into small hydrocarbon radicals from which, under fuel-rich conditions, small hydrocarbon molecules, particular acetylene are formed. The latter adds hydrocarbon radicals for growth and the growing unsaturated (radicalic) hydrocarbons form aromatic rings when containing a sufficiently large number of carbon atoms. The formation of larger aromatic rings occurs mainly via the addition of acetylene. All these processes occur within molecular length scales.

However, only ~5–10% of the c.b. mass is produced during the inception step. The remaining ~90–95% of the total yield is due to surface growth rather than soot inception, i.e., the deposition of carbonaceous species on c.b. particles that have already been formed [26,27]. Mostly it is assumed that particle growth is similar to formation of Polycyclic Aromatic Hydrocarbons (PAH), i.e., addition of acetylene and, probably, aromatics. The problem in this connection is that surface growth is not a gas-phase reaction of small molecules, but a heterogeneous process, where adsorption and desorption processes at the surface have to be considered as well [32]. Some phenomenological approaches are found in the literature (see, for example [32], Section 18.4); However, the corresponding growth rate parameters are empirical fits, and their simple structure does not reveal the underlying mechanisms. Especially, for interpretations of the ''deactivation'' of the soot surface a really convincing physical explanation is not yet available [32]. We note here, that in the physical well founded ballistic deposition model, that we propose here, ''deactivation'' can be easily explained as a kind of surface relaxation which will be explained later.

By using phase-contrast electron microscopy, it appears that surface growth occurs on both individual particles and on the aggregates formed by collision of the individual particles [26]. From this reason, the surface growth is also responsible for the stability of the primary aggregates, since it proceeds in the contact range of the collided aggregates implying a strong bonding by sinter bridges (compare Fig. 31.8). Accordingly, the bonds between neighboring particles of a primary c.b. aggregate are not stabilized by weak short-range forces, but by a continuous carbon network. Surface growth contributes to the major part to the final c.b. concentration in soothing flames while coagulation – switching the length scales to particle dimension – determines the final size of the c.b. particles.

A comparison with deposit models and simulation results of disordered growth processes that might appear during c.b. processing can provide a deeper physical background for an explanation of the universal value $D_s \approx 2.6$ of c.b. surface topography [33]. The models are based on physical concepts of surface growth, which were recently applied in many different fields in nature. Deposition models are classified, for example, in [34–37]. The simplest are ''random deposition'', ''random deposition with surface diffusion'', and ''ballistic deposition''. In all these cases, rough surfaces are generated by growth processes. It seems to be a general feature that randomness is essential in the development of the self-affine character of the surfaces.

Random deposition (RD) is the simplest (but most unrealistic) deposition model for surface growth. The particles fall vertically at a constant rate independently of one another and stick when they reach the top of a column of deposited particles. As there is no horizontal correlation between the neighboring columns, the surface is extremely rough and the surface structure is compact, i.e., $D_s = d = 3$ for the case of three dimensional simulations [34–37].

In the case of ballistic deposition (BD) a particle is released from a randomly chosen position above the surface located at a distance larger than the maximum height of the interface. The particle follows a straight vertical trajectory until it reaches the surface, where upon it sticks. Contrary to the RD model, the particle can stick also to neighboring columns and typically overhangs appear in the interface structure. One important property of the BD growth process is that, due to the ability to stick at neighboring columns, correlation develops along the surface, which imply that the different sites of the surface are not completely independent, but depend on the heights of the neighboring sites. This is different to the RD model where the interface is uncorrelated and the columns grow independently, as there is no mechanism that can generate correlation along the interface. Numerical calculations of the BD model in $d = 2$ give $D_s \approx 1.5$ [35,37]. In particular, numerical simulation of the BD model with restricted step height yield $D_s \approx 1.5$ in two dimensions ($d = 2$) and for $d = 3$ one obtains $D_s = 2.6$–2.64, dependent on the details of simulations [35,37].

A similar realistic model for surface growth during c.b. processing is random deposition with surface ''diffusion'' [35,38]. There a particle reaches the surface as in the random deposition model, but then is allowed to ''diffuse'' on the surface. The diffusion continues until the particle finds the column of minimum height inside a domain of finite size around the initial contact. A schematic view of the model and an example of the resulting interface for $d = 2$ is shown in Fig. 31.9. The surface diffusion generates a nontrivial

[1] We note that soot and carbon black have the similar mechanism of inception and growth.

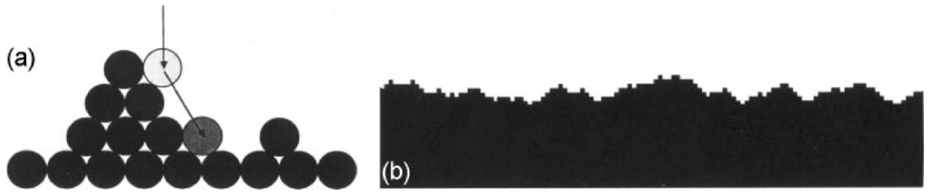

FIGURE 31.9. Random deposition model with surface diffusion. (a) Schematic view of the model in a triangular lattice. (b) Simulation result for a square lattice. Reprinted from [16] with kind permission of Springer Science + Business Media.

correlation between the heights of the columns. Therefore, the roughness of the surface scales with an exponent different from the random deposition model.

The simplest continuum equation describing kinetic roughening is based on a Langevin equation approach and has been introduced by Edwards and Wilkinson (EW) [39]:

$$\frac{\partial h(r,t)}{\partial t} = \nu \cdot \nabla^2 h(r,t) + \eta(r,t). \tag{31.6}$$

The first term on the right side comes from a kind of surface tension and tends to smooth the surface, while the second term is a Gaussian fluctuating white noise satisfying the fluctuation dissipation theorem. Equation (31.6) leads for $d = 2$ to $D_s = 1.5$. Also numerically, this result is well verified for random deposition with surface diffusion [34–38]. For $d = 3$, we find from Eq. (31.6) $D_s = 3$. In this case the correlation decays logarithmically. The discrete growth model, random deposition with surface diffusion, and the continuous EW equation define a universality class, different from random deposition. The construction of the EW equation provides a general procedure that will be useful where more complicated growth models and processes are discussed [34].

The first extension of the EW equation to include nonlinear terms was proposed by Kardar, Parisi, and Zhang (KPZ),

$$\frac{\partial h(r,t)}{\partial t} = \nu \cdot \nabla^2 h(r,t) + \frac{\lambda}{2}(\nabla h)^2 + \eta(r,t), \tag{31.7}$$

where $\lambda/2$ is the coupling of the nonlinear term [40]. Again, the noise η is assumed to be uncorrelated and white and to have a Gaussian distribution. A nonlinear coupling $\lambda \neq 0$ is generated whenever the growth velocity depends on the tilt of the surface [34]. For $d = 2$ the roughness exponent of the interface is $D_s = 1.5$ [34]. Comparing with the numerically-obtained exponents for the BD model ($D_s \approx 1.5$), we find remarkable agreement, suggesting that indeed the KPZ equation and the BD model belong to the same universality class. Kardar, Parisi, and Zhang [40] conjectured that the $d = 2$ result might be superuniversal (independent of d) but this is evidently not correct [36]. At present, no rigorous results are available from Eq. (31.7) for $d > 2$.

A further model of interest for surface growth during c.b. processing is obtained if anisotropy effects are considered in the KPZ equation. The presence of anisotropy is expected to lead to surface tension and nonlinear terms that are different in the two directions. This has been incorporated in the growth equation by considering two different coefficients ν and λ:

$$\frac{\partial h(r,t)}{\partial t} = \nu_x \cdot \partial_x^2 h + \nu_y \cdot \partial_y^2 h + \frac{\lambda_x}{2}(\partial_x h)^2 + \frac{\lambda_y}{2}(\partial_y h)^2 + \eta(r,t). \tag{31.8}$$

Equation (31.8) is called the anisotropic KPZ (AKPZ) equation (see [34] and references therein). If $\nu_x = \nu_y$ and $\lambda_x = \lambda_y$, Eq. (31.8) reduces to the KPZ equation (31.7).

The nontrivial effect of the anisotropy can be observed in the case of stepped surfaces [41,42] or in the three-dimensional discrete Toom model [34,43–45] that is described by the AKPZ equation. The original two-dimensional Toom model has attracted much attention since its nonergodicity in the presence of small perturbations has been proved [45], leading to the possibility that the model is "generic" for a variety of physical systems, including c.b. growth. In this model, spins with values $S = \pm 1$ are simultaneously updated at every time step with the following rule: S becomes equal 1 with probability p, -1 with probability q, and becomes aligned with the majority of itself and a specified set $\{S\}$ of neighboring spins with probability $1-p-q$. When $p = q = 0$, the Toom model is deterministic. For small enough p and q, the model for any dimension has two stable phases: one phase has most spins aligned up $(+1)$ and the other phase has most spins aligned down (-1).

The origin of the surface anisotropy is the anisotropy of the set $\{S\}$ in the updating rule: the x and y directions are not equivalent. Numerical simulations indicate that the interface is described by the AKPZ equation in the strong-coupling or KPZ limit, the scaling exponent in $d = 3$ being $D_s = 2.57 \pm 0.04$ [43]. The mechanisms and results of the $3d$ Toom model can be mapped to surface growth in the case of c.b. formation. Already in the two-dimensional case, where the Toom interface is formed by a rule of simple probabilistic cellular automation [46], this model leads to a $(1+1)$-dimensional solid-on-solid type (SOS) model. Therein, the dynamics of spin flips may be regarded as a "deposition-evaporation" process of particles which occurs in an avalanche fashion [44]. This physics has been generalized in [44], where the spin dynamics in three dimensions is mapped into particle dynamics via the deposition and evaporation process with an avalanche on a checkerboard

lattice. For the biased case the interface is described by the AKPZ equation.

31.4 SURFACE ENERGY DISTRIBUTION FROM STATIC GAS ADSORPTION

The systematic study of c.b. particle surface properties and organization underlines the role of surface morphology in rubber compound properties [47]. In addition to well investigated reinforcing effects caused by the fractal nature of particulate filler aggregates and networks in the rubber matrix [1,8–13,48], the surface activity of fillers plays a key role in reinforcement by controlling the polymer-filler phase bonding and the filler–filler interaction. The surface activity includes: (i) the surface roughness on atomic length scales and (ii) the site energy distribution in relation to the primary particle microstructure and the specific reactivity of adsorption sites with the polymer matrix under consideration. In the previous sections it was demonstrated by equilibrium gas-adsorption measurements on c. b. that the surface roughness, characterized by its surface fractal dimension, is similarly graded for all furnace blacks irrespective of their specific surface area and DBP-number [15]. These results confirm previous findings that all furnace blacks adsorb the same amount (or number) of polymer chains per unit surface area [49]. This would leads to the conclusion that polymer chains of similar chemical nature behave similar concerning their conformational entropy during adsorption on the c.b. surface. Therefore the contribution of the surface roughness cannot explain specific reinforcing effects observed in c.b. filled rubbers.

Early investigations performed by equilibrium gas adsorption have established qualitative differences in the adsorption heat above a surface coverage of 5–10% for original and graphitized c. b. [50]. Nonequilibrium inverse gas-chromatography investigations [51,52] indicate a relationship between the dispersive surface energy contributions and the primary particle size and deliver hints for a heterogeneous surface energy distribution.

In this section we will demonstrate how the site energy distribution, obtained by equilibrium gas-adsorption measurements of ethene on different c.b. grades, can explain the characteristic differences in reinforcement [22,53]. In a typical gas-adsorption experiment the amount N of adsorbed molecules is measured in dependence of the equilibrium pressure p at a constant temperature T. N_m is the maximum number of adsorption sites for a monolayer coverage. The surface coverage Θ is the quotient N/N_m. At low pressures mostly sites with high energies Q are occupied by the gas molecules. With rising pressure more and more molecules adsorb on sites with lower energies Q. At very high pressures p near the vapor pressures p_0 of the pure condensed gas at T the molecules become adsorbed in multilayers. Therefore the isotherms are determined by the energetic surface structure for a given adsorbent. The overall isotherm $\Theta(p,T)$ can be considered as the sum of local isotherms $\theta(p,T,Q)$ of sites with a given energy Q. The local isotherms $\theta(p,T,Q)$ are weighted by the site energy distribution function $f(Q)$. For a continuous distribution function the overall isotherm is given by:

$$\Theta(p,T) = \int_0^\infty \theta(pT,Q) \cdot f(Q)\mathrm{d}Q. \qquad (31.9)$$

The site energy distribution function $f(Q)$ can be calculated by using the experimentally observed overall isotherm $\Theta(p,T)$ and a theoretical local isotherm function $\theta(p,T,Q)$. Here a Langmuir type model equation $\theta(p,T,Q)$ with corrections for multilayer adsorption and lateral interactions between the adsorbed molecules is chosen [54–56]. Then the integral equation can be solved by an analytical iterative method based on numerical integration [57]. More details about this procedure are found in [22,53].

For a precise estimation of the site energy distribution function it is necessary to measure adsorption isotherms down to very low pressures from about 0.001 up to one full monolayer. For this purpose a volumetric gas adsorption apparatus equipped with three capacitance manometers (MKS Instruments Baratron; pressure range: 0.0001–1400 mbar) was used. The temperature T of the c.b. samples was regulated with a cryostat (Huber, $-80\ ^\circ\mathrm{C} - 20\ ^\circ\mathrm{C}$, $\pm$ 0.1 K). Prior to each adsorption measurement, the samples were all subjected to purification extraction treatment (methanol/water (1:1) and toluene each for 48 h) and dried at 40 °C in vacuum. Out-gassing of the samples was carried out at 200 °C in high vacuum for at least 24 h. Ethene (Messer Griesheim, purity $> 99.95\%$) was taken as measurement gas. The investigated c.b. samples with similar aggregate structures (DBP-numbers) and varying mean particle sizes (nitrogen surface area) are shown in Table 31.1. In addition a graphitized N220g was examined as a reference system. The graphitization was performed at 2,500 °C under nitrogen atmosphere.

Figure 31.10 shows the adsorption isotherms of ethene at $T = 223$ K for the examined c.b. samples. As the pressure rises the amount N of adsorbed molecules increases (submonolayer regime) until the isotherms reach a plateau which signifies the monolayer capacity N_m. It can be seen that N115 with the smallest mean particle size has the highest monolayer capacity N_m, whereas N550 with the highest mean particle size has the lowest monolayer capacity N_m. For $p/p_0 \rightarrow 1$ the isotherms increases steeply, because the

TABLE 31.1. *Specific nitrogen surface area (*N_2-SA*) and DBP-number of the investigated c.b. samples.*

	N115	N220	N220g	N550
N_2-SA[m^2/g]	143	118	88	44
DBP [ml/100g]	113	114	–	122

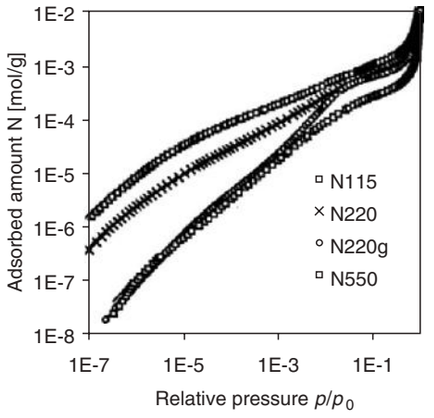

FIGURE 31.10. Adsorption isotherms $N(p,T)$ of ethene on four c.b. samples at $T = 223$ K. Reprinted from [11] with kind permission of Springer Science + Business Media.

gas molecules are adsorbed in multilayers. This regime was extrapolated according to the BET-theory [55]. The symbols in Fig. 31.10 denote the experimental points. The solid lines are the calculated isotherms. Obviously the correlation between the experimental and the fitted isotherms is very good.

The corresponding energy distribution functions $f(Q)$ of ethene calculated from the isotherms are shown in Fig. 31.11. For the original c.b. samples multimodal site energy distribution functions $f(Q)$ are found. The result of an energetic heterogeneous surface structure for N220 has been confirmed by thermodynamic values for isosteric heats of adsorption and infrared spectra of the furnace black N220 in a flow of ethene [22]. The sum curves of the distribution functions $f(Q)$ can be deconvoluted to four gaussian peaks, as shown in Fig. 31.12 for N220. This result demonstrates the existence of discrete energetic surface sites I – IV with

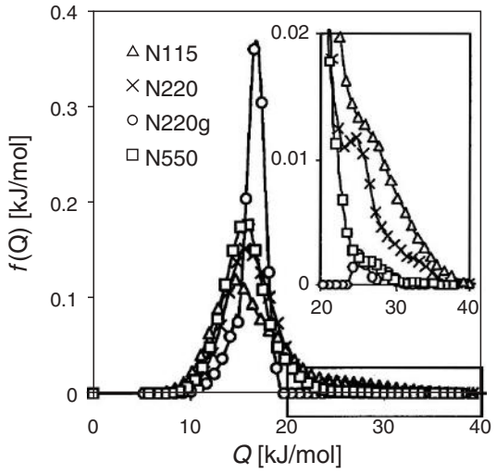

FIGURE 31.11. Site energy distribution function $f(Q)$ for ethene on the c.b. samples shown in Fig. 31.10. Reprinted from [11] with kind permission of Springer Science + Business Media.

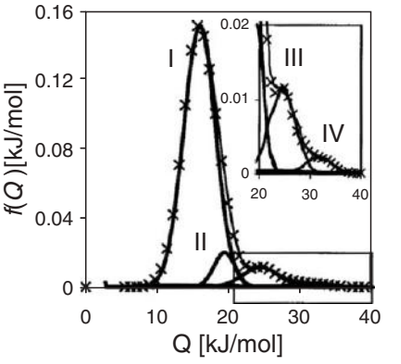

FIGURE 31.12. Deconvolution of the site energy distribution function of N220 to four Gaussian peaks (I–IV). Reprinted from [11] with kind permission of Springer Science + Business Business Media.

energies of $Q(\mathrm{I}) \approx 16$ kJ/mol, $Q(\mathrm{II}) \approx 20$ kJ/mol, $Q(\mathrm{III}) \approx 25$ kJ/mol, and $Q(\mathrm{IV}) \approx 30$ kJ/mol. These sites can be attributed to the microstructure of the spherical primary particles from a comparison of the distribution functions $f(Q)$ of untreated N220 with graphitized N220g (Fig. 31.13).

Contrary to untreated N220, the surface of N220g is energetically more homogeneous (Fig. 31.11). It consists of more than 99% of sites of type I. Sites II are missing and sites III and IV can only be found in traces. It is well known [1] that graphitization increases the degree of crystallization of c. b. with the graphitic planes oriented parallel to the particle surface. So energetic sites I have to be attributed to adsorption sites on graphitic planes and energetic sites II – IV to defect structures which have normally higher interaction energies Q. Possible defect structures are amorphous carbon II with sp^3-hybridization, crystallite edges III or cavities IV between to crystallites. Upon graphitization all amorphous carbon is transformed to carbon incorporated in graphitic planes as revealed by Raman spectroscopy [58] and no energetic sites II are left on the surface (Fig. 31.11). On the other hand side, crystallite edges and cavities should always be present on the surface, because the microcrystallites have to form spherical particles. Compared

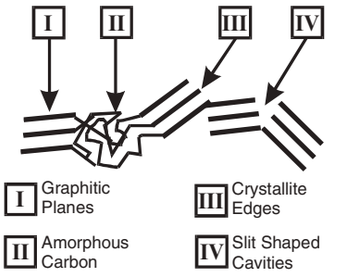

FIGURE 31.13. Proposed attribution for the energetic sites I–IV to the surface microstructure, obtained from the deconvolution of the energy distribution function in Fig. 31.12. Reprinted from [11] with kind permission of Springer Science + Business Media.

to the crystallite edges the cavities IV should have higher energies Q, because an adsorbed gas molecule interacts with the surface from several directions. In a slit shaped cavity the interaction energy Q was calculated to be enhanced by a factor of 1.6 at maximum [59] which can explain interaction energies as high as 40 kJ/mol.

The results of the deconvolution with four gaussian peaks are given in Table 31.2. The percentages at surface of adsorption sites I- IV calculated from the areas of the Gaussian peaks vary significantly: The percentage of high energetic sites III and IV increases with decreasing particle size or increasing specific nitrogen surface area. Accordingly, the percentage of the low energy sites I increases with increasing particle size.

31.5 SUMMARY AND CONCLUSIONS

In conclusion it has been shown that the presented gas adsorption technique gives equal estimates for the surface roughness independent of adsorption temperature or pressure, which is clearly not the case if other evaluation procedures for the cross section that are proposed in the literature are applied. Based on the consideration of film formation of adsorbed molecules in the multilayer regime, it was demonstrated that all examined c. b.s have a unique surface roughness on atomic length scales with a surface fractal dimension $D_s \approx 2.6$ (Fig. 31.7). Thereby, capillary condensation was demonstrated to be the relevant mechanism of film formation of adsorbed probe molecules. This result was confirmed by investigations in the monolayer regime (Fig. 31.4), where the same relatively high value of the surface fractal dimension for the untreated furnace black N220 was found.

We point out that experimental investigations of c. b. surface roughness by two different gas adsorption techniques indicate a universal surface morphology for all furnace blacks. We have presented numerical and theoretical attempts to explain c. b. formation within the today well founded statistical physics of surface growth mechanisms. The universal and scaling properties of the discussed growth models explain the universal topography of c. b. particle surface, independent of c. b. grade. This property can be seen in the universal value of the surface fractal dimension $D_s \approx 2.6$. These universal features can now be understood and traced back to the deeper physical origin of correlation between neighboring sites during the growth process.

The results concerning the energy distribution functions $f(Q)$ of ethene, calculated from the isotherms on a broad pressure range, lead to the conclusion that the examined furnace blacks have an energetic heterogeneous surface structure. With increasing particle size the amount of high energetic sites per gram of filler decreases dramatically showing the very different surface activities to polymers, respectively, the different reinforcement potentials of the fillers. The percentage of high energetic sites is not constant for the grades with different mean particle size. Therefore the value of the specific nitrogen surface area is not sufficient to describe the surface activity of the filler. Upon graphitization the surface becomes nearly energetically homogeneous.

TABLE 31.2. *Estimated fractions [%] of adsorption sites I–IV at the surfaces of the four examined c.b. samples*

	N115	N220	N220g	N550
I ($Q \approx 16$ kJ/mol)	69	84	99	93
II ($Q \approx 20$ kJ/mol)	13	7	–	6
III($Q \approx 25$ kJ/mol)	15	7	< 1	1
IV ($Q \approx 30$ kJ/mol)	3	2	< 1	< 1

ACKNOWLEDGMENTS

The authors are indebted to Professor R. H. Schuster (DIK), Dr. M. Gerspacher and Professor T. A. Vilgis (MPI Mainz) for helpful discussions and to the Deutsche Kautschukgesellschaft (DKG) for financial support.

REFERENCES

1. J. B. Donnet, R. C. Bansal, M. J. Wang (eds), Carbon Black: Science and Technology. Marcel Decker, New York Hongkong (1993)
2. G. Kraus (ed), Reinforcement of Elastomers. Interscience Publisher, New York London Sydney (1965)
3. R. Payne, J. Appl. Polym. Sci. **6**, 57 (1962); ibid. **7**, 873 (1963); ibid. **8**, 2661 (1965); ibid. **9**, 2273, 3245 (1965)
4. G. Kraus, J. Appl. Polym. Sci., Appl. Polym. Symp. **39**, 75 (1984)
5. A. van de Walle, G. Tricot, M. Gerspacher, Kautsch. Gummi Kunstst. **49**, 173 (1996)
6. C. R. Lin, Y. D. Lee, Macromol. Theory Simul. **5**, 1075 (1996); ibid. **6**, 102 (1997)
7. T. A. Witten, M. Rubinstein, R. H. Colby, J. Phys. II (France) **3**, 367 (1993)
8. M. Klüppel, G. Heinrich, Rubber Chem. Technol. **68**, 623 (1995)
9. G. Heinrich, M. Klüppel, T.A. Vilgis, Curr. Opin. Solid State Mater. Sci. **6**, 195 (2002)
10. G. Heinrich, M. Klüppel, Adv. Polym. Sci. **160**, 1 (2002)
11. M. Klüppel, Adv. Polym. Sci. **164**, 1 (2003)
12. A. I. Medalia, Rubber Chem. Technol. **59**, 432 (1986)
13. M. Klüppel, R. H. Schuster, G. Heinrich, Rubber Chem. Technol. **70**, 243 (1997)
14. S. Havriliak, S. Negami, Polymer **8**, 161 (1967)
15. A. Schröder, M. Klüppel, R. H. Schuster, Kautsch. Gummi Kunstst. **52**, 814 (1999), ibid. **53**, 257 (2000)
16. A. Bunde, S. Havlin (eds), Fractals and Disordered Systems, Chap. 7, Springer Verlag, Berlin Heidelberg New York (1991)
17. J. Fröhlich, S. Kreitmeier, D. Göritz, Kautsch. Gummi Kunstst. **51**, 370 (1998)
18. B. Mandelbrot, "The Fractal Geometry of Nature", Freeman, New York, (1977)
19. P. Pfeifer, M. Obert, M. W. Cole, Proc. R. Soc. London, **A 423**, 169, (1989)
20. P. Pfeifer, M. W. Cole, New J. Chem. **14**, 221, (1990)
21. B. C. Lippens, B. G. Linsen, J. H. De Boer; J. Catalysis, **3**, 32, (1964)
22. A. Schröder, PhD-Thesis, University of Hannover (2000)
23. M. Klüppel, A. Schröder, R. H. Schuster, J. Schramm, "The Disordered Morphological Structure of Carbon Black", Paper No. XLI, 157th ACS Rubber Division Meeting, Dallas Texas, 4–6 April (2000)

24. T. P. Rieker, S. Misono, F. Ehrbourger-Dolle, Langmuir **15**, 914 (1999)
25. T. P. Rieker, M. Hindermann-Bischoff, F. Ehrbourger-Dolle, Langmuir **1**6, 5588 (2000)
26. R. C. Bansal, J-B. Donnet, "Mechanism of Carbon Black Formation", in Carbon Black. Sci. Technol. (Eds. J-B. Donnet, R. C. Bansal, M-J. Wang), Marcel Dekker, New York, Basel, Hong Kong (1993)
27. J. Lahaye, F. Ehrburger-Dolle, 'Mechanism of Carbon Black Formation. 'Correlation with the Morphology of Aggregates', in Proceedings 2nd Int. Conf. on Carbon Black, Mulhouse (F), 27–30. September 1993, pp. 11–23
28. H. Bockhorn, "A Short Introduction to the Problem", in H. Bockhorn (Ed.), Soot Formation in Combustion, Mechanisms and Models, Springer-Verlag, Berlin Heidelberg New York, pp. 3–7
29. J. B. Donnet, T.-K. Wang, C. C. Wang, M. Monthioux, M. P. Johnson, D. T. Norman, R. W. Wansborough, P. Bertrand, Kautschuk, Gummi, Kunststoffe **52**, 340 (1999)
30. F. Cataldo, Fullerene Sci. Technol. **8**, 105 (2000)
31. M. P. Johnson, R. W. Locke, J. B. Donnet, T. K. Wang, C. Wang, P. Bertrand, Paper No. 179, "Carbon Black and Fullerenes: New Discoveries in Early Formation Mechanisms and Nucleation", 156th ACS Rubber Division Meeting, Orlando, FL. September 1999
32. J. Warnatz, U. Maas, R. W. Dibble, "Combustion", Springer-Verlag, Berlin Heidelberg New York (1999)
33. G. Heinrich, M. Klüppel, Kautsch. Gummi Kunstst. **54**, 159 (2001)
34. A.-L. Barabási, H. E. Stanley, Fractal Concepts in Surface Growth, Cambridge University Press, Cambridge (1996)
35. J.-F. Gouyet, M. Rosso, B. Sapoval, "Fractal Surfaces and Interfaces", in A. Bunde, S. Havlin (Eds.), "Fractals and Disordered Systems", Springer-Verlag, Berlin Heidelberg New York (1991)
36. J. Kertész, T. Vicsek, "Self-Affine Interfaces", in A. Bunde, S. Havlin (Eds.), "Fractals in Science", Springer-Verlag, Berlin Heidelberg New York (1994)
37. P. Meakin, "Fractal Structures", Progr. Solid St. Chem. **20**, 135–233 (1990)
38. F. Family, J. Phys. **A 19**, L441 (1986)
39. S. F. Edwards, D. R. Wilkinson, Proc. R. Soc. London A 381, 17 (1982)
40. M. Kardar, G. Parisi, Y. C. Zhang, Phys. Rev. Lett. **56**, 889 (1986)
41. K. Moser, D. E. Wolf, "Kinetic roughening of vicinal surfaces", in "Surface Disordering: Growth, Roughening and Phase Transitions", in R. Jullien, J. Kertész, P. Meakin and D. E. Wolf (Eds.), Nova Science, New York (1992), pp. 21–30
42. D. E. Wolf, Phys. Rev. Lett. **67**, 1783 (1991)
43. A.-L. Barabási, M. Araujo, H. E. Stanley, Phys. Rev. Lett. **68**, 3729 (1992)
44. H. Jeong, B. Kahng, D. Kim, Phys. Rev. Lett. **71**, 747 (1993)
45. A. L. Toom, in 'Multicomponent Random Systems', (Eds.: R. L. Dobrushin, Ya. G. Sinai), Dekker, New York (1980)
46. B. Derrida, J. L. Lebowitz, E. R. Speer, H. Spohn, Phys. Rev. Lett. **67**, 165 (1991)
47. J. B. Donnet, Rubber Chem. Technol. **71**, 323 (1998)
48. M. Gerspacher, C. P. O'Farrell, L. Nikiel, H. H. Yang; F. LeMehauté, Rubber Chem. Technol. **69**, 789 (1996)
49. D. Bussmann, Ph. D. Thesis, Universität Hannvoer (1992)
50. R. A. Beebe, J. Biscoe, W.R. Smith, C.B. Wendell, J. Am. Chem. Soc. **69**, 2294 (1947)
51. J.-B. Donnet, Carbon **32**, 1305 (1994)
52. M.-J. Wang, S. Wolff, Rubber Chem. Technol. **65**, 715 (1992)
53. A. Schröder, M. Klüppel, R. H. Schuster, J. Heidberg, Kautsch. Gummi Kunstst. **54**, 260 (2001), ibid. Carbon 40, 207 (2002)
54. I. Langmuir, J. Am. Chem. Soc. **40**, 1361 (1918)
55. S. Brunauer, P. H. Emmett, E. J. Teller, J. Am. Chem. Soc. **60**, 309 (1938)
56. R. H. Fowler, E. A. Guggenheim, "Statistical Thermodynamics", Cambridge University Press, Cambridge (1952)
57. A. W. Adamson, I. Ling, Adv. Chem. **33**, 51 (1961)
58. T. W. Zerda, W. Xu, H. Yang, M. Gerspacher, Rubber Chem. Technol. **71**, 26 (1998)
59. D. H. Everett, J. C. Powl, J. Chem. Soc. Faraday Trans. I **72**, 619 (1976)

CHAPTER 32

Properties of Polymers Reinforced With Silica

Chandima Kumudinie Jayasuriya* and Jagath K. Premachandra†

*Department of Chemistry, University of Kelaniya, Dalugama, Kelaniya, Sri Lanka
†Department of Chemical and Process Engineering, University of Moratuwa, Katubedda, Moratuwa, Sri Lanka

32.1 INTRODUCTION

The elastomers which cannot undergo strain-induced crystallization are generally reinforced with permanent reinforcing fillers [1–5]. The incorporation of fillers into polymers has the advantage of increased tensile strength, tear strength, abrasion resistance, resilience, and extensibility. However, the incorporation of fillers into a polymer has several disadvantages including increases in hysterisis and thus heat build-up resulting permanent deformation [1–5]. Two of the most important examples for the use of reinforcing fillers are the incorporation of carbon black fillers into natural rubber and to some other elastomers [6–8] and the incorporation of silica fillers into siloxane polymers [5,9]. Other polymers that have been reinforced using fillers include acrylates [10–13], polyamides [13], polyimides [15], polybenzoxazoles [16,17], and polybenzothiazoles [16,17]. Fillers such as titania, zirconia, mixed fillers of silica–titania and silica–zirconia, clays, metallic particles, and even glassy polymers have been used to achieve reinforcement.

The focus of this review is the properties of polymers reinforced with silica, however, the synthetic approaches of incorporating silica into polymers will also be briefly discussed.

32.2 IN SITU GENERATION OF SILICA

Experimental evidences indicate that the extent of the reinforcement depends strongly on the particle size. The maximum reinforcement is obtained for particles with diameters ranging from 10 to 100 nm. Although polymers filled with such nanoscaled silica fillers, i.e., polymer–silica nanocomposites can be prepared by a variety of approaches, the majority of such composites are prepared through the sol–gel technique. Sol–gel reaction of a silicon alkoxide is a method for preparing inorganic silicon oxides under mild conditions [18]. It involves simultaneous hydrolysis and condensation of silicon alkoxide to form a three-dimensional silica network.

The sol–gel reaction has been used to in situ precipitate very small, well-dispersed silica particles into a polymeric material [19,20]. Silica particles thus produced give good reinforcement to a variety of elastomers. This technique avoids the difficult, time-consuming and energy extensive process of blending agglomerated filler into high molecular-weight polymers, especially when this is applied to elastomers. Insitu precipitation of silica using sol–gel technique can be done after, during or before crosslinking [20]. In situ filled elastomer is then extracted with a good solvent to achieve reinforcement. Various polymeric phases such as elastomers, glassy polymers, semicrystalline polymers and high-temperature polymers have been reinforced with silica in situ generated by the sol–gel technique [21,22].

Among elastomers, poly(dimethyl siloxane) (PDMS) has been the most extensively studied polymer with in situ generated filler. PDMS has frequently been chosen since it is compatible with silica or any other organometallic material used to generate ceramic phases. In addition, being a low-strength material, PDMS requires a considerable reinforcement from fillers before it is useful in many industrial applications [5,6]. A large number of other elastomeric phases including poly(phenyl methyl siloxane) [20,21], polybutadiene [21,23], and polyisobutylene [21,24] have been reinforced with silica using the sol–gel approach. Examples of glassy polymers [21] reinforced with in situ

generated silica include polyacrylates [12], poly(vinyl acetate) [25–27], and polyanilines [28]. Semicrystalline phases treated by the sol–gel technique include poly(tetra methylene oxide) [29,30], poly(ethylene oxide) [31,32], and poly(vinyl alcohol) [21,22]. Although it is difficult to treat high-temperature polymers in the usual sol–gel technique, few studies on aromatic polyamides [33,34], polyimides [35–40], polybenzobisoxazoles [16,17], and polybenzobisthiazoles [16,17] have been reported. High-temperature, high-performance polymers are generally unreactive which cause poor bonding between the polymeric and ceramic phases. This problem can be minimized by functionalizing the polymer or by adding a bonding agent [16,17,21,41].

32.3 CHARACTERIZATION TECHNIQUES

Polymer–silica nanocomposites thus prepared are characterized by electron microscopy, scattering techniques, nuclear magnetic resonance spectroscopy, etc. to determine the structural features. In addition, properties such as mechanical, thermal, optical, and other important physical properties are generally determined.

32.3.1 Structural Features

Electron Microscopy

Both transmission electron microscopy (TEM) and scanning electron microscopy (SEM) have been used to determine structural features of various polymer–silica systems. Electron microscopic techniques generally provides information on the nature of the filler, average particle size, or the distribution of particle sizes, smoothness of the interfaces, and the degree of agglomeration of particles.

Transmission electron micrographs obtained for silica-filled PDMS elastomers in base (ethyl amine) catalyzed hydrolysis of tetraethoxysilane (TEOS) and acid (acetic) catalyzed hydrolysis of TEOS are given in Figs. 32.1 and 32.2, respectively [2,3]. Figure 32.1 shows that the particles in this silica-filled PDMS network have an average diameter of approximately 80 Å which is a very much desirable size with regard to reinforcement. Figure 32.1 also indicates that the filler particles have a relatively narrow size distribution, very little agglomeration, and well-defined surfaces. On the other hand, acidic catalysts yield poorly defined, agglomerated particles (Fig. 32.2) [2,3].

Electron microscopic results on networks filled in situ by the sol–gel approach have shown that the filler particles typically have a narrow distribution of sizes, with most diameters in the range 200–250 Å. TEM studies on the distribution of silica in situ generated within PDMS have shown that well-distributed particles can be obtained by using basic catalysts, thin samples, and long hydrolysis times, while the silica was found to precipitate mainly in the sample periphery in the case of acidic conditions, bulky

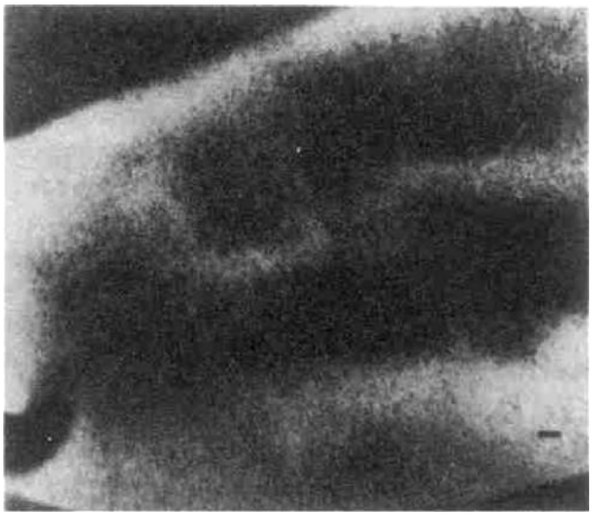

FIGURE 32.1. Transmission electron micrograph for PDMS filled with silica using basic catalysts. From [2] 1988 © John Wiley and Sons.

samples, and short hydrolysis times [42]. TEM was also used for characterizing PDMS networks filled with silica–titania and silica–zirconia mixed oxides [48–50]. The distributions of particle sizes in such systems were relatively narrow with average particle diameter approximately 200–250 Å which increased to 300–350 Å when the molecular weight of the PDMS chains increase from 18,000 g/mol to 26,000 g/mol presumably due to the confining effect of the network pores. The silica–zirconia mixed oxide fillers were found to have particle sizes and distributions very similar to those of the silica–titania ones [48–50].

TEM studies performed on silica filled poly(tetramethylene oxide) by the sol–gel process showed an increase in the

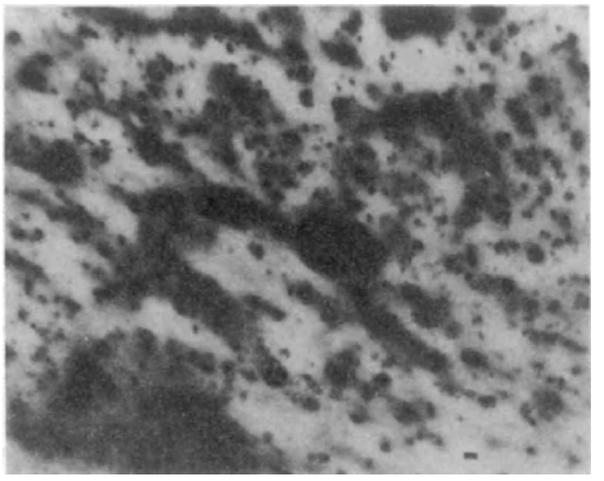

FIGURE 32.2. Transmission electron micrograph for PDMS filled with silica using acid catalysts. From [2] 1988 © John Wiley and Sons.

particle size as the TEOS concentration was increased [43]. This is due to the fact that the phase separation between the metal oxide and oligomeric phases is greater when the metal alkoxide content is increased. Similar results have been obtained for poly(phenylene terephthalamide)–silica ceramers with interface bonding achieved by the use of aminopropyltriethoxysilane [34].

Electron microscopy results for composites prepared using TEOS and tetramethylorthosilicate (TMOS) in trialkoxysilane-functionalized and unfunctionalized polyacrylates indicated phase separation behavior in the composites of methacrylate polymers when the methyl groups are substituted with butyl groups, due to the absence of hydrogen bonding between the silicate and the polymer [44]. Electron microscopy has also been used to demonstrate the particle distribution in a study of the effects of dispersion and aggregation of silica in poly(methyl methcrylate) [45]. In addition, SEM results on nanocomposites prepared using mesoporous silica particles in a methacrylate polymer indicated spherical silica particles ranging from 1 to 10 μm in diameter [46]. The composites showed a certain degree of chain orientation. SEM results also suggested that the composites were composed of polymer that threaded through the mesoporous silica particles and the polymer formed among these filler particles. Compared with conventional particle/polymer composites prepared using dense particles as fillers, it was suggested that these porous fillers may serve as pseudo crosslinking points with the nanocomposites [46].

SEM results on polyimide–silica composites also showed dispersed silica particles of diameter of 3–7 μm [15]. The particle size increased with the silica content as already mentioned for other composite systems [43]. When a bonding agent, (aminophenyl)trimethoxy silane (APTMOS) was incorporated to provide bonding sites between the polymer and the silica like phase, the particles were much smaller and more uniform. This could be explained by the fact that aminophenyl group on the substituted silicon trialkoxide reacted with the polymer chains, possibly improving the compatibility of silica with the polymer. It also has the tendency to prevent the formation of high molecular weight silicate, thus reducing the size of clusters [38,47]. In a similar study, polyimide–silica hybrid materials prepared by the incorporation of small amounts of γ-glycidyloxypropyltrimethoxysilane exhibited finely-dispersed co-continuous phase morphology [39]. Similar observations were made for other composites such as polybenzoxazole–silica and polybenzobisthiazole–silica prepared with interfacial bonding achieved by the use of bonding agents [16,17]. In another study, partial replacement of TEOS with a nonpolar network modifier, dimethylethoxysilane, in polyimide–silica composites caused precipitation of fine silica-rich particles [39]. On the other hand, SEM results obtained for composites prepared using ''site isolation'' method by trapping SiO_2 in polyimide matrices indicated the presence of oxide nanoclusters of size 1–1.5 nm up to 32% silica content and when it was increased to 42% the particles were 1 μm in size [36].

A comparison of properties of composites of poly(vinyl acetate) (PVAc) and silica prepared by the sol–gel process and those prepared by the melt milling or solution casting with fumed silica indicated that both types of films were transparent, however, TEM pictures for two types showed a microscopic heterogeneity [26]. Qualitative differences were apparent with respect to the primary particle size, the size of phase heterogeneity and the sharpness of the polymer–filler interface. TEM pictures obtained for both melt-milling and solution casting indicated that the aggregates are evenly dispersed. Figure 32.3 shows a TEM picture for PVAC–silica composites with 20 wt% silica prepared using solution casting from THF.[26]. The absence of larger micron-sized clusters are also supported by the fact that the films are optically transparent. The micrograph for PVAc film filled in situ with silica by the sol–gel process also showed a two-phase morphology, however, with a much finer texture indicating a more intimate mixture of the two phases (Fig. 32.4)

Scattering Techniques

Analyses of structural features using small angle, light, X-ray, and neutron scattering (SALS, SAXS, SANS) have been carried out for a number of polymer–silica systems [26,43,44,51,52]. In general, scattering data provides estimates of average particle size and the particle size distribution. In addition, the terminal slopes give an indication of the nature of the interfaces, with −3 corresponding to rough interfaces and −4 to smooth. Some typical SAXS results are shown in Fig. 32.5 [2].

Beaucage and coworkers analyzed the structural features of PDMS–silica composites and interrelated those features over a wide range of length scales using the unified approach

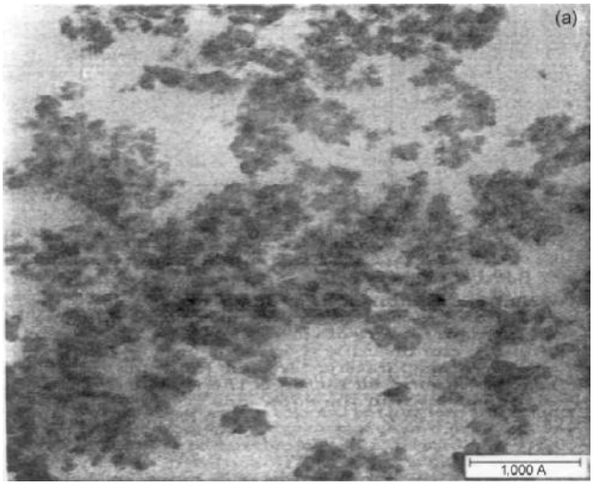

FIGURE 32.3. Transmission electron micrograph for PVAC–silica composites with 20 wt% silica prepared using solution casting from THF. From [26] 1993 © American Chemical Society.

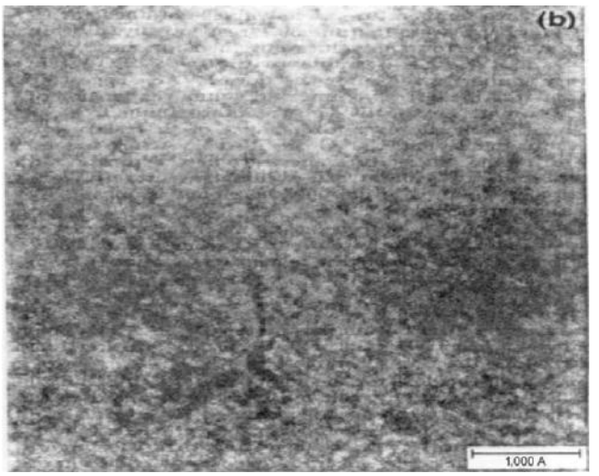

FIGURE 32.4. Transmission electron micrograph for PVAC–silica composites with 16 wt% silica prepared using the sol–gel process. From [26] 1993 © American Chemical Society.

[51]. Analysis of rubber filled with conventional filler and an in situ filled siloxane sample displayed three levels of structure in the size-range observed [51]. In another study, growth mechanism and structures of siloxane composites containing silica, and silica–titania were studied by Breiner *et al*. using SAXS. Both systems were found to yield dense particles.

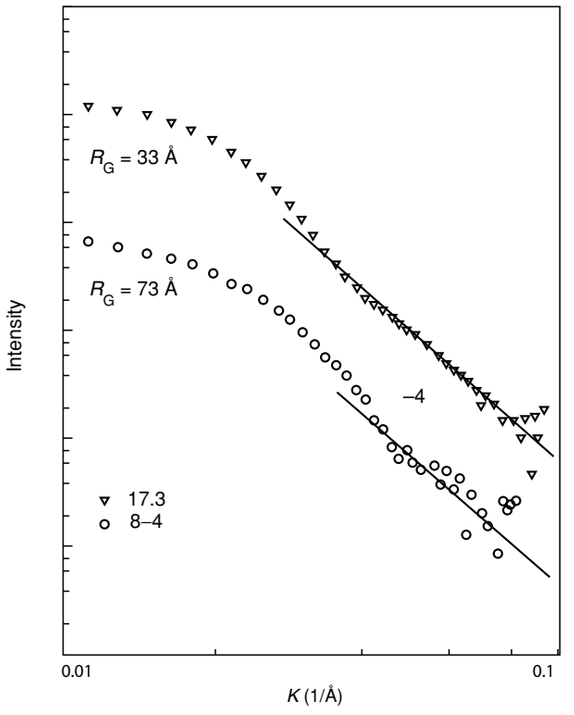

FIGURE 32.5. Intensity of small angle x-ray scattering as a function of the scattering vector for PDMS networks containing 17.3 wt% (▽) and 8.4 wt% (O) silica. From [2] © John Wiley and Sons.

The scattering results suggested that the corresponding growth processes in the mixed oxides proceeds by the formation of relatively uniform titania particles, followed by the formation of significantly larger silica particles [52].

A morphological model for PTMO–metal oxide ceramers was proposed by Rodriguez *et al*. and validity of the model was tested under a variety of variables such as temperature, metal alkoxide content, oligomer spacer length, and the solvent. All three types of ceramers investigated, PTMO–silica, PTMO–titania, and PTMO–zirconia displayed very similar SAXS profiles each showing a single interference peak suggesting the existence of a microphase-separated morphology in accordance with the proposed model [43]. Among the three metal alkoxides employed, the scattering intensity was the lowest for TEOS and the highest for zircornium propoxide. This could be explained by the fact that as the atomic number of the inorganic component increases, so does the mean square electron density difference between the inorganic and the oligomeric components which in turn causes an increase in the scattering intensity. The peaks in the scattering profiles were determined to be due to interparticle interference. Thus, by increasing the length of the organic matrix spacer between the particles, the interdomain spacing as measured from SAXS profiles also increased as expected [43].

In another study, composites made using in situ polymerization of TEOS and TMOS in the presence of tri alkoxy functionalized and unfunctionalized polyacrylates were characterized using SAXS [44]. Slight differences in the local morphology were observed by SAXS, however, macroscopic phase separation was controlled to a large degree by the ability of the backbone to interact with the growing silica network [44].

SAXS studies have also been performed for PVAc–silica composites prepared by solution casting or melt-milling techniques or by in situ [26]. SAXS profiles of PVAc–silica composites containing 20 wt% silica prepared by solution casting and melt-milling were found to be identical suggesting that the local structure of the silica aggregates is the same whether the composites were prepared by solution casting or melt-milling. The final power law slope of −4 at the highest scattering vectors indicates that the surface of primary silica particles is smooth and a sharp interface exists between the organic and inorganic phases. SAXS profiles for several compositions of in situ prepared PVAc–silica composites all approached a limiting slope of −2.45, indicating that the structures are mass fractals [26].

Nuclear Magnetic Resonance Spectroscopy

Nuclear Magnetic Resonance Spectroscopy (NMR) is a useful technique in characterizing the structures being formed and in determining the extent to which chemical reactions are occurring [21,53–57]. For example, ^{29}Si NMR spectrum of polyimide–silica composites consisted of nonhydroxy, monohydroxy, and dihydroxy siloxane

structures, suggesting that the formation of developed silica–oxygen network structure was incomplete.

In addition, NMR imaging utilizing ^{1}H and ^{29}Si magic-angle spinning, with two-dimensional Fourier transform spin echo technique has been an extremely useful nondestructive technique in determining inhomogeneities in in situ filled networks [3,21]. For example, PDMS networks reinforced by in situ precipitated silica were characterized by measuring bulk-spin lattice (T_1) and spin–spin (T_2) relaxation times [58,59]. PDMS–silica composites were intentionally made inhomogeneous by using bulky samples and carrying out the precipitation reaction for a short period of time. Thus, T_1 and T_2 maps showed significant variations of NMR signal intensity throughout the sample due to nonuniform hydrolysis of TEOS in the specimens [58,59].

Infrared Spectroscopy

Infrared spectroscopy (IR) is also a very useful technique for characterizing structure. IR spectroscopy can be used for identification purposes as well as for monitoring the progress of a chemical reaction. Comparisons of the positions of absorptions in the IR spectrum of a sample with the characteristic absorption regions, leads to identification of the bonds and functional groups present in the sample. For example, the chemical structures of polyimide–silica hybrid films were confirmed by IR spectroscopy by the appearance of two absorptions at 1,100 and 830 cm^{-1} indicating the formation of the Si–O bonds.

32.3.2 Densities

Density measurements of polymer–silica composites provide very useful information on the filler particles. In general, density of polymer–silica composites increases with increasing amount of silica because of the high density of silica compared to the polymer. Densities of the filled networks, unfilled network, and silica are used to estimate the weight% silica in the composite which could then be compared with the values obtained directly from weight increases. Such comparisons in PDMS–silica systems have shown that the densities obtained by density measurements were smaller than those determined by weight increases, suggesting possible voids or incomplete hydrolysis of TEOS. In another approach by Morikawa *et al*., the density of silica estimated by extrapolation of the density versus percent silica curve was smaller than that of the usual silica glass suggesting incompletion of polycondensation to form silica structure. This result was consistent with those obtained for NMR studies.

32.3.3 Water Absorption

The knowledge of the relative rate of water absorption is important, since water can influence many physical properties such as electrical insulating ability, dielectric loss, dimensional stability, and appearance. The relative rate of water absorption measured for several polyamide–silica [34,41], polybenzoxazole–silica [16,17] and polybenzobisthiazole–silica [16,17] systems showed a considerable decrease in water absorption in the films containing 5–10 wt% silica with a slight additional decrease for higher silica contents. The decreased hydrophilicity could be explained by the fact that silica hindered the access of water to the polar, hydrogen-bonding regions of the composites.

32.3.4 Transparency

Transparency in some polymer–silica composites make them qualify for various optical applications. One example is PDMS–silica composites which show excellent transparency [60]. On the other hand, polyimide–silica hybrid films containing very low amounts of silica were transparent even after the films were heated to 270 °C where as the films containing more than 10 wt% silica were opaque and were phase separated upon drying [15]. This is due to the fact that increase in amount of silica increases the size of particles, increasing the magnitude of scattering, resulting opaque films. Another example involves polyamide–silica composites which were transparent up to 20 wt% silica content [33,34]. The films containing 25 wt% silica was only semi-transparent and partial phase separation was found to occur during the drying process with the films containing higher silica contents. When a bonding agent was used, the films with up to 25 wt% silica content were completely transparent indicating that the bonding agent has chemically bonded the two phases suppressing the phase separation [33,34]. In addition, transparent polymer–silica composites were prepared using other high temperature polymers such as polybenzoxazoles and polybenzothiazoles with interfacial bonding achieved through the use of bonding agents [16,17].

32.3.5 Thermal Properties

Thermogravimetric Analysis

Thermogravimetric analysis (TGA) which records the weight of the sample against the temperature is a useful technique in determining how the sample is deteriorated at various temperatures. Thus, it can be used not only to study thermal decomposition and stability of materials but also to give important structural information.

Thermogravimetric analyses of various polymer–silica composites including PDMS–silica [61], polyamide–silica [33,34], polyimide–silica [15,38,47], polybenzoxazole–silica [16,17], polybenzobisthiazole–silica [16,17] and PDMS–silica–titania [62] have been reported, in all cases indicating that the incorporation of silica raises the temperature of thermo oxidative degradation of the polymer. A possible mechanism for the improvements in degradation temperature could be due to silica inactivating the terminal OH groups

which participate in the degradation process [3]. In addition, weight residues at elevated temperatures, for example at 800 °C, were found to increase with the increase in amount of silica in the composites which could also be attributed to the same reasoning indicated above [15,17,33,34,38,47].

A comparative study of thermal stabilities involving PDMS–silica composites showed that commercial fume silica caused more severe degradation problem than did in situ precipitated silica [61]. This improvement in the case of in situ precipitated silica could be due to the increased capability of silica introduced in situ to tie up hydroxyl chain ends [3,61].

Differential Scanning Calorimetry

The basis of differential scanning calorimetry (DSC) is the change in specific heat of the polymer as it passes through the glass transition, upon the change of temperature. DSC is one of the most convenient methods of determining glass transition temperature. A study of low temperature properties of unfilled and filled PDMS networks in the unstretched state [63] using DSC showed that the filler reduces both the extent of crystallization and the rate of crystallization, in contrast to the results obtained for PDMS networks in the stretched state [3,64]. Influence of silica content on T_g was determined for various polymer–silica composites including PDMS–silica [63], PMMA–silica [12,45,65], and PVAc–silica [12] using DSC. Results indicated that the T_g of a composite can increase, decrease or stay unchanged depending on the specific polymer-filler system.

Thermal Expansivity

Polymers, in general, show high expansivities than most metals and ceramics. Therefore, changes in composition can produce significant changes in thermal expansivities [66]. Thus, preparing composites by incorporating inorganic and metallic fillers into polymers can result materials with reduced thermal expansivities. For example, thermal expansivities of polyimide–silica composites were found to decrease with increase in silica content [15]. Such composites prepared with a compatibilizer resulted a larger reduction in thermal expansivities possibly due to the co-continuous phase morphology achieved by compatibilization [39]. However, in applications in which large temperature changes must be tolerated, a compromise between modulus and expansivity to minimize thermal stress is required.

32.3.6 Mechanical Properties

Uniaxial Extension

There have been numerous experiments carried out on various polymer networks in situ filled with silica in uniaxial extension [3,14,15,17,19–21,67,68]. In fact, the uniaxial extension is the mostly studied deformation to characterize the effects of particles produced in situ on the mechanical properties of filled elastomers. Only few studies are available on other deformations such as biaxial extension, shear, and torsion because of the difficulties of imposing such deformations. In general, the results for uniaxial extension are represented as stress–strain isotherms. Such isotherms represented as the dependence of nominal stress on elongation for silica-filled PDMS by simultaneous curing and filling is given in Fig. 32.6 [68]. In this representation, the area under each curve corresponds to the energy required for network rupture.

Same set of isotherms in Fig. 32.6, when represented as reduced stress as a function of reciprocal elongation is given in Fig. 32.7. Upturns in [f^*] observed at high elongations clearly demonstrate the reinforcing effect.

Studies of uniaxial extension on noncrystallizable elastomer, poly(phenyl methyl siloxane) showed results which are consistent and comparable with those obtained for PDMS, suggesting that the crystallization is not important for this type of reinforcement [20]. Other examples for reinforcement effects achieved with the addition of silica fillers include polyisobutylene [24], poly(ethyl acrylate) [3], poly (tetra methylene oxide) [29,30], and some high-temperature polymers such as aromatic polyamides [14,33,34], polyimides [15,38,39], polybenzoxazoles [16,17], and polybenzobisthiazoles [16,17]. Results indicated that the modulus increases with increase in silica content while the tensile

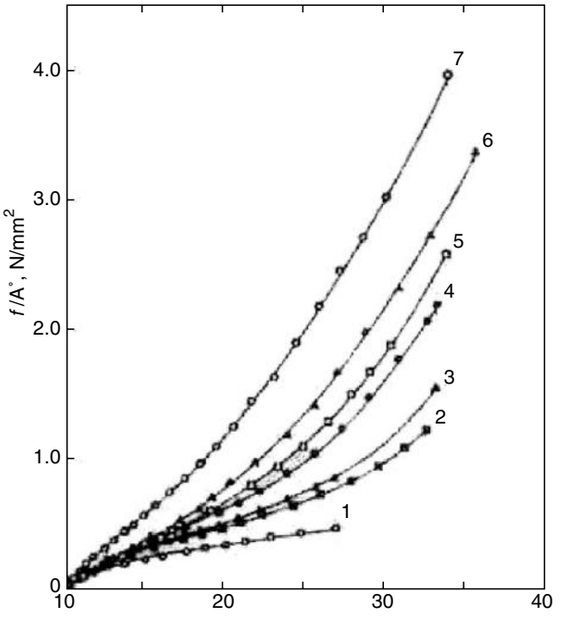

FIGURE 32.6. Nominal stress as a function of elongation for PDMS networks filled with silica by simultaneous curing and filling: 1—unfilled, 2—1.80 wt%, 3—1.96 wt%, 4—5.12 wt%, 5—5.59 wt%, 6—5.74 wt%, and 7—8.61 wt% silica determined by density measurements. From [68] 1984 © American Chemical Society.

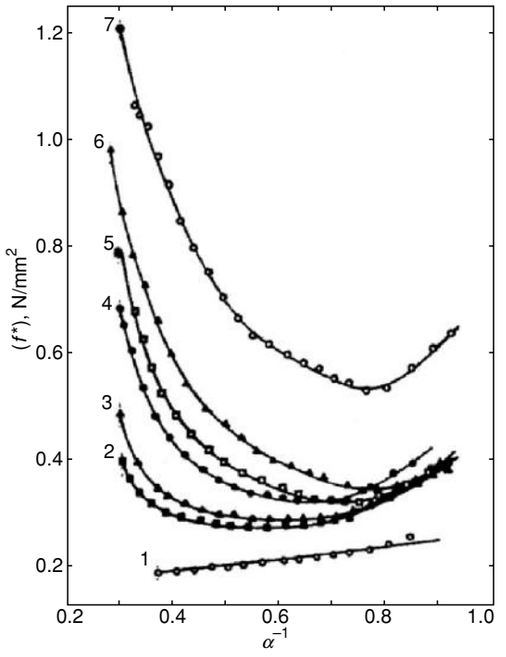

FIGURE 32.7. Same set of isotherms in Fig. 32.6, when represented as reduced stress as a function of reciprocal elongation. From [68] 1984 © American Chemical Society.

strength and the elongation at break decreases. This could be explained by the incorporation of large silica particles. However, by incorporating small amounts of bonding agents to provide better bonding between the two phases, both the modulus and the tensile strength were increased [14,17,38,39]. The improvements thus obtained could be explained by both reductions in particle size which increases the interfacial area and by the introduction of bonding between the polymer chain and silica. The reinforcement achieve will depend on the structure of the polymer involved. For example, a study of linear and nonlinear polyamide–silica chemically bonded systems showed that the latter had low strength relative to the former due to the irregularity of the polyamide structure [14].

In one study with polyamide–silica composites compatibilised with γ-glycidyloxypropyltrimethoxysilane, the increase in tensile strength up to about 25 wt% silica was explained by more stress transfer mechanism between the two components due to the co-continuous phase morphology developed with the addition of the coupling agent [39]. The same study indicated that the elongation at break decreased equally in both cases with or without coupling agent with increasing silica content, confirming that failure is controlled mainly by events within the polymer phase [39].

Biaxial Extension

Only a few studies on elastomers filled with silica in biaxial extension are available simply because of the difficulty in imposing such deformation [69–71]. The state of deformation for biaxial extension can be described using equations similar to those used for uniaxial extension [2,3]. A state of biaxial extension is achieved by stretching a thin sheet of elastomer in two directions in its own plane. The most convenient way of producing equibiaxial extension is inflation of a circular sheet, clamped around its circumference, into the form of a part of a spherical balloon [69–71]. Since biaxial extension is equivalent to uniaxial compression, both biaxial and uniaxial deformation data can be combined in the same plot. In this way, a full spectrum of stress–strain data for both elongation and compression can be viewed, and the behavior of networks in the deformation regions can be compared directly [69]. Results obtained for a PDMS network filled with in situ generated silica for both elongation ($\alpha^{-1} < 1$) and compression ($\alpha^{-1} > 1$) are therefore depicted in Fig. 32.8 where modulus is plotted against α^{-1}. It is obvious that very strong reinforcing effects from the precipitated silica occur for biaxial extension as well as for elongation. This is evident from both the large upward shifts of isotherms as a whole and from pronounced upturns at both high elongations($\alpha^{-1} < 1$) and at high compressions ($\alpha^{-1} > 1$). As can be seen from the figure 32.8, such reinforcing effects do not exist in the unfilled PDMS sample.

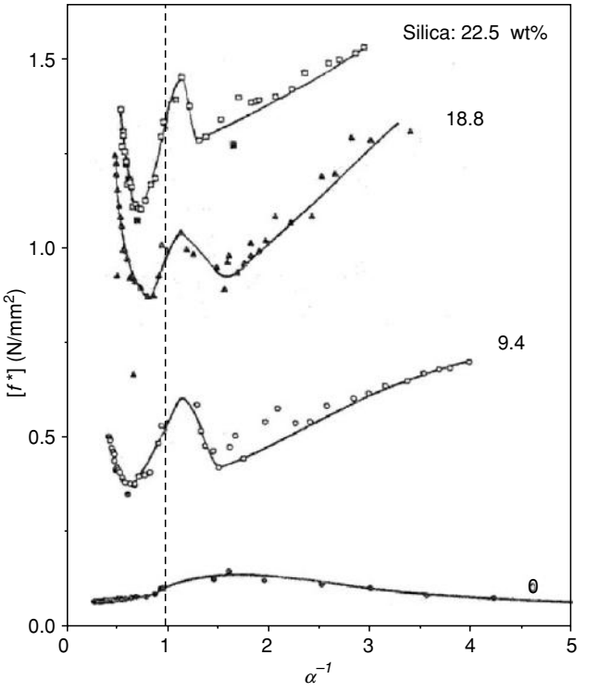

FIGURE 32.8. Stress–strain isotherms for PDMS networks filled with in situ generated silica for both elongation ($\alpha^{-1} < 1$) and compression ($\alpha^{-1} > 1$). The filled points represent the data used to test for reversibility. From [69] 1991 © American Chemical Society.

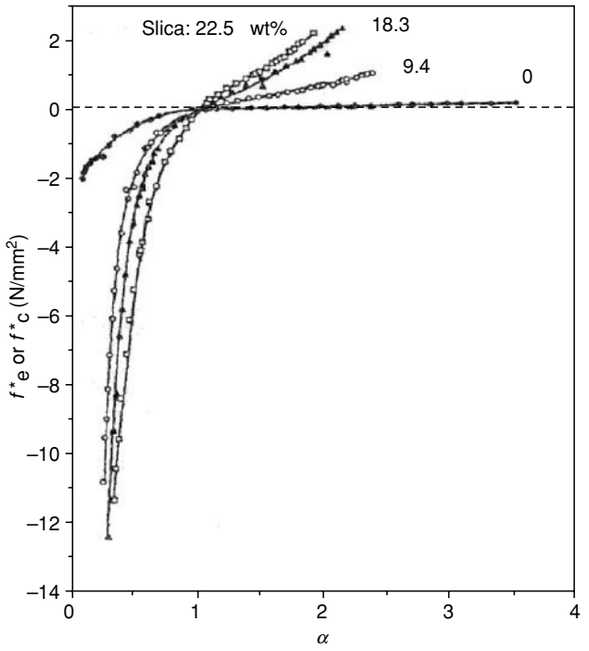

FIGURE 32.9. The same set of isotherms shown in Fig. 32.8, now represented as the dependence of the nominal stress on deformation for both elongation (e) and compression (c). In this representation, tensile stress (f^*_e) is positive and the compressive stress (f^*_c) is negative. From [69] 1991 © American Chemical Society.

The same results are represented in Fig. 32.9 where nominal stress is plotted as a function of deformation. The tensile stress is positive while the compressive stress is negative and a single continuous curve represents both elongation and compression without any discontinuity in passing through the point (1,0) characterizing the undeformed state. Compared to the unfilled sample, the silica-filled samples showed large reinforcing effects. Specifically their values of the modulus, ultimate strength, and rupture energy were increased significantly. The reinforcing effects thus produced, as gauged by the magnitude of the upturns, is approximately the same in uniaxial and in biaxial extension. However, the range of deformation over which it occurs seems to be larger in the case of biaxial extension. Results also indicate that the increase in filler content decreases the deformation at rupture.

Shear

Only a very few studies have been carried out to characterize the reinforcement of in situ precipitated silica in elastomers in shear [3,69,72,73]. There are two types of shear: simple shear and pure shear. Simple shear is a type of strain obtained by sliding a plane which is parallel to a given plane, through a distance which is proportional to the distance from the given plane [3,69]. The lateral faces of a cube are transformed by simple shear into parallelograms, and the amount of shear is measured by the tangent of the angle ϕ through which a vertical edge is tilted [3,69]. Pure shear involves extension in three perpendicular directions without rotation of the principal axis of the strain. The stress–strain isotherms obtained for both unfilled and filled PDMS networks, represented in terms of the shear modulus G and principal extension ratio α, is shown in Fig. 32.10. The results in simple shear, in terms of shear strain were essentially identical [72]. For filled networks, there is an initial decrease in the modulus with increase in deformation. Also, the larger the amount of filler present, the more pronounced the decrease. This may be due to strain-induced rear arrangements of the chains in the vicinity of the filler particles. Also of possible relevance is the fact that an increase in amount of filler decreases the number of load-bearing chains passing through the unit cross-sectional area and changes the distribution of their end-to-end distances [69]. In an alternative representation, the pure shear nominal stress f^* is plotted against the extension ratio α, as shown in Fig. 32.11. Results showed that the filled samples have much higher shear moduli than the corresponding unfilled sample. Also, at high deformation, pronounced upturns in the reduced stress or modulus appear in the case of filled samples which indicate good reinforcement. The extension

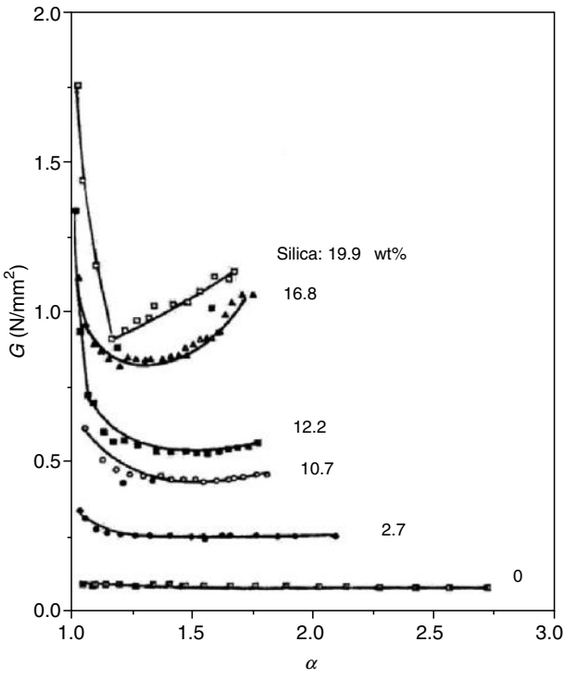

FIGURE 32.10. Stress–strain isotherms represented in terms of the shear modulus G and principal extension ratio α, for both unfilled and filled PDMS networks in pure shear. The filled points represent the data used to test for reversibility. From [69] 1991 © American Chemical Society.

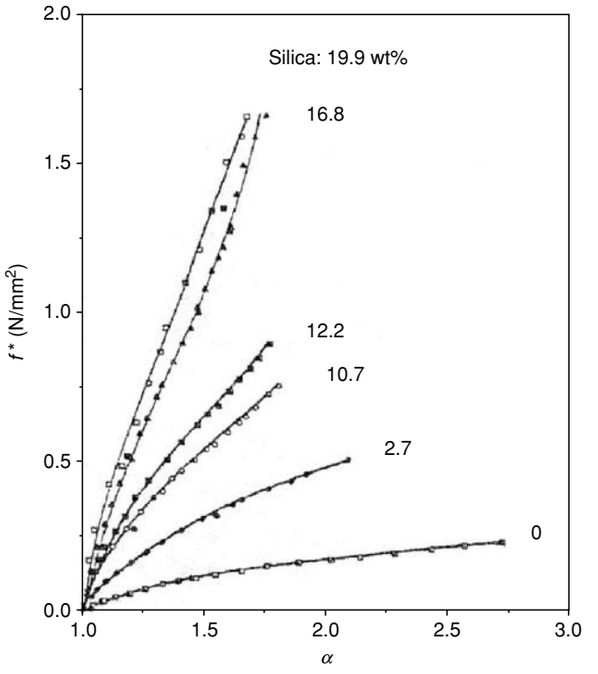

FIGURE 32.11. The stress–strain data shown in Fig. 32.10, now represented in terms of the nominal stress against the extension ratio α. From [69] 1991 © American Chemical Society.

ratio or shear strain γ at which the upturn appears is seen to decrease with increase in weight% filler and as expected the maximum deformability was decreased. The behavior observed for shear is very similar to those observed for uniaxial and biaxial extension. However, shear moduli calculated using torsion measurements for PDMS–silica networks were significantly different from those for other types of deformation in that there is little evidence for upturns in the modulus at high deformation [72,73]. Shear modulus experiments have indicated that the presence of PDMS can dramatically shorten the incipient gelation time in PDMS–silica composites [62].

Impact Strength

The impact strength of a material is its ability to withstand the application of a sudden load which results in fracture. Impact strength of some PDMS–silica composites have been determined by the Charpy pendulum impact test and by the falling weight impact test. The composites thus tested had PDMS contents sufficiently low to produce composites with the brittleness required in impact strength testing. The higher the molecular weight or the larger the amount of PDMS introduced, the higher the impact strength. This can be explained by the fact that PDMS component can behave as an elastomeric phase because its glass transition temperature is well below the room temperature and when the material is subjected to an impact test, the PDMS component can absorb a great deal of energy delaying the growth of cracks and fracture. Increasing the amount of PDMS would increase the number of the phase-separated domains helping to absorb the impact energy. Impact strength values obtained using dart impact tests and energy of rupture obtained from the area under the curve of nominal stress versus elongation had a good correlation as measures of impact resistance [74,75].

Dynamic Mechanical Properties

Dynamic mechanical tests provide useful information on transition occurring in polymers including polymer–silica composites. Such results document the effect of filler on the glass transition temperature and on the melting point of the systems. For example, glass transition temperature determined by the peak temperature of the loss modulus curves for polyimide–silica composites indicated low T_g values compared to that of the original poyimide films for low silica contents up to 8 wt% followed by an increase of T_g with increase in silica content [15]. This could be explained by the fact that at low TEOS concentration, TEOS was polymerized incomplete in the polymer giving rise to low molecular weight silica which is more compatible with polyimide and as the TEOS concentration is increased further, high molecular weight silica is formed and the compatibility between silica phase and polyimide decreased giving rise to increase in T_g [15].

Tear Strength

Tear strength of a material is defined as the energy required to propagate a crack per unit area torn through. It has been shown that the tear strength is independent of the particular test method or the form of the test piece, thus it is an intrinsic property of the material under the given test conditions [76,77]. Tear strength measurements have shown that filled systems generally show a rather complicated tear behavior compared to that of unfilled systems [78,79]. Tear strength measurements conducted on PDMS–silica composites showed steady tearing at low rates of tearing similar to that observed for unfilled networks. However, at higher rates of tearing, somewhat unstable tearing behaviour was observed and it could be explained by the deviation of the tear path from the straight-ahead direction by curving around and stopping when it encounters a filler particle, followed by a possible new tear which then tend to repeat the same process [80]. As the amount of silica incorporated was increased, the tear strength increased as expected in agreement with the results for tensile measurements in which both the energy of rupture and ultimate strength were increased upon increase in the amount of silica.

REFERENCES

1. J. E. Mark, A. Eisenberg, W. W. Graessley, L. Mandelkern, E. T. Samulski, J. L. Koenig and G. D. Wignall, Physical Properties of Polymers, Second Edition, American Chemical Society, Washington, DC, 1993, pp. 48–53.
2. J. E. Mark and B. Erman, Rubberlike Elasticity: A Molecular Primer, John Wiley & Sons, NY, 1988, pp. 145–153.
3. B. Erman, and J. E. Mark, Structures and Properties of Rubberlike Networks, Oxford University, NY, 1997, pp. 265–306.
4. A. I. Medalia and G. Kraus, In Science and Technology of Rubber, J. E. Mark, B. Erman, and F. R. Eirich, Eds., Second Edition, Academic Press, NY, 1994, p. 387.
5. E. L. Warrick, O. R. Pierce, K. E. Polmanteer and J. C. Saam, Rubber Chem. Technol., **52**, 437 (1979).
6. B. B. Boonstra, Polymer, **20**, 691 (1979).
7. Z. Rigbi, Adv. Polym. Sci., **21**, 36 (1980).
8. L. Karasek and M. sumita, J. Mater. Sci., **31**, 281 (1996).
9. E. P. Giannelis, In Biomimetic Materials Chemistry, S. Mann, Ed., VCH Publishers, NY, 1996, p. 337
10. E. J. A. Pope and J. D. Mackenzie, J. Mater. Res., **4**, 1017 (1989).
11. C. J. T. Landry and B. K. Coltrain, Polym. Prepr., **32(3)**, 514 (1991).
12. C. J. T. Landry, B. K. Coltrain, J. A. Wesson, N. Zumbulyadis and J. L. Lippert, Polymer, **33**, 1496 (1992).
13. Y. Wei, D. Jin, G. Wei, D. Yang and J. Xu, J. Appl. Polym. Sci., **70**, 1989 (1998).
14. Z. Ahmad, M. I. Sarwar and J. E. Mark, **7(2)**, 259 (1997).
15. A. Morikawa, Y. Iyoku, M. Kakimoto and Y. Imai, Polym. J., **24**, 107 (1992).
16. J. E. Mark, J. K. Premachandra, C. Kumudinie, W. Zhao, T. D. Dang, J. P. Chen and F. E. Arnold, in Better Ceramics Through Chemistry VII: Organic/Inorganic Hybrid Materials, B. K. Coltrain, C. Sanchez, D. W. Schaefer, and G. L. Wilkes, Eds., Materials Research Society, Pittsburgh, PA 1996, vol. 435, p. 93.
17. J. Premachandra, C. Kumudinie, W. Zhao, J. E. Mark, T. D. Dang, J. P. Chen and F. E. Arnold, J. Sol–Gel Sci., **7**, 163 (1996)
18. C. J. Brinker and G. W. Scherer, Sol–Gel Science; The Physics and Chemistry of Sol–Gel Processing, Academic Press, NY, 1990
19. J. E. Mark and S. J. Pan, Makromol. Chem., Rapid Commun., **3**, 681 (1982).
20. S. J. Clarsn and J. E. Mark, Polym. Commun., **28**, 249 (1987).
21. J. E. Mark, Heterogeneous Chem. Rev., **3(4)**, 307 (1996).
22. J. E. Mark, Polym. Eng. Sci., **36(24)**, 2905 (1996).
23. H. Kaddami, F. Surivet, J. F. Gerald, T. M. Lam and J. P. Pascault, J. Inorg. Organomet. Polym., **4**, 183 (1984).
24. C.-C. Sun and J. E. Mark, J. Polym. Sci., Polym. Phys. Ed., **25**, 1561 (1987).
25. J. J. Fitzgerald, C. J. T. Landry and J. M. Pochan, Macromolecules, **25**, 3715 (1992).
26. C. J. T. Landry, B. K. Coltrain, M. R. Landry, J. J. Fitzgerald and V. K. Long, Macromolecules, **26**, 3702 (1993).
27. C. J. T. Landry and B. K. Coltrain, J. Macromol. Sci., Pure Appl. Chem., **31**, 1965 (1994).
28. Y. Wei, J.-M. Yeh, D. Jin, X. Jia and J. Wang, Chem. Mater., **7**, 969 (1995).
29. H.-H. Huang, G. L. Wilkes and J. G. Carlson, Polymer, **30**, 2001 (1989).
30. H. H. Huang, R. H. Glaser and G. L. Wilkes, In Inorganic and Organometallic Polymers, M. Zeldin, K. J. Wynne and H. R. Allcock, Eds, American Chemical Society, Washington, DC, 1994, vol. 360, p. 354.
31. D. Ravaine, A. Seminel, Y. Charbouillot and M. Vincens, J. Non-Cryst. Solids, **82**, 210 (1986).
32. T. Kyprianidou-Leodidou, W. Caseri and U. W. Suter, J. Phys. Chem., **98**, 8992 (1994).
33. S. Wang. Z. Ahmad and J. E. Mark, Polym. Bull., **31**, 323 (1993).
34. S. Wang. Z. Ahmad and J. E. Mark, in Better Ceramics Through Chemistry VI, A. K. Cheetham, C. J. Brinker, M. L. Mecartney, and C. Sanchez, Eds., Materials Research Society, Pittsburgh, 1994, vol. 346, p. 127.
35. M. Spinu, A. Brennan, J. Rancourt, G. L. Wilkes and J. E. McGrath, in Multi-functional Materials, D. R. Ulrich, F. E. Karasz, A. J. Buckley and G. Gallagher-Daggit, Eds., Materials Research Society, Pittsburgh, 1990, vol. 175, p. 179.
36. M. Nandi, J. A. Conklin, J. L. Salvati and A. Sen, Chem. Mater., **3**, 201 (1991).
37. A. Morikawa, Y. Iyoku, M. Kakimoto and Y. Imai, J. Mater. Chem., **2**, 679 (1992).
38. S. Wang. Z. Ahmad and J. E. Mark, Chem. Mater., **6**, 943 (1994).
39. L. Mascia and A. Kioul, Polymer, **36**, 3649 (1995).
40. L. Mascia and A. Kioul, J. Mat. Sci. Lett., **13**, 641 (1994).
41. Z. Ahmad, S. Wang and J. E. Mark, In Hybrid Organic Inorganic Composites, J. E. Mark, C. Y-C. Lee and P. A. Bianconi, Eds., 1995, American Chemical Society, Washington, DC, p. 291.
42. S. Wang and J. E. Mark, Macromolecular Reports, **A31 (Suppls. 3 & 4)**, 253 (1994).
43. D. E. Rodrigues, A. B. Brennan, C. Betrabet, B. Wang and G. L. Wilkes, Chem. Mater., **4**, 1437 (1992).
44. B. K. Coltrain, C. J. T. Landry, J. M. O'Reilly, A. M. Chamberlain, G. A. Rakes, J. S. Sedita, L. W. Kelts, M. R. Landry and V. K. Long, Chem. Mater., **5**, 1445 (1993).
45. Z. Pu, J. E. Mark, J. M. Jethmalani and W. T. Ford, Chem. Mater., **9**, 2442 (1997).
46. X. Ji, J. E. Hampsey, Q. Hu, J. He, Z. Yang and Y. Lu, Chem. Mater., **15**, 3656 (2003).
47. S. Wang, Z. Ahmad and J. E. Mark, Macromolecular Reports, **A31(Suppls. 3 & 4)**, 411 (1994).
48. J. Wen and J. E. Mark, J. Appl. Polym. Sci., **58**, 1135 (1995).
49. J. Wen and J. E. Mark, Rubber Chem. Technol., **67**, 806 (1994).
50. T. A. Ulibarri, G. Beaucage, D. W. Schafer, B. J. Oliver and R. A. Assink, Mat. Res. Symp. Proc., 274 (1992).
51. G. Beaucage, T. A. Ulibarri, E. P. Black and D. W. Schafer, In Hybrid Organic-Inorganic Composites, J. E. Mark, C. Y.-C. Lee and P. A. Bianconi, Eds., American Chemical Society, Washington, DC, 1995, p. 97.
52. J. M. Breiner and J. E. Mark, Polymer, **39**, 5483 (1998).
53. G. M. Jamison, D. A. Loy, R. A. Assnk and K. J. Shea, In Better Ceramics Through Chemistry VI, A. K. Cheetham, C. J. Brinker, M. L. Mecartney and C. Sanchez, Eds., Materials Research Society, Pittsburgh, 1994, vol. 346, p. 487.
54. D. A. Loy, R. J. Buss, R. A. Assink, K. J. Shea and H. Oviatt, In Better Ceramics Through Chemistry VI, A. K. Cheetham, C. J. Brinker, M. L. Mecartney and C. Sanchez, Eds., Materials Research Society, Pittsburgh, 1994, vol. 346, p. 825.
55. R. A. Assink and B. D. Kay, In Better Ceramics Through Chemistry, C. J. Brinker, D. E. Clark and D. R. Ulrich, Eds., Materials Research Society, New York, 1984, vol. 32, p. 301.
56. F. Surivet, T. M. Lam, J.-P. Pascautt and Q. T. Pham, Macromolecules, **25**, 4309 (1992).
57. M. Spinu and J. E. McGrath, J. Inorg. Organomet. Polym., **2**, 103 (1992).
58. L. Garrido, J. L. Ackerman and J. E. Mark, Mat. Res. Soc. Symp. Proc., **65**, 171 (1990).
59. L. Garrido, J. E. Mark, C. C. Sun, J. L. Ackerman and C. Chang, Macromolecules, **24**, 4067 (1991).
60. H.-H. Huang, B. Orler and G. L. Wilkes, Polym. Bull., **14**, 557 (1985).
61. G. B. Sohoni and J. E. Mark, J. Appl. Polym. Sci., **45**, 1763 (1992).
62. J. Wen and J. E. Mark, Polym. J., **27**, 492 (1995).
63. S. J. Clarson, J. E. Mark and K. Dodgson, Poly. Commun., **29**, 208 (1988).
64. V. Y. Levin, G. L. Solonimski, K. A. Andrianov, A. A. Zhdanov, Y. A. Godovski, V. S. Papkov and A. Y. Lyubavskaya, Polym. Sci., USSR, **15**, 256 (1963).
65. C. J. T. Landry, B. K. Coltrain, J. A. Wesson, N. Zumbulyadis and J. L. Lippert, Polymer, **33**, 1486 (1992).
66. C. Hall, Polymer Materials, An Introduction for Technologists and Scientists, 2nd edition, MacMillan Education Ltd., 1989, p. 96.
67. J. E. Mark, J. Appl. Polym. Sci., **50**, 273 (1992).
68. J. E. Mark, C. Y. Jiang and M. Y. Tang, Macromolecules, **17**, 2614 (1984).
69. S. Wang, P. Xu and J. E. Mark, Rubber Chem. Technol., **64**, 746 (1991).
70. P. Xu and J. E. Mark, Rubber Chem. Technol., **63**, 276 (1990).
71. P. Xu and J. E. Mark, J. Polym Sci., Polym. Phys. Ed., **29**, 355 (1991).
72. S. Wang, Ph.D. in Chemistry, University of Cincinnati, OH, 1991.
73. J. Wen and J. E. Mark, Polym. J., **26**, 151 (1994).
74. M.-Y. Tang, A. Letton and J. E. Mark, Colloid and Polym. Sci., **262**, 990 (1984).
75. J. E. Mark and Y.-P. Ning, Polym. Bull., **12**, 413 (1984).
76. R. S. Rivlin and A. G. Thomas, J. Polym. Sci., **10**, 291 (1953).
77. A. G. Thomas, J. Appl. Polym. Sci., **3**, 168 (1960).
78. L. C. Yanyo and F. N. Kelley, Rubber Chem. Technol., **60**, 78 (1987).
79. T. L. Smith, B. Haidar and J. L. Hedrick, Rubber Chem. Technol., **60**, 98 (1987).
80. C. Kumudinie and J. E. Mark, Mat. Sci. Eng., **C11**, 61 (2000).

CHAPTER 33

Physical Properties of Polymer/Clay Nanocomposites

Clois E. Powell and Gary W. Beall

Center for Nanophase Research, Texas State University, San Marcos, TX 78666

Polymer/clay nanocomposites have been reported since the 1960s and early 1970s [1–4]. However, when workers at the Toyota Central Research Laboratories reported a Nylon 6/clay nanocomposite that was utilized in a timing belt cover on the Toyota Camry [5–9], an expansion of activity with a wide range of polymer types was soon evident in the literature and conferences. The nylon 6/clay nanocomposites exhibited some very substantial enhancements of the physical properties of the composite relative to the pure nylon 6 polymer. These physical property improvements include substantial increases in tensile strength, modulus, and heat distortion temperature without loss of impact strength. The maintenance of the impact strength in these composites with substantial increases in strength and stiffness are surprising. Also, the decrease of water uptake and gas barrier improvements of the nanocomposites were substantially improved when compared to pure nylon. This series of papers initiated a huge research effort throughout the world on polymer/clay nanocomposites.

The ultimate clay nanocomposite is formed when individual clay plates are completely dispersed into a polymer matrix. This type of composite yields the maximum improvement in properties. This complete dispersion is normally referred to as full exfoliation. In many cases the composites reported in the literature are intercalated or partially exfoliated. Intercalated systems are characterized by insertion of polymer between plates of clay with retention of well-defined spacing distance between the plates. This spacing is called the gallery spacing and is determined from wide angle x-ray diffraction (WAXS). The x-ray diffraction pattern in many cases has been misleading in determining the level of intercalation/exfoliation. Disordered systems with a distribution of spacings mimic the pattern that an exfoliated system would yield. The only reliable technique for establishing the extent of exfoliation in nanocomposites is transmission electron microscopy.

The clays utilized in these composites belong to the smectite family of clays. These clays are characterized by a 2:1 structure built of a central layer of octahedrally coordinated metal, normally Al^{3+} or Mg^{2+}, sandwiched between two tetrahedral coordinated layers of silicon. Figure 33.1 is a model of this structure viewed from the edge of the plate. The morphology of these platy materials is characterized by a thickness of 1 nm. The two other dimensions are in the range of 100–1,500 nm. When dispersed as individual plates these materials exhibit surface areas of greater than $750\,m^2/g$. This large surface area and aspect ratio dominate the interaction of these materials with polymers. Complete separation of the plates is important to realize their full benefit. One must modify this surface to render the clay compatible with the polymer of interest. In clays of this type isomorphous substitution is quite common. The octahedral metal layer contains Al^{3+} which is replaced by Mg^{2+} or Fe^{2+} and Mg^{2+} is replaced by Li^{+}. Substitution can occur in the tetrahedral layer by exchanging Al^{3+} for Si^{4+}. Isomorphous substitution results in a charge imbalance in the structure. This is compensated by exchangeable cations on the surface of the clay plate shown in Fig. 33.1 as atoms

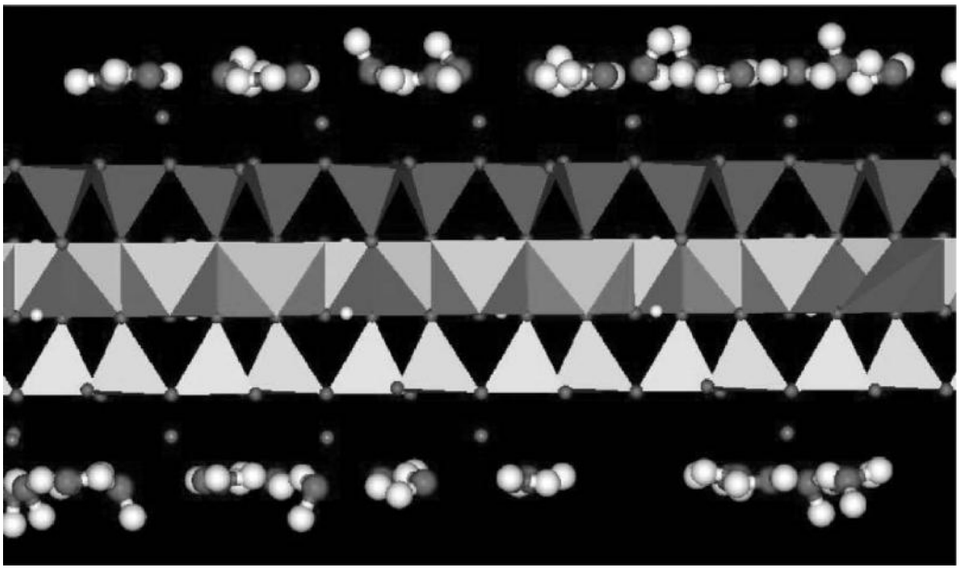

FIGURE 33.1. Representation of the two to one structure of montmorillonite showing the central octahedrally coordinated Aluminums sandwiched between two tetrahedrally coordinated silicons. Atoms above and below the layer are exchangeable cations and their associated waters of hydration.

slightly above and below the clay plate. The exchangeable cation is normally sodium, potassium, calcium, or magnesium. Sodium is preferred due to the ease of exchange reactions. The clay in its cation form is very hydrophilic and will disperse into aqueous solutions forming thixotropic gels. Figure 33.1 shows waters of hydration that normally surround the exchangeable cation. This hydrophilic character makes them suitable for polymer systems that are water soluble or dispersable such as polyvinylalcohol, polyethylene oxides, latex, and polyvinylpyrrolidone. In order to render these clays to be more compatible with more hydrophobic polymers ion exchange reactions utilizing organic onium ions are employed. The most common onium ions are quaternary ammonium ions. They are commercially available due to their use in the detergent industry. Most of these materials derived from natural fats and oils are hydrophobic. The surface of the clay can also be modified with organic molecules that contain appreciable dipole moments. These molecules do not ion exchange but form ion–dipole bonds to the exchangeable cation on the surface.

In most commercially available clay the average exchange capacity is in the range of 95 meq./100 g of clay. When this type of clay is exchanged fully with quaternary ammonium ions there is an appreciable amount of clay silicate surface still available for interaction with polymers. It has been reported that small amounts of selected polymers can be mixed with the quaternary amine prior to treating the clay with the resulting surface modified clay being more hydrophobic. The polymer apparently covers the silicate surface where exchange sites do not exist.

A fourth type of treatment is edge treatment with coupling agents. The edges of the plates are terminated in metal and silica hydroxides. These hydroxides act as a barrier to hydrophobic polymer entering the clay gallery for exfoliation. Silane coupling agents can react with these hydroxides via condensation reactions. Silane coupling agents are available with a variety of functional organic groups. This allows the edges of the plates to be tailored to the polymer of interest. The edge treatment appears to effect the kinetics of intercalation but not the ultimate formation of and characteristics of the final nanocomposite.

The use of surface modified clays to form polymer nanocomposites in a large variety of polymers has been thoroughly reviewed recently by Ray *et al*. [10]. In this chapter we will not attempt to cover in detail all of these nanocomposites but will describe the general physical properties observed for nanocomposites as a whole. The method of formation of these composites will also not be covered in detail. The majority of the examples will fall into two categories concerning the method of formation. The methods include in situ polymerization and melt compounding. In the case of in situ polymerization the polymer is being produced in the presence of the clay and in most cases is actually tethered to the clay surface. The melt compounding approach is normally accomplished by addition of the surface modified clay to a melt of the polymer in an extruder. The discussion will attempt to cover the engineering, barrier, and flame retardancy characteristics of polymer/clay nanocomposites and will be divided broadly into thermoplastics, thermosets, and rubbers.

33.1 ENGINEERING PROPERTIES OF THERMOPLASTIC/CLAY NANOCOMPOSITES

The engineering properties of polymer/clay nanocomposites in general exhibit substantial improvement in tensile strength, tensile modulus, flexural strength and modulus, heat distortion temperature, and in ideal cases no loss in impact strength. In some cases the improvements in strength and stiffness are also accompanied by improvements in elongation at break. These observed characteristics do not fit conventional polymer physics where increases in strength and stiffness are normally accompanied by loss in impact and elongation at break.

The thermoplastic that has been most extensively studied is nylon 6. This will serve as a basis for comparison of other polymer groups. Table 33.1 contains a compilation of data for Nylon 6 /clay nanocomposites from a number of sources. The first data is from Okada *et al*. [11] describing in situ produced nylon 6/ montmorillonite. The surface treatment was 12-aminolauric acid. The nylon 6 chains predominately grow from the surface of the clay. The tensile strength increases by 55% and the tensile modulus by 91%, and the heat distortion temperature increased by 134%. The impact strength showed no statistical change. The transmission electron micrographs (TEM) of this nanocomposite shows that the clay is almost totally exfoliated. The work reported by Fornes *et al*. [12] on melt compounding of organoclays into various molecular weight nylon 6 polymers can be compared to this data. Interpolation of the data to match the clay content of the in situ nylon 6 indicates that the tensile strength would show a 26% increase and the tensile modulus a 59% increase. These numbers are lower than the in situ polymerized composite. Detailed TEM analysis of these compounded samples showed that a large portion of the plates were exfoliated but that there was a significant number of aggregates containing two and three plates and infrequently ones with larger numbers of plates. The impact strength was retained as seen in the in situ material. The elongation at break dropped drastically in the compounded material. Melt compounding work by Hasegawa *et al*. [13] reported a tensile strength increase of 48% and tensile modulus increase of 71%. These numbers are extrapolated to match the 4.2% clay content of the in situ composite. These numbers are closer to those seen in the in situ material. TEM analysis showed almost complete exfoliation with some two and three layer agglomerates. The HDT increases by 80% uncorrected for clay content. In both in situ derived and melt compounded nanocomposites, substantial improvements in strength and modulus are realized. The increases seen in the in situ material yield the greatest increases possibly due to greater exfoliation. In order to predict modulus and HDT the theories of reinforcement in composites, Halpin–Tsai and Mori–Tanaka, has been applied to nylon 6 nanocomposites by Fornes [14]. The theoretical modulus (Mori–Tanaka) increase predicted in this paper for 4.2% clay loading is 56%. This is in very good agreement with the 59% observed for the melt processed nylon 6/montmorillonite nanocomposite [12]. The effect on modulus due to agglomerates was also calculated as a reinforcing factor (RF). The RF for fully exfoliated plates using Mori–Tanaka is 34.8 and for agglomerates containing two plates it is 23.8. This could be a viable explanation for the lower modulus seen in melt compounded material. The nylon 6 studied in the in situ composite had an inherently lower modulus [11]. When this lower value is utilized to predict a modulus for the in situ produced nanocomposite, a value of 2.0 GPa is predicted for a 4.2% clay containing nanocomposite. This is in excellent agreement with the measured 2.1 GPa. This would indicate that the differences

TABLE 33.1. *Physical properties of selected nylon 6 nanocomposites.*

Sample description	Clay (wt%)	Tensile strength (Mpa)	Tensile modulus (Gpa)	Impact strength (J/m)	HDT (°C)	Elongation at break (%)	Reference
Nylon 6	0	69	1.1	6.2*	65		
NCH-5	4.2	107	2.1	6.1*	152		[11]
Nylon 6LMW	0	69.1	2.82	36		232	[12]
NCH-LMW3	3.2	78.9	3.65	32.3		12	
NCH-LMW5	6.4	83.6	4.92	32		2.4	
Nylon 6 MMW	0	70.2	2.71	39.3		269	
NCH-MMW3	3.1	85.6	3.66	38.3		81	
NCH-MMW5	7.1	95.2	5.61	39.3		2.5	
Nylon 6 HMW	0	69.7	2.75	43.9		129	
NCH-HMW3	3.2	84.9	3.92	44.7		27	
NCH-HMW5	7.2	97.6	5.7	46.2		6.1	
Nylon 6	0	68	1.08	50	75		[13]
NCH-OC	1.8	82	1.41	42	135		
NCH-Slurry	1.6	82	1.38	44	102		

*Charpy impact kJ/m^2.

seen between in situ and melt compounded material is largely due to the differences in the moduli of the starting material and not slight differences in the level of exfoliation. The Halpin–Tsai theory was utilized successfully to predict the HDT of the nylon 6 nanocomposites [14]. This indicates that both melt compounded and in situ derived nanocomposites fits closely the composite theory of Mori–Tanaka. The Halpin–Tsai theory over estimated the modulus in all the clay nanocomposites but was very good at predicting the HDT increases. The theory predicts that polymer with lower the modulus will provide a greater increase in modulus in a fully exfoliated nanocomposite. Prediction of the lack of change in impact resistance in nylon 6 nanocomposites lies outside of the scope of the theory. This phenomena awaits further study to understand the mechanism.

The effect of larger increases in modulus for low modulus materials can be seen in dynamic mechanical analysis curves. The typical modulus increase seen in these curves below the T_g, on a percentage of starting modulus, is substantially lower than that seen above the T_g. This observation makes the large increases in HTD observed in nylon quite easy to rationalize.

Another polyamide that has been studied extensively is nylon 66. Table 33.2 contains a compilation of data on selected nylon 66/clay nanocomposites. In the case of nylon 66 all successful nanocomposites have been produced utilizing melt compounding. The average tensile strength increase, for the three selected composites at 5% clay loading, is 21% and tensile modulus of 46%. These increases are somewhat lower than that observed for nylon 6 nanocomposites. Chavarria and Paul [16] have applied the same modeling techniques that were used on nylon 6 to successfully predict the modulus of nylon 66. The Mori–Tanaka theory predicted the modulus of nylon 66 over a wider range than the Halpin–Tsai theory. Two of the studies reported an increase in impact strength [15,17]. As in the case of nylon 6 it appears that conventional composite reinforcing models do a reasonable job of predicting increases in modulus. As in nylon 6 the impact changes observed seem to go counter to experience with macroscale composites.

Lew *et al*. [18] has reported the production of a nylon 12 nanocomposite via melt compounding with synthetic fluoromica at 4% by weight loading. They reported an increase of 27% in tensile strength, 39% in tensile modulus, and a loss of only 9% in impact resistance. The magnitude of these changes seems to be in line with other polyamides. When one considers the very low modulus of the neat nylon 12, theory predicts a much greater change in modulus. The x-ray data indicates a high degree of intercalated structure as opposed to exfoliation. The most striking effect seen in this composite was an almost threefold increase in elongation at break. Fornes and Paul [19] have reported data on nanocomposites of nylon 11 and 12. At 4% by weight clay, the increase in tensile strength was 18% and 17% and tensile modulus was 56% and 51% for nylon 11 and 12, respectively. Comparisons with nylon 6 nanocomposites indicated that the level of exfoliation was much lower in nylon 11 and 12 than nylon 6. They did not observe the increase in elongation at break reported by Lew [18]. Impact strength decreased rapidly with increased clay loading. The data suggest that optimum increase in physical properties requires almost complete exfoliation.

For most polyamides, when close to full exfoliation exist, conventional composite theories do a very good job of predicting increases in strength, modulus, and HDT. The impact resistance, however, appears not to be explicable by these theories.

The physical properties of a number of other polymer nanocomposites made with clays have been measured. Table 33.3 contains a selection of reported values for some of the most common polymers. Poly(ethylene terephthalate) (PET) and Poly(butylene terephthalate) (PBT) are the most common commercial engineering polymers. The average increase in tensile modulus for most of the PET nanocomposites [21,22,24] is in the range of 35%. This is well below the prediction of a 95% increase for a 5% by weight nanocomposite utilizing Halpin–Tsai theory . The only exception was PET produced by in situ polymerization and tested as fibers [20]. In each one of these references it was acknowledged that full exfoliation had not been reached in the composite. It is reasonable to expect that substantial improvement in properties could be seen if full exfoliation were achieved. The reported increase in tensile modulus for PBT nanocomposites is only in the 36% range [23,24].

TABLE 33.2. *Physical properties of selected nylon 66 nanocomposites.*

Sample description	Clay (wt%)	Tensile strength (Mpa)	Tensile modulus (Gpa)	Impact strength (J/m)	HDT (°C)	Elongation at break (%)	Reference
Nylon 66	0	77	3	98	75		[15]
NCH66-5	5	97	4.75	145	140		
NCH66-10	10	107	5.25	140	168		
Nylon 66	0	72.6	2.91			211	[16]
NCH66-3	2.9	80.4	3.92			10	
NCH66-4	4.4	na	4.24			4	
Nylon 6	0	79	2.5	145		35	[17]
NCH66-6	4.4	90	3.1	208		10	

TABLE 33.3. *Physical properties of selected polyester and polyolefin nanocomposites.*

Sample description	Clay (wt%)	Tensile strength (Mpa)	Tensile modulus (Gpa)	Impact strength (J/m)	HDT °C	Elongation at break (%)	Reference
Polyesters							
PET	0	46	2.21			3	[20]
PETNC-3	3	71	4.1			3	
PET	0	32	2.55			370	[21]
PETNC-5	3.5	47	3.35			<5%	
PET	0	49	1.3				
PETNC-2	2	64	1.7				[22]
PBT	0	41	1.37				
PBTNC-3	3	60	1.76				[23]
PBTNC-5	5	49	1.86				
PBT	0		1.16				[24]
PBTNC-3	3		1.25				
PBTNC-5	5		1.35				
PBTSO3	0		1.08				
PBTSO3-5	5		1.48				
Polyolefins							
PP	0		1.5				[25]
PPNC-5	5		2.4				
PP	0	31	1.5(flex)	2	120		[26]
PPNC-3	3	39	2.1(flex)	3.4	130		
PP	0	37.9				1350	[27]
PPNC-2	2	39.4				36	
PE	0		0.183				[28]
PENC-3	3.5		0.258				
PE	0	28.9	0.26	66(dart)		945	[29]
PENC-1.5	1.5	30.2	0.31	57(dart)		860	
PE	0	26.1	0.8				[30]
PENC-5	5.4	33.1	1.67				
PE	0		0.19			>400	[31]
PENC-5	4.6		0.48			>400	
PE	0	21.1	0.649			773	[32]
PENC-6V	6	27.4	0.753			168	

Based upon Halpin–Tsai theory, a 5% loading of clay in PBT should increase the tensile modulus above 100%. Chisholm [24] claims that the PBT composite made with sulfated PBT was fully exfoliated. Therefore, the degree of exfoliation cannot be the reason for the low increase in modulus.

The results for polypropylene are worse than that observed for polyesters. All the nanocomposite work that is reported [25–27] acknowledges that the composites have very little exfoliation. The reported modulus increases are in the 50% range which are well below the 150% increase expected from composite theory.

Hotta and Paul [31] reported studies on melt compounding of many different organoclays into linear low density polyethylene and found that in some cases a 5% clay loading resulted in a 153% increase in modulus. The TEM images confirmed that the clay was largely exfoliated.

In general the most critical factor that governs the ultimate improvement in engineering properties in polymer/clay nanocomposites is the level of exfoliation. As full exfoliation is achieved in a composite, the modulus increase can be predicted using Halpin–Tsai or Mori–Tanaka theories. The prediction of impact strength and elongation at break of nanocomposites needs further study.

33.2 FLAME RETARDANCY OF POLYMER/CLAY NANOCOMPOSITES

The flammability of polymers in many applications is of critical importance. In the past, brominated flame retardant additives dominated this market. Concern over halogen containing compounds has resulted in the gain in popularity of various char forming phosphates. Recently clay nanocomposites were found to impart a substantial level of flame retardancy. The flame retardancy effect appears to originate from the clay's ability to contribute to char formation. This char layer forms an insulative layer to slow down heat transfer and retards movement of gases to feed the flame. Gilman [33] has recently reviewed this area. Figure 33.2

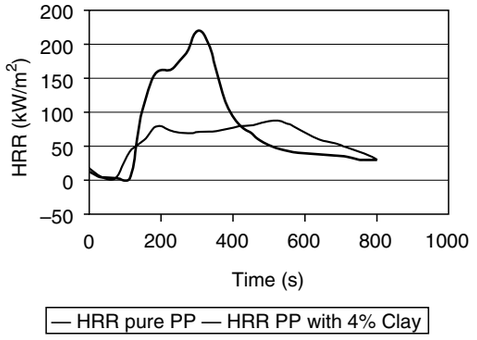

FIGURE 33.2. A plot of heat release rate (HRR) for pure polypropylene compared with a 4% loaded polypropylene/clay nanocomposite.

contains a typical cone calorimeter curve for a pure polymer compared to a nanocomposite of that polymer. In this figure several characteristics of polymer/clay nanocomposites can be seen in these type curves. The first is the reduction in both peak heat release rate (PHRR) and mean heat release rate (MHRR). It can also generally be seen that the time to ignition is also slightly lowered. Table 33.4 contains a compilation of selected cone calorimeter data for a number of polymer/clay nanocomposites compared to the pure polymer. The table contains several parameters of importance. The first is char yield, which obviously relates to char formation. The amount of char correlates directly to the amount of clay in the nanocomposite. Two other parameters of importance are the specific extinction area (SEA) and mean carbon monoxide yield. SEA relates to the amount of smoke produced when the sample burns. SEA data contained in the table has very mixed results. Gilman [33] shows an increase in smoke production; Song *et al*. [34] and Tidjani [35] report a reduction in smoke by the nanocomposites. The same mixed results is seen in carbon monoxide yield. Song *et al*. [34] also reports the synergistic effect of combining nanoclays and phosphate flame retardants. The table illustrates that intercalated systems seem to be similar to exfoliated composites. This is in marked contrast to parameters such as modulus discussed previously.

Based upon the many studies conducted on the flame retardancy of polymer/clay nanocomposites it appears that clay addition to a polymer system will improve its flame retardancy substantially. It also would appear that the flame retardancy can further be improved by combination with other flame retardants.

TABLE 33.4. *Flame retardancy data for selected polymer/clay nanocomposites.*

Sample	Residue yield (%)	Peak HRR (Δ%) (kW/m^2)	Mean HRR (Δ%) (kW/m^2)	Mean Hc (MJ/kg)	Mean SEA (m^2/kg)	Mean CO yield (kg/kg)	Reference
Nylon 6	1	1,010	603	27	197	0.01	[33]
Nylon 6 NC 2%	3	686 (32%)	390 (35%)	27	271	0.01	
Nylon 6 NC 5%	6	378 (63%)	304 (50%)	27	296	0.02	
Nylon-12	0	1,710	846	40	387	0.02	
Nylon-12NC 2%	2	1,060 (38%)	719 (15%)	40	435	0.02	
Polystyrene	0	1,120	703	29	1460	0.09	
PSNC-3%intercal. PS w/ DBDPO/	4	567 (48%)	444 (38%)	27	1730	0.08	
Sb_2O_3 30%	3	491 (56%)	318 (54%)	11	2580	0.14	
Polypropylene	0	1,525	536	39	704	0.02	
PPNC-2%intercal.	5	450 (70%)	322 (40%)	44	1028	0.02	
Polyurethane	0	923			1399	2.33	[34]
PU NC 5%	5.23	472			473	0.37	
PU+6%							
Melamine							
Polyphosphate	3.71	563			488	2.33	
PU NC 5%+6%							
Melamine							
Polyph.	9.47	243			415	0.33	
PP-MA	0	732		40.2	449	0.22	[35]
PP-MA-OD3M-5%	21	245 (66%)	40	389	0.025		
SAN		500					[36]
SAN NC 2%		450					
SAN NC 4%		420					
SAN NC 6%		340					
SAN NC 8%		320					

33.3 BARRIER PROPERTIES OF POLYMER/CLAY NANOCOMPOSITES

In many applications the gas barrier properties of polymers is critical. This is especially true in the food packaging industry. In many food packages the oxygen ingress determines the shelf life of the food in the package. In carbonated drinks the egress of carbon dioxide is the issue. It was recognized early in nanocomposite development that the high aspect ratios of clays could impart barrier to the composite. Nielsen [37] proposed a very simple model for the effect of platy materials on relative barrier performance. This model is commonly referred to as the tortuous path model. Figure 33.3 exhibits the effect of aspect ratio and clay loading on relative gas permeability of a composite utilizing this model. It can be seen that relatively low clay loadings can change the gas permeability greatly. There are a number of nanocomposites that come close to fitting the predictions of this simple model. Table 33.5 contains a listing of such composites. There are, however, a number of effects on permeability of nanocomposites that cannot be explained by this simple model and observed permeabilities that far exceed the predicted relative permeabilities. Lan *et al*. [41] observed in polyimide nanocomposites that the relative permeability for O_2, CO_2, and H_2O fit the tortuous path model reasonably well but measurements on ethyl acetate exhibited a very large dependence on relative humidity. The relative permeability of ethyl acetate at 0% RH was 0.19 and at 50% RH it was 0.09. In contrast the pure polyimides more than double its permeability going from 0 to 50% RH. Chaiko and Leyva [42] reported that in a polypropylene wax composite that they observed 62-fold decrease in oxygen permeability at 5% weight loading of clay. Beall [43] suggested a more complex model for gas permeability that attempts to take into account the change in properties of the polymer that interacts with the clay surface to form a constrained polymer region. This model was utilized to show that much of the data in the literature could be explained by the combination of tortuousity and constrained polymer regions. The theory awaits further experimental verification of the size and character of the constrained polymer region.

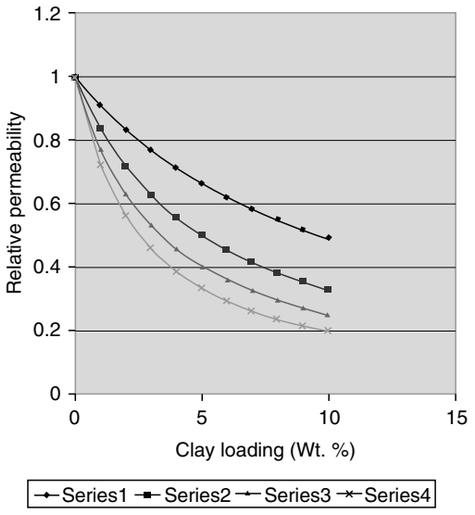

FIGURE 33.3. Relative gas permeabilty versus clay loading for polymer/clay nanocomposites per the model be Nielsen. The different curves represent aspect ratios of 50,100, 150, and 200 for series 1 to 4, respectively.

As a first approximation the simple model of Nielsen can be utilized to predict at least the minimum change in barrier properties one would expect from a polymer nanocomposite. One must use caution, however, since a substantial number of papers in the literature have observed performance far surpassing that predicted by the simple model.

33.4 THERMOSETS

There has been a considerable amount of work conducted on thermoset resin/clay nanocomposites. The overall trends seen in thermoplastics concerning engineering, flammability, and barrier properties are also seen in thermosets. Table 33.6

TABLE 33.5. *Gas permeability data for selected polymer/clay nanocomposites.*

		Permeant (Rel. Perm.)			
Sample	Clay %	Oxygen	Water	Hydrogen	Reference
Nylon 6	2	0.56	0.7	0.63	[5,9]
HDPE	3	0.65			[38]
PUU/Urea	2.5		0.7		[39]
	5		0.43		
	10		0.3		
	15		0.2		
Polylactic acid	4	0.35			[40]
	7	0.27			
	10	0.175			

TABLE 33.6. *Physical properties of selected thermoset nanocomposites.*

Sample description	Clay (wt%)	Tensile strength (MPa)	Tensile modulus (GPa)	Impact strength (kJ/m^2)	HDT (°C)	Elongation at break (%)	Reference
Epoxy 44	0	69	1.1	2.3	65		[5]
Epoxy 44 intercal.	5	61	1	2.2	89		
Epoxy 44 exfoliat.	4.2	107	2.1	2.8	145		
Epoxya 45	0	36	2.1				[44]
Epoxya 45 NC2.5	2.5	38	2.4				
Epoxya 45 NC5	5	24	2.73				
Epoxya 45 NC10	10	20	3.95				
Epoxyb 45	0		3.2				
Epoxyb 45 NC5	5		3.95				
PU 46	0	29	0.98			255	[45]
PU 46 NC1	1	33	1.26			200	
PU 46 NC3	3	34	1.3			190	
PU 46 NC%	5	35	1.5			190	

contains selected physical data on several epoxies [5,44] and one polyurethane [45]. The magnitude of change in modulus and HDT are certainly in line with values seen for thermoplastics. The greatest complication in thermosets, however, is the control of crosslink density in the pure systems as compared to the nanocomposites. As an example Fig. 33.4 contains the DMA of a flexible epoxy and its corresponding nanocomposite. As is the case with thermoplastics there is an increase in modulus below the T_g and a relatively larger percentage increase above the T_g. In contrast to thermoplastics there is a substantial shift in T_g between the pure epoxy and the nanocomposite. It would be reasonable to attribute this to a change in crosslink density since large T_g shifts have not been observed in thermoplastics. This complicates greatly any attempt at theoretically predicting changes that will occur in nanocompositing of thermosets. Uhl *et al.* [45] has measured the effect of clay on crosslink density in a polyurethane nanocomposite. The control polyurethane had a crosslink density of 6.4 (10^{-3}mol/cm^3) while the composites

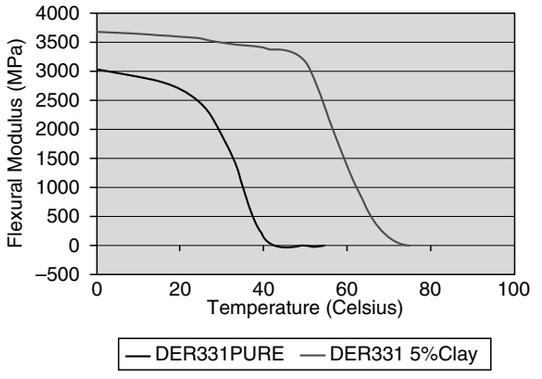

FIGURE 33.4. Comparison of flexural modulus between a pure epoxy and a 5% loaded epoxy/clay nanocomposite utilizing dynamic mechanical analysis.

containing 5% clay gave an average of 8.1. This is a 26% increase which is very close to the average increase in modulus of 28%. It appears that the clay either promotes the crosslinking reaction or acts as a crosslinker.

33.5 RUBBER NANOCOMPOSITE

Rubber is an important worldwide commodity. The worldwide consumption of rubber in 2003 was about 18.97 million metric tones. This consumption can be divided into two major categories, natural and synthetic. The synthetic rubber category is about 58.6% of the total. Of the diverse markets that utilize rubber, approximately 50% of the total rubber consumption goes into tire production.

The benefits identified earlier that relate to nanocomposite reinforcement also applies to rubber as well as increased barrier properties. One of the unique parameters for rubber that is of great importance is hysteresis. Decreased hysteresis at high temperature relates directly to lower rolling resistance for tires. A car, for example, will expend 5–15% of total fuel energy to overcome the rolling resistance of its tires. Heavy trucks will use 15–30% of their fuel to overcome tire rolling resistance. An increase in hysteresis at lower temperature provides for increased tire adhesion to icy and snow covered roads. A combination of lower rolling resistance at higher temperatures and increased adhesion at lower temperature will add value to all weather tires, for example.

Carbon black as a reinforcing additive has been employed in rubber manufacture for many years. One may argue that carbon black provides nanoparticle reinforcement for rubber. There are many reviews available on carbon black use in rubber.[46] We will focus on recent advancements in nanoparticle reinforcement. These advancements do not include carbon black. Most of the recent advancements in nanoparticle reinforcement in rubber have focused on montmorillonite clay.There are several reviews on rubber

nanocomposites found in the open literature in other languages the only one in English, however, is by Karger-Kocsis [47].

This chapter will divide the advancements in rubber nanocomposites as a function of polymer type. One should be aware that polymer blending is very prevalent in commercial applications of rubber. For example, a tire can contain eight different polymer types.

33.5.1 Styrene–Butadiene Nanocomposites

Styrene–butadiene copolymers are extremely important to the rubber industry. They are particularly important in tire manufacture. Styrene–butadiene polymer is produced by emulsion polymerization and solution polymerization. Most of the volume is by emulsion polymerization. This affords the opportunity to prepare polymer nanocomposites by several avenues. One can blend an aqueous dispersion of the nanoparticles with the styrene–butadiene latex before flocculation to produce the rubber crumb, disperse an organically treated nanoparticle in the styrene–butadiene solution polymer before the solvent is stripped from the polymer, disperse the organically treated nanoparticles into the monomers, or prepare the rubber nanocomposite in the traditional compounding approach. One finds all of these approaches in the literature. One also finds functional modifications of the styrene–butadiene polymer in the literature designed to improve the efficiency of the dispersion and interaction of the nanoparticles with the polymer.

Manoj Ajbani *et al*. [48] describes the value of amine functional block copolymers of styrene–butadiene with montmorillonite clay to prepare rubber nanocomposites. Light weight composites were evaluated with pure montmorillonite, Cloisite NA, and montmorillonite exchanged with tallow, bis(2-hydroxyethyl) methyl quaternary ammonium chloride. The focus of the work is to improve traction, tread wear, and rolling resistance of tires with a reduction of the weight of the tire. The two areas of the tire where these rubber–clay nanocomposites are applicable are the tread for lower rolling resistance and increased traction and the tire side-walls for increased flexibility with enhanced tensile strength. Cloisite 30B demonstrated a significant increase in performance at 5 phr. Transmission electron microscopy (TEM) indicated partial exfoliation of the clay into the polymer.

Parker *et al*. [49] altered the stabilization mechanism for styrene–butadiene latex prepared by emulsion polymerization from anionic to cationic so that they could get a spontaneous flocculation with aqueous montmorillonite slurry and the latex. Evaluation of the rubber nanocomposite prepared in this manner gave dramatic increases in modulus, strength, percent elongation, and decrease in hysteresis.

Sarashi [50] intercalates montmorillonite with styrene and butadiene monomer before polymerization. After the clay–monomer dispersion is polymerized to form the styrene–butadiene nanocomposite, the rubber nanocomposite is compounded with natural rubber to provide a composite with good break strength and bending fatigue resistance.

Only limited success has been achieved in compounding organomontmorillonites with styrene–butadiene rubber to prepare rubber nanocomposites [51]. Knudson *et al*. [51] discovered that flocculation of the aqueous blend of styrene–butadiene latex and montmorillonite gives an exfoliated clay–rubber nanocomposite. The approach offers the most convenient and effective method for the preparation of clay–styrene–butadiene rubber nanocomposites.

To confirm the relationship of exfoliation of montmorillonite in styrene–butadiene rubber to mechanical properties, Sadhu *et al*. [53], dissolved styrene–butadiene rubber into toluene and dispersed organically treated montmorillonite and untreated montmorillonite into the polymer solution at 4% concentration based on polymer. The organoclay was prepared by the exchange of octadecyl amine. The toluene was removed by evaporation. The degree of exfoliation of the polymer nanocomposites was measured by wide angle x-ray diffraction WAXS. The untreated clay was intercalated with polymer; the organically treated clay was fully exfoliated. The exfoliated rubber nanocomposite has significantly improved tensile strength, elongation at break, energy to break, and modulus at 50% elongation when compared to the intercalated rubber nanocomposite. Both rubber composites had superior mechanical performance when compared to the pure rubber. In a previous publication by Mousa *et al*. [54], the same organoclay that was utilized in the above publication by S. Sadhu was compounded with styrene–butadiene up to 10 phr and cured. The rheology of the polymer nanocomposite demonstrated shear rate thinning behavior. This is common with montmorillonite dispersed systems. The mechanical properties were as predicted except for the increase in percent elongation to failure as a function of clay loading. The percent elongation to failure increased along with modulus and tensile strength. This is not expected or predicted by standard reinforcing theories. For example, carbon black loaded polymer does not behave in this manner. The crosslink density was measured by swelling the composite and utilizing the Flory–Rehner equation. The crosslink density increase with organoclay loading indicated that the amine could be participating in the cure. The authors speculate that two distinct polymer morphologies develop. A higher crosslinked polymer morphology is associated with the clay particles and a lower crosslinked density polymer is associated with the bulk of the rubber composite. Ganter *et al*. [55], prepared organoclay–styrene–butadiene rubber nanocomposites in a similar fashion to Sahdu by dispersing the rubber and organoclay in toluene and evaporating the solvent to prepare the rubber nanocomposite. In addition, they utilized a sulfur functional silane(bis(triethoxysilylpropyl)-tetrasulfan to further enhance the crosslinking during cure. Transmission electron microscopy indicated intercalated and partially exfoliated montmorillonite in the rubber. They saw increased

hysteresis with clay loading. WAXS indicated that the montmorillonite was changing orientation, i.e., sliding past one another, during cyclic tensile testing. Sadhu *et al*. [56], examined the role of the chain length of the amine exchanged on montmorillonite with respect to exfoliation and mechanical properties when dispersed in styrene–butadiene. Amines with longer chain length exfoliated to a greater extent and resulted in improved mechanical performance of the rubber nanocomposite. Subsequent work by Sadhu *et al*. [57], with octadecyl amine exchanged montmorillonite exfoliated into styrene–butadiene indicated that the styrene content of the polymer was a significant variable with respect to mechanical properties. The styrene–butadiene polymer with the greatest styrene content, i.e., 40%, demonstrated a much greater increase in strength, i.e., 53%, as a rubber nanocomposite than the polymers with 23% styrene, 38% increase in strength, and 15% styrene, 13% increase in strength. An extension of the work [58] evaluated the significance of the cure system to the development of mechanical properties and found little effect of the type of cure system but longer cure time provided for improved mechanical properties. Bala *et al*. [59] evaluated dodecylamine exchanged montmorillonite compounded into styrene–butadiene. The WAXS indicated less that perfect exfoliation into the rubber. However, the tensile strength, modulus, and elongation at break increased significantly at 4% loading of the organoclay when compared to the unfilled rubber. Crosslink density increased in the rubber composite as a function of organoclay concentration.

Wang *et al*. [60] utilized positron annihilation lifetime spectroscopy to measure the polymer free volume in montmorillonite–styrene–butadiene rubber nanocomposites. There was an apparent reduction of the free volume of the polymer in the nanocomposite. The authors speculated that the reduction was primarily at the clay surface. This information is consistent with the crosslink density results reported above.

Molesa *et al*. [61] compared compounded styrene–butadiene nanocomposites with polymer nanocomposites that were prepared by blending the latex with an aqueous dispersion of the montmorillonite. The loading of the dispersed phase was at 10 phr. The initial results are consistent with the information found above. The flocculated rubber nanocomposite from the aqueous blend has superior strength properties when vulcanized and compared with the rubber nanocomposite prepared by compounding. Montmorillonite that was organically treated demonstrated superior tensile strength when compared with rubber compounded with silica.

Ganter *et al*. [62], utilized a synthetic layered fluorohectorite silicate and organomontmorillonite to evaluate the role of functional rubber exchanged onto the synthetic clay in the preparation of styrene–butadiene rubber nanocomposites. The functional rubber that was exchanged onto the fluorohectorite was amino-terminated polybutadiene. The styrene–butadiene was dispersed in solvent and then dispersed with the organoclays. Break strength, tensile strength, and hysteresis correlated with transmission electron microscopy determination of particle morphology. The particles were intercalated with polymer or partially exfoliated. Orientation of these highly anisotropic clay particles correlated with the mechanical properties of the rubber nanocomposites.

Zhang *et al*. [63] prepared styrene–butadiene nanocomposites by dispersing an aqueous dispersion of montmorillonite and latex and flocculating the dispersion with acid. The performance of the rubber nanocomposites were compared with clay, carbon black, and silica rubber composites prepared by standard compounding methods. The montmorillonite loadings for the rubber nanocomposite were up to 60 phr. The morphology of the rubber nanocomposites by transmission electron microscopy appears to indicate intercalated structures. The mechanical properties of the rubber nanocomposites were superior to all of the other additives up to about 30 phr. However, rebound resistance was inferior to all of the additives except silica. The state of cure was not evaluated.

33.5.2 Butyl Rubber Nanocomposites

Butyl rubber is the most expensive polymer utilized in tire manufacture. The primary use for butyl rubber is for the inner liner of a tire. The inner liner of the tire maintains air pressure in the tire for an extended period of time. Oxygen diffusing into the carcass of the tire from the inside will degrade the tire just as oxygen from the outside of the tire degrades the sidewalls of the tire. Butyl rubber has low mechanical durability and a relatively high specific gravity. There is a clear need for a butyl rubber nanocomposite with increased toughness and barrier resistance. Lower butyl rubber content through the use of a nanocomposite will make the tire more cost effective and increase operation efficiency without a compromise in safety and durability.

Butyl rubber is exclusively made by a solution polymerization process. Hence, nanoparticles can only be introduced as a dispersion with the butyl polymer before the solvent is removed, with the monomer, or in a standard compounding protocol. Butyl rubber is prepared from isobutylene. There are no double bonds available for cure after polymerization. A small amount of isoprene is added to the polymerization process to provide for the double bonds necessary for cure. Bromination of the polymer is also done to provide crosslinking sites.

A patent application by Maruyama *et al*. [64], teaches that anhydride modification of the butyl rubber improves the exfoliation of amine exchanged clays. This combination produces exfoliated clay–butyl rubber nanocomposites. These nanocomposites have excellent barrier performance.

Hagiwara *et al*. [65], prepares the butyl rubber nanocomposite from the polymer solution. The polymer is prepared

by solution polymerization in toluene. The polymer solution is then emulsified in water with the aid of anionic surfactants and alcohol coupling solvents. The solvent and coupling solvent is removed by reduced pressure. The aqueous dispersion of butyl rubber is blended with an aqueous dispersion of clay. The water is then removed by reduced pressure. The resultant clay–butyl rubber nanocomposite demonstrated good barrier resistance.

Work done by Gong *et al*. [66] is similar to the work by Maruyama *et al*., above. They functionalize butyl rubber with succinic anhydride to improve the compatibility of butyl rubber with an organoclay. Barrier performance of the rubber nanocomposite increases with the amount of succinic anhydride modification. In a companion publication [67], butyl rubber is functionalized by grafting maleic anhydride onto the polymer chain with peroxide. The same organoclay is utilized in this work as well to form the rubber nanocomposite. Barrier performance of the butyl rubber is significantly enhanced.

Ishida *et al*. [68], determined that organoclay compounded into halogenated butyl rubber, e.g., brominated copolymer of isobutylene and methyl styrene, provides a rubber nanocomposite with a lower air permeability index, i.e., 85, than the pure brominated butyl rubber. Yagi *et al*. [69] found that the addition of epoxidized natural rubber to the formula with halogenated butyl rubber provided for the successful utilization of clay and mica to form a butyl rubber nanocomposite with reduced air permeability, i.e., $9 \times 10{-}11$ cc cm/cm^2 s cmHg. Maiti *et al*. [70] evaluated montmorillonite exchanged with amines in brominated butyl rubber. TEM and WAXS indicated good exfoliation of the organoclay in the polymer. Tensile strength, elongation to break, and modulus were significantly greater for the rubber nanocomposites when compared to the pure rubber. Mruyama *et al*. [71] teaches that montmorillonite exchanged with long chained amino acids disperses well in brominated butyl rubber to produce rubber nanocomposites that provide good barrier to air. Tsou *et al*. [72] discovered that the addition of nylon or nylon–organoclay nanocomposites to the bromobutyl rubber–organoclay nanocomposite also enhances barrier properties.

33.5.3 Natural Rubber Nanocomposites

Natural rubber composition is polymerized *cis*-1,4-polyisoprene. However, synthetic attempts of duplicating natural rubber have been largely unsuccessful. Natural rubber is the largest polymer component of a tire. The preparation of natural rubber nanocomposites will add value to a very large segment of the rubber industry. Because natural rubber can be obtained as an aqueous dispersion from the rubber tree and as a dried solid phase, one can disperse an aqueous dispersion of nanoparticles into the latex before drying or compound the organic modified nanoparticles into the solid phase to obtain the rubber nanocomposite.

Larson [73] teaches that one can successfully compound organoclays into natural rubber. One obtains a homogeneous distribution of intercalated and exfoliated clay particles. The benefits of the rubber nanocomposite are high storage modulus with a small increase in hysteresis. Ajbani *et al*. [74] used maleic anhydride functional polybutadiene as a compatibilizer for clay incorporation into natural rubber. The organoclays were predispersed with maleic anhydride functional polybutadiene before compounding with natural rubber. The mechanical properties were excellent. The fatigue to failure cycles with the Monsanto FTF tester were especially high.

Jeon *et al*. [75] employed rheology to identify structure–property relationships of clay–natural rubber nanocomposites. The rubber nanocomposites were prepared by dispersing the rubber and organoclay in toluene. Upon evaporation of the solvent, x-ray, small and wide angle, and TEM indicate good exfoliation of the clay in the rubber. Weight concentrations of the clay varied between 1 and 9.2%. Dynamic viscosity, storage modulus, and loss modulus were determined. In the range of 3–4 wt% loading of clay, one apparently sees an interaction between the clay and the rubber that suggests chain entanglement with the clay. Above this concentration, the rubber composite seems to behave as a ''pseudosolid,'' i.e., a frequency independent, storage modulus.

Yaakub *et al*. [76], prepared natural rubber–clay nanocomposites by blending an aqueous dispersion of the clay with an aqueous dispersion of the rubber and flocculating the dispersion with other additives for cure. Hectorite and montmorillonite were evaluated. Mechanical properties improved as well as an increase in coefficient of friction and abrasion resistance.

Kgawa *et al*. [77], found that a dispersion of organoclay and epoxy functional rubber compounded into natural rubber resulted in an increase of modulus and tensile strength.

Lopez-Manchado *et al*. [78] prepared natural rubber nanocomposites with organoclay prepared from saponite. The polymer and organoclay were dispersed in organic solvent. The solvent was evaporated to yield the rubber nanocomposite with intercalated clay nanoparticles. A silane coupling agent was also evaluated with the rubber nanocomposite. The loading level of clay in the rubber was about 10 phr. Mechanical properties improved significantly. Further improvement in mechanical properties was observed when the silane coupling agent was present.

Varghese *et al*. [79,80], observed that pure, synthetic sodium fluorohectorite does not disperse well into natural rubber. However, when polyurethane rubber was dispersed with the clay and natural rubber, excellent mechanical properties were observed when the clay was present at 10 wt%. The clay preferred to be associated with the urethane dispersed phase.

Varghese *et al*. [81–84] evaluated pure montmorillonite, kaolin, and synthetic fluorohectorite by mixing an aqueous dispersion of clay, an aqueous dispersion of natural latex,

and curative additives and then drying the mixture to prepare the rubber nanocomposite. Fluorohectorite rubber nanocomposite demonstrated the best dispersion of the clay and best mechanical properties. Epoxidized natural rubber was evaluated with pure clays and several organoclays. Standard compounding methods were used to prepare 10% clay loaded rubber nanocomposites. Octadecylamine exchanged montmorillonite demonstrated the best tensile strength, modulus, and tear strength. WAXS and TEM indicated that the octadecylamine exchanged montmorillonite probably had the best dispersion in the rubber.

Magaraphan *et al*. [85] evaluated organoclays prepared from amines and quats with carbon chain lengths that varied from 12 to 18 with natural rubber. The rubber and organoclays were dispersed in toluene and then the solvent was evaporated. Based on WAXS and TEM, exfoliation of the clay in the polymer was observed up to 10 wt%. Above that concentration, the organoclays seemed to be intercalated. The amine exchanged clays with the longer hydrocarbon chains provided rubber nanocomposites that had superior mechanical performance when compared to the rubber nanocomposites prepared with the quat exchanged clays with the same hydrocarbon chain.

Vu *et al*. [86], reports similar work to that of Varghese above with montmorillonite, natural rubber, and epoxidized natural rubber. The rubber nanocomposites were prepared by compounding the clay with the rubber or dissolving the rubber in toluene or methyl, ethyl ketone, dispersing the clay in the solution, and evaporating the solvent to produce the rubber nanocomposite. Pure montmorillonite and organically modified montmorillonite were evaluated. Natural rubber and natural rubber epoxidized with 25 or 50% mole percent epoxide were evaluated. Mechanical properties are similar to those reported by Varghese above and correlate with the x-ray diffraction results. Organic modification of the montmorillonite results in improved intercalation and exfoliation in the rubber. Greater intercalation and exfoliation of the clay resulted in improved mechanical performance.

Joly *et al*. [87], prepared natural rubber nanocomposites by compounding organoclays at 10 wt% loading. The rubber nanocomposites were characterized by small angle x-ray scattering, scanning, and TEM, mechanical properties, birefringence, infrared dichroism, and crosslink density by swelling in toluene. The clay in the rubber was intercalated and exfoliated. The organoclays were very efficient in reinforcing the rubber. The clay also appears to increase the crosslink density of the rubber.

33.5.4 Acrylonitrile-Butadiene (NBR) and Hydrogenated Acrylonitrile (HNBR) Rubber Nanocomposites

Because of the thermal stability and chemical resistance of NBR and HNBR rubber, their application areas include power transmission, i.e., belts, etc., blow out preventors, packer seals, stators, fuel hoses, engine seals, and gaskets. HNBR has improved thermal stability and exterior durability but sacrifices low temperature flexibility when compared to NBR.

Akelah *et al*. [88], prepared a NBR nanocomposite by blending an aqueous dispersion of montmorillonite with a dioxane solution of amine terminated NBR. The solvent was evaporated to product the rubber nanocomposite. WAXS and TEM indicated intercalated clay morphology in the rubber. No mechanical properties were reported. Okada *et al*. [89], also prepared NBR by blending an aqueous dispersion of montmorillonite with an *N*,*N*-dimethyl sulfoxide–ethanol solution of amine terminated NBR. The solvent was evaporated away to produce the rubber nanocomposite. This nanocomposite was compounded into NBR to produce NBR–clay nanocomposites at 5 and 10 phr clay. TEM indicates an intercalated morphology for the clay in the rubber. When compared to carbon black loaded NBR at 20 and 40 phr, the Mooney viscosity of the rubber nanocomposites decreases with increased clay loading; carbon black loaded rubber always results in increasing viscosity with increased loading. Mechanical properties indicated that the clay was about four times more efficient at reinforcing NBR when compared to carbon black. The moisture and hydrogen permeability of these NBR nanocomposites were reported in a subsequent puplication [90]. Barrier properties of the clay–NBR nanocomposites are significantly superior to the carbon black filled NBR. The anisotropic-plate structure of the clay provides for this enhanced barrier.

Pazur [91] found that compounding carboxyl functional HNBR (HXNBR) with HNBR, carbon black, and 5 phr. Organoclay in a standard rubber formula provided a rubber nanocomposite with superior mechanical, barrier, and cure performance when compared to HNBR alone. A variety of organoclays and pure montmorillonite were evaluated with a 75/25 ratio of HNBR/HXNBR and 70 phr carbon black.

Previously mentioned work by Sadhu and Bhowmick evaluated NBR nanocomposites as a function of acrylonitrile content and organoclay loading. The rubber was dispersed into chloroform; the organoclay were dispersed into ethanol. The dispersions were blended and dicumyl peroxide was added for cure. The solvent was evaporated to produce the rubber nanocomposite. The acrylonitrile content of the rubber was 19, 34, and 50%. The organoclay content was evaluated at 2, 4, 6, and 8%. TEM and WAXS confirmed intercalated structure of the clay in the rubber. The general trend was the rubber with the highest acrylonitrile content provided the best mechanical performance. The tensile strength increased as a function organoclay concentration. Interestingly, for the 50% acrylonitrile containing rubber, the elongation to failure also seemed to increase as a function of organoclay content. Kim *et al*. [92] also evaluated octadecyl amine exchanged montmorillonite in NBR. The rubber nanocomposites were prepared by compounding. The role of 3-(mercaptopropyl)trimethoxysilane

coupling agent was also evaluated in the formula. The rate of cure and barrier to water vapor increased as a function of increasing clay and coupling agent content. Nah *et al*. [93] found similar mechanical properties with NBR with various organoclays. The rubber nanocomposites were prepared by compounding. The structure of the montmorillonite in the rubber was intercalated.

33.5.5 Ethylene–Propylene–Dimer Rubber Nanocomposites

Ethylene–propylene–dimer (EPDM) rubber has a good balance of toughness, durability, chemical resistance, and barrier performance that makes this rubber suitable for the manufacture of parts for power transmission, i.e., belts, etc., gaskets, and hoses. EPDM also has utility as a dispersed phase to toughen thermoplastics.

Gatos *et al*. [94], evaluated compounding processing variables, the role of functionality on the EPDM, and cure additives in relation to mechanical performance and the degree of dispersion of the clay in the rubber nanocomposite. Clay loading for the study was 10 phr. Superior tensile strength and modulus was achieved with a 1% maleic anhydride grafted EPDM with an internal mixer at elevated temperature, i.e., 100 °C. Better mechanical properties were obtained with the rubber nanocomposite when the zinc oxide and stearic acid was added to compounding on an open mill rather than added to the internal mixer. The accelerator, zinc diethyldithiocarbamate, provided the best mechanical performance in the formula. WAXS and TEM indicated that functionalized EPDM with maleic anhydride and glycidyl methacrylate increases the compatibility of the organoclay with the rubber. The morphology appears to be intercalation with the possibility of some exfoliation. Usuki *et al*. [95], also evaluated EPDM with octadecylamine exchanged montmorillonite. The rubber nanocomposite was prepared by compounding 7 phr of the organoclay into the rubber. The nature of the accelerator was found to be a significant variable in regard to the degree of dispersion of the organoclay in the rubber. Exfoliation of the organoclay appears to occur in the EPDM when the accelerators were zinc dimethyldithiocarbamate and tetramethylthiuram monosulfide based on the WAXS and TEM. The exfoliated rubber nanocomposites were significantly superior in mechanical properties and barrier performance when compared to the intercalated rubber composites. The exfoliated rubber nanocomposites demonstrated approximately two times the tensile strength, percent elongation to failure, and modulus when compared to the unfilled, cured rubber. The barrier performance based on nitrogen permeability was improved approximately 30% when compared to the unfilled, cured rubber. A series of publications by Zhueng *et al*. [96–105] focus on evaluating the role of quat surface treatment of montmorillonite in the dispersion of organoclays in EPDM. Montmorillonite exchanged with alkyl hydroxyl functional quats exfoliate in EPDM by standard compounding procedures. The other quat treatments on montmorillonite result in intercalated structures in the EPDM. The mechanical properties of the organoclay–EPDM nanocomposites significantly increased when compared to the cured rubber without reinforcing additives. Exfoliated structures demonstrated superior mechanical performance compared to intercalated morphologies. Loading levels up to 15 phr. were evaluated. At that loading level, exfoliated rubber nanocomposites demonstrated a factor of 3–4 times improvement in mechanical performance compared to the cured rubber without reinforcement. They also found that maleic anhydride grafted EPDM of at least 5.2 wt% improved the exfoliation efficiency of the organoclays and subsequent mechanical properties of the rubber nanocomposites. Comparisons of sulfur cure with peroxide cure, i.e., 2,5,-dimethyl-2, 5-di- *tert*-butylperoxyhexane, with the organoclay–EPDM nanocomposites indicated that sulfur cure produced exfoliated structures and peroxide cure of the same nanocomposite produced intercalated structures. The sulfur cured nanocomposites had lower crosslink density than the peroxide cured nanocomposites. Improved barrier performance of oxygen by the rubber nanocomposites was also determined.

REFERENCES

1. Friedlander, H. Z., *ACS Div. Polym. Chem. Reprints* (1963), **4**, 300–306.
2. Soloman, D. H., Luft, B. C., *J. Appl. Polym. Sci*. (1968), **12**, 1253–1262.
3. Blumstein, A., Blumstein, R., Vanderspurt, T. H., *J. Colloid Intef. Sci*. (1969), **31**, 236–247.
4. Blumstein, A., Parikh, K. K., Malhotra, S. L., *J. Polym. Sci*. (1971), **A2**, 1681–1691.
5. Kojima, Y., Usuki, A., Kawasumi, M., Okada, A., Fukushima, Y., Kurauchi, T., Kamigaito, O., *J. Mater. Res*. (1993), **8**, 1185–1189.
6. Kojima, Y., Usuki, A., Kawasumi, M., Okada, A., Kurauchi, T., Kamigaito, O., *J. Appl. Polym. Sci*. (1993), **49**, 1259–1264.
7. Kojima, Y., Fukumori, K., Usuki, A., Okada, A., Kurauchi, T., *J. Mater. Sci. Lett*. (1993), **12**, 889–890.
8. Usuki, A., Kawasumi, M., Kojima, Y., Okada, A., *J. Mater. Res*. (1993), **8**, 1174–1178.
9. Usuki, A., Kojima, Y., Kawasumi, M., Okada, A., Fukushima, Y., Kurauchi, T., Kamigaito, O., J. Mater. Res. (1993), **8**, 1179–1184.
10. Ray, S. S., Okamoto, M., *Prog. Polym. Sci*. (2003), **38**, 1539–1641.
11. Okada, A., Usuki, A., *Mater. Sci. Eng*. (1995), **C3**, 109–115.
12. Fornes, T. D., Yoon, P. J., Heskkula, H., Paul, D. R., *Polymer* (2001), **42**, 9929–9940.
13. Hasegawa, N., Okamoto, H., Kato, M., Usuki, A., Sato, N., *Polymer* (2003), **44**, 2933–2937.
14. Fornes, T. D., Paul, D. R., *Polymer* (2003), **44**, 4993–5013.
15. Liu, X., Wu, Q., *Macromol. Mater. Eng*. (2002), **287**, 180–186.
16. Chavarria, F., Paul, D. R., *Polymer* (2004), **45**, 8501–8515.
17. Han, B., Ji. G., Wu, S., Shen, J., *Eur. Polym. J*. (2003), **39**, 1641–1646.
18. Lew, C. Y., Murphy, W. R., McNally, G. M., Yanai, S., Abe, K., ANTEC 2003, 178–182.
19. Fornes, T. D., Paul, D. R., *Macromolecules* (2004), **37**, 7698–7709.
20. Chang, J-H., Kim, S. J., Joo, Y. L., Im, S., *Polymer* (2004), **45**, 919–926.
21. Pegoretti, A., Kolarik, J., Peroni, C., Migliaresi, C., *Polymer* (2004), **45**, 2751–2759.

22. Sanchez-Solis, A., Garcia-Rejon, A. Manero, O., *Macromol. Symp.* (2003), **192**, 281–292.
23. Chang, J.-H., An, Y. U., Ryu, S. C., Giannelis, E. P., *Polym. Bull.* (2003), **51**, 69–75.
24. Chisholm, B. J., Moore, R. B., Barber, G., Khouri, F., Hempstead, A., Larsen, M., Olson, E., Kelley, J., Balch, G., Caraher, J., *Macromolecules* (2002), **35**, 5508–5516.
25. Zhang, Q., Wang, K., Men, Y., Fu, Q., Chin. *J. Polym. Sci*. (2003), **21**, 359–367.
26. Oya, A., Kurokawa, Y., Yasuda, H., *J. Mat. Sci*. (2000), **35**, 1045–1050.
27. Wang, D., Wilkie, C., *Polym. Degrad. Stab.* (2003), **80**, 171–182.
28. Gopakumar, T. G., Lee, J. A., Kontopoulou, M., Parent, J. S., *Polymer* (2002), **41**, 5483–5491.
29. Wang, K. H., Koo, C. M., Chung, I. J., *J. Appl. Polym. Sci*. (2003), **89**, 2131–2136.
30. Wei, L., Tang, T., Huang, B., *J. Polym. Sci.*: Part A (2004), **42**, 941–949.
31. Hotta, S., Paul, D. R., *Polymer* (2004), **45**, 7639–7654.
32. Tjong, S. C., Meng, Y. Z., *J. Polym. Sci.*: Part B: *Polym. Phys*., (2003), **41** (13), 1476–1484.
33. Gilman, J. W., *Appl. Clay Sci*. (1999), **15**, 31–49.
34. Song, L., Hu, Y., Tang, Y., Zhang, R., Chen, Z., Fan, W., *Polym. Degrad. Stab.* (2005), **87**, 111–116.
35. Tidjani, A., 2005, *Polym. Degrad. Stab*. (2005), **87**, 43–49
36. Bourbigot, S., Vanderhart, D. L., Gilman, J. W., Bellayer, S., Stretz, H., Paul, D. R., *Polymer* (2004), **45**, 7627–7638.
37. Nielsen, L. E., *J. Mocromol. Sci*. (1967), **A1**, 929–942.
38. Osman, M., Atallah, A., *Macromol. Rapid Commun*. (2004), **25**, 1540–1544
39. Xu, R., Manias, E., Synder, A. J., Runt, J., *Macromolecules*, (2001), **34**, 337–339.
40. Ray, S. S., Yamada, K., Okamoto, M., Ogami, A. Ueda, K., *Chem. Mater*. (2002), **15**, 1456–1465.
41. Lan, T., Kaviratna, P. D., Pinnavaia, T. J., *Chem. Mater*. (1994), **6**, 573–575.
42. Chaiko, D. J., Leyva, A. A., *Chem. Mater*. (2005), **17**, 13–19.
43. Beall, G. W., Polymer–Clay Nanocomposites, edited by Pinnavaia, T. J. and Beall, G. W., John Wiley & Sons, Chichester, UK, (2001), 267–268.
44. Daniel, I. M., Miyagawa, H., Gdoutos, E. E., Luo, J. J., *Exp. Mech.* (2003), **43** (3), 348–354.
45. Uhl, F. M., Davuluri, S. P., Wong, S-C., Webster, D. C., *Polymer* (2004), **45**, 6175–6187.
46. Donnet, J. B., Compos. Sci. Technol. (2003), **63**, 1085.
47. Karger-Kocsis, J., Polym. Eng. Sci. (2004), **44**(6), 1083–1093.
48. Ajbani, M., Hsu, W., Halasa, A. F., Lee, G., Castner, E. S., US Pat. 6, 727, 311 (2004).
49. Parker, D. K.; Larson, B. K., Yang, X., US Pat. Appl. 2004/0054049 B1 (2004).
50. Sarashi, H., Jap. Pat. JP 2003327751 (2003).
51. Knudson, M. L., Powell, C., PCT Int. Pat. WO 02/070589 A2 (2002).
52. Heinrich, G., Herrmann, W., Kendziorra, N., Pietag, T., Recker, C., US Pat. 6, 818, 693 (2004).
53. Sadhu, S., Bhowmick, A. K., J. Polym. Sci.:Part B:Polym. Phys. (2004), **42**, 1573–1585.
54. Mousa, A., Karger-Kocsis, J., Macromol. Mater. Eng. (2001), **286**(4), 260–266.
55. Ganter, M., Gronski, W., Riechert, P., Mulhaupt, R., Rubber Chem. Technol. (2001), **74**(2), 221–235.
56. Sadhu, S., Bhowmick, A. K., Rubber Chem. Technol. (2003), **76**(4), 860–875.
57. Sadhu, S., Bhowmick, A. K., Adv. Eng. Mat. (2004), **6**(9), 738–742.
58. Sadhu, S., Bhowmick, A. K., J. Appl. Polym Sci. (2004), **92**(2), 698–709.
59. Bala, P., Samantaray, B. K., Srivastava, S. K., Nando, G. B., J. Appl. Polym. Sci. (2004), **92**, 3583–3592.
60. Wang, Y., Wu, Y., Ahang, H., Zhang, L., Wang, B., Wang, Z., *Macromol. Rapid Commu.* (2004), **25** (23), 1973–1978.
61. Malesa, M., Parasiewicz, W., Slusarski, L, Pysklo, L., Debek, C, *Materialy Konferencji, 7th* (2004), 108–111; Pub: Osrodek Badawczo-Rozwojowy Kauczukow I Tworzyw Winylowych, Oswiecim, Poland.
62. Ganter, M., Gronski, W., Semke, H., Zilg, T., Thomann, C., Muhlhaupt, R., Kautschuk Gummi Kunststoffe (2001), **54**(4), 166–171.
63. Zhang, L., Wang, Y., Wang, Y., Sui, Y., Yu, D., J. Appl. Polym. Sci. (2000), **78**(11), 1873–1878.
64. Maruyama, T., Ishikawa, K, Amino, N., Ikawa, M., US Pat. Appl. 2003/0191224 (2003).
65. Hagiwara, I., Kadota, K., Mashimo, S., Jap. Pat. JP 2003321551 (2003).
66. Gong, C., Dias, A. J., Tsou, A. H., Poole, B. J., Karp, K. R., PCT Int. Pat. WO 2004005387 A1 (2004).
67. Gong, C., Dias, A. J., Tsou, A. H., Poole, B. J., Karp, K. R., PCT Int. Pat. WO 2004005388 A1 (2004).
68. Ishida, K, Masaki, K., Jap. Pat. JP 2004224809. A2 (2004).
69. Yagi, N., Muraoka. K, Minagawa, Y., Nishioka, K., US Pat. Appl. 2004/0226643 (2004).
70. Maiti, M., Sadhu, S., Bhowmick, A. K., J. Polym. Sci., Part B: Polym. Phys. (2004), **42**(24), 4489–4502.
71. Mruyama, T., Ishikawa, K., Jap. Pat. JP 2004155912 A2 (2004).
72. Tsou, A. H., Dias, A. J., PCT Int. Pat. WO 02/100923 A2 (2002).
73. Larson, B. K., US Pat. 6598645 (2003).
74. Ajbani, M., Geiser, J. F., Parker, D. K., US Pat. Appl. 20030144401 A1 (2003).
75. Jeon, H. S., Rameshwaram, J. K., Kim, G., J. Polym. Sci., Part B: Polym. Phys. (2004), **42**(6), 1000–1009.
76. Yaakub, A., Kuen, C. P., Keane, N., Ross, M., US Pat. Appl. 20040147661 A1 (2004).
77. Kgawa, K, Maruyama, T., Ishikawa, K., Jap. Pat. JP 2004250473 A2 (2004).
78. Lopez-Manchado, M. A., Herrero, B., Arroyo, M., Polym. Int. (2004), **53**(11), 1766–1772.
79. Varghese, S., *Latex 2004, Two-Day Conference on Synthetic Emulsions, Natural Latex and Latex Based Products,* 3rd, (2004) 179–190, Rapra Technology Ltd., Shrewsbury, UK.
80. Varghese, S., Gatos, K.G., Apostolov, A. A., Karger-Kocsis, J., J. Appl. Polym. Sci. (2004), **92**(1), 543–551.
81. Varghese, S., Karger-Kocsis, J., Pannikottu, A., *Tech. Papers-American Chemical Society, Rubber Div. 164*th, (2003) 2148–2172, American Chemical Society, Rubber Div., Akron, Ohio.
82. Varghese, S., Karger-Kocsis, J., *Polymer* (2003), **44**(17), 4921–4927.
83. Varghese, S., Karger-Kocsis, J., J. Appl. Polym. Sci. (2004), **91**(2), 813–819.
84. Varghese, S., Karger-Kociss, J, Pannikottu, A., Rubber World (2004), **230**(1), 32–38.
85. Magaraphan, R., Thaijaroen, W., Lim-Ochakum, R., Rubber Chem. Technol. (2003), **76**(2), 406–418.
86. Vu, Y. T., Mark, J. E., Pham, L. H., Engelhardt, M., J. Appl. Polym. Sci. (2001), **82**(6), 1391–1403.
87. Joly, S., Garnaud, G., Ollitrault, R., Bokobza, L, Mark, J. E., Chem. Mater. (2002), **14**(10), 4202–4208.
88. Akelah, A., El-Deen, N. S., Hiltner, A., Baer, E., Moet, A., Mater. Lett. (1995), **22**, 97–102.
89. Okada, A., Fukumori, K., Usulki, A., Kojima, Y., Sato, N., Kurauchi, T., Kamigaito, O., Polym. Prepr. Am. Chem. Soc. Div. Polym. Chem. (1991), **32**, 540–541.
90. Kojima, Y., Fukumori, K., Usuki, A., Okada, A., Kurauchi, T., J. Mater. Sci. Lett. (1993), **12**, 889–890.
91. Pazur, R., Eur. Pat. Appl. EP 1475405 A1 (2004).
92. Kim, J., Oh, T., Lee, D., Polym. Int. (2004), **53**(4), 406–411.
93. Nah, C., Ryu, H.J., Kim, W. K., Chang, Y., Polym. Int. (2003), **52**(8), 1359–1364.
94. Gatos, K. G., Thomann, R., Karger-Kocsis, J., Polym. Int. (2004), **53**, 1191–1197.
95. Usuki, A., Tukigase, A., Kato, M, Polymer (2002), **43**(8), 2185–2189.
96. Zheng, H., Peng, A., Zhang, Y., Zhang, Y., Hecheng Xiangjiao Gongye (2002), **25**(5), 317.
97. Zheng, H., Zhang, Y., Zhang, Y., Peng, Z., Hecheng Xiangjiao Gongye (2003), **26**(2), 115.
98. Zheng, H., Peng, Z., Zhang, Y., Zhang, Y., Lin, H., Tanxingti (2002), **12**(6), 14–18.
99. Zheng, H., Zhang, Y., Peng, A., Zhang, Y., Lin, H., Hecheng Xiangjiao Gongye (2003), **26**(4), 226–229.

100. Zheng, H., Zhang, Y., Peng, A., Zhang, Y., Polym. Test. (2004), **23**(2), 217–223.
101. Zheng, H., Zhang, Y., Peng, Z., Zhang, Y., Li, P., Tanxingti (2003), **13**(4), 1–5.
102. Zheng, H., Zhang, Y., Peng, Z., Zhang, Y., J. Appl. Polym. Sci. (2004), **92**(1), 638–646.
103. Zheng, H., Zhang, Y., Peng, Z., Zhang, Y., Polym. Polym. Compos. (2004), **12**(3), 197–206.
104. Zheng, H., Zhang, Y., Peng, Z., Zhang, Y., Lin, H., Gaofenzi Xuebao (2004), (2), 160–164.
105. Zheng, H., Zhang, Y., Cheng, G., Li, P., Hecheng Xiangjiao Gongye (2004), **27**(3), 157–160.

CHAPTER 34

Polyhedral Oligomeric Silsesquioxane (POSS)

Guirong Pan

Department of Chemical and Materials Engineering, The University of Cincinnati, Cincinnati, OH 45221-0012

34.1 DEFINITION, HISTORY AND SYNTHESIS

The Polyhedral Oligomeric Silsesquioxanes (POSS) are an interesting class of three-dimensional inorganic/organic hybrids with the generic formula of $(RSiO_{3/2})_n$, as shown in Fig. 34.1 [1–4]. These molecules contain an inner inorganic framework covered by inert and/or reactive organic substituents. POSS molecules with well-defined shapes and sizes ranging from 1–3 nm have been described as the smallest version of colloidal silica. The R's can be inert organic groups used to enhance miscibility with polymeric host materials [5,6]. Making one or more of the R groups reactive permits bonding of the cages to polymers by copolymerization [7] or grafting [8] onto backbone chain. Incorporating such POSS cages into polymeric materials has already provided useful property enhancements, such as increased glass transition temperature, decomposition temperature, and mechanical strength. Because of the tailorability of POSS molecules, they can also be designed to probe the molecular basis of reinforcement, and to establish structure–property relationships that can then be exploited to optimize properties for particular applications. These POSS reagents have a number of desirable physical properties. For example, they are soluble in common organic solvents such as tetrahydrofuran (THF), toluene, chloroform, and hexane [9,10].

POSS was discovered in 1946 by Scott [11]. After 1990 the field developed rapidly due to the work of two groups: the Feher group at the University of California-Irvine and the Lichtenhan group at the Air Force Research Laboratory. The Feher group devised many methods for synthesizing and chemically modifying structurally well-defined Si/O frameworks [3,4,12–29]. The Lichtenhan group, on the other hand, pioneered the use of discrete POSS in polymer-related applications [7,9,30–32].

The synthesis of fully condensed POSS frameworks starts with the controlled hydrolysis and condensation of trifunctional organosilicon monomers (i.e., $RSiX_3$, R = c-C_6H_{11}, Cy or c-C_5H_9, *C*p) [13,16,33]. The functionalization of the POSS framework is then easily accomplished by corner capping of the POSS-trisilanols with silane coupling agents containing organic groups suitable for polymerization [1,13,16]. This methodology provides access to a family of cycloalkyl-substituted POSS monomers, each containing one polymerizable group, as shown in Fig. 34.2 [1]. In cases where the appropriate functionality is not directly available by the corner capping sequence, subsequent functional group transformation of the reactive group on a unique silicon atom is possible [1]. Multifunctional POSS derivatives can be made by the condensation of $R'Si(OEt)_3$, as described above, where R′ is a reactive group [2,34]. Another approach involves functionalizing POSS cages that have been formed [35–37].

The detailed methods of POSS synthesis have been reviewed by Voronkov *et al*. in 1982 [2] and Feher and co-workers in 2000 [28]. It is now possible to prepare range of useful Si/O frameworks from relatively inexpensive feedstocks. A variety of POSS reagents with one or more covalently bonded reactive functionalities has become commercially available from the Hybrid Plastics Company (http://www.hybridplastics.com).

34.2 NANOREINFORCED POSS-BASED POLYMER AND COPOLYMERS

Because of its chemical nature, POSS is easily incorporated into common plastics via copolymerization or blending, requiring little or no alteration to existing manufacturing processes. Incorporation of POSS reagents into

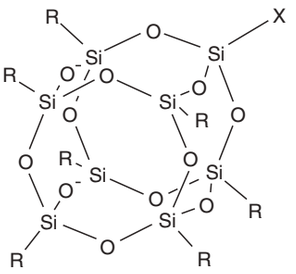

FIGURE 34.1. Schematic structure of POSS(R = c-C_6H_{11} (Cy), c-C_5H_9(Cp); X = reactive group).

linear thermoplastics or thermoset networks can be used to modify composition, local structure, and chain mobility. These modifications can ultimately affect the thermal, oxidative, and dimensional stability of many polymeric resins, resulting in improvements in properties, including increased glass-transition temperature, decomposition temperature and modulus, reduced flammability, and increased gas permeability. Depending on the number of POSS functional groups, different architectures of POSS/polymer composite can be obtained, as shown in Fig. 34.3.

A variety of POSS-containing polymer and copolymers have been synthesized based on radical [7], conventional [7,30], and atom-transfer [38], condensation [9,39] and ring-opening metathesis polymerization (ROMP) [40,41] techniques. Copolymers obtained in this manner with POSS units attached as dangling blocks to the polymer backbone include copolymers of polysiloxane [9,42], poly(methyl methacrylate) [30,32,38], poly(4-methylstyrene) [7,43–45], epoxy [39,46], polynorbornene [47–49], and polyurethane [50,51], *et al*. Monofunctional and difunctional POSS is commonly used in this case. The resulting materials represent a new category of polymers characterized by the presence of bulky POSS nanoparticles. There are some very useful review papers available on this subject [52,53].

Here, we will use POSS-styrene system as paradigm to explain the synthesis and properties of POSS-containing polymers and copolymers. Other systems are listed in Table 34.1, along with references. POSS-styrene polymers and copolymers with 4-methylstyrene have been extensively studied by Haddad *et al*. [7,44]. The reaction scheme is shown in Fig. 34.4.

The glass transition temperature T_g of poly(*co*-POSS-4-methylstyrene) varies linearly with mole percent POSS in the copolymer, from 116 °C for pure poly(4-methylstyrene) to approximately 400 °C for pure polyPOSS-substituted styrene. The decomposition temperature of the styryl backbone dramatically increases, presumably because the large pendant POSS groups reduce chain mobility. POSS modification also effects dynamical mechanical properties [43]. By varying the R groups on the POSS cages, the DMTA spectra show an increase in tan δ with R = Cy>Cp (Cy:cyclohexyl, Cp:cyclopentyl) and a plasticization effect when R = *i*-Bu. This result supports the conclusion that R groups on the POSS cages result in significant changes of bulk mechanical properties [48]. Coughlin *et al*. are studying hemi-telechelic POSS-polystyrene and are investigating

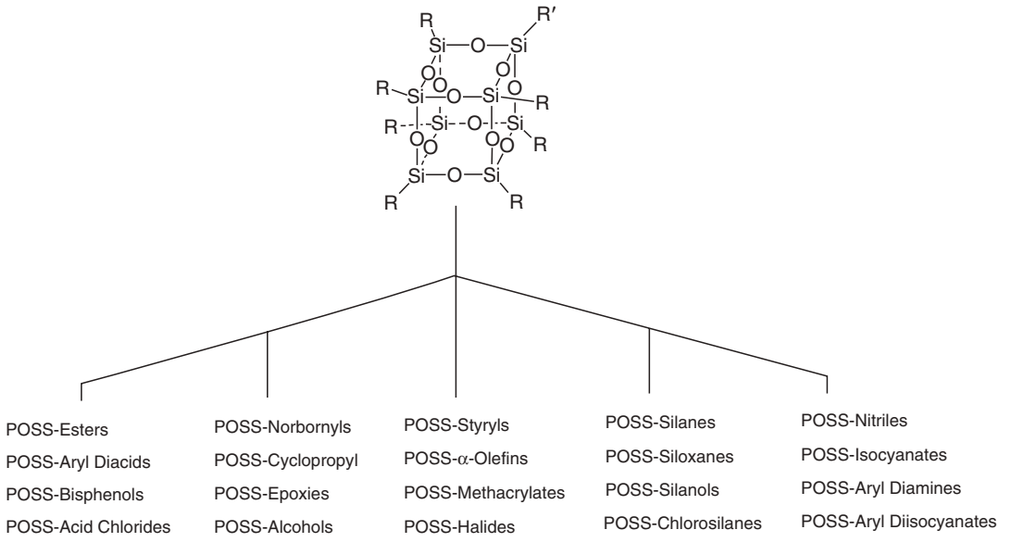

FIGURE 34.2. Some of the functionalities that can be prepared from POSS–trisilanol precursors [1]. (Applied Organometallic Chemistry, 12, Schwab, J. J. and Lichtenhan, J. D., "Polyhedral Oligomeric Silsesquioxane (POSS)-based Polymers," pp. 707–713, Copyright (1998), John Wiley and Sons Ltd., New York. Reproduced with permission.)

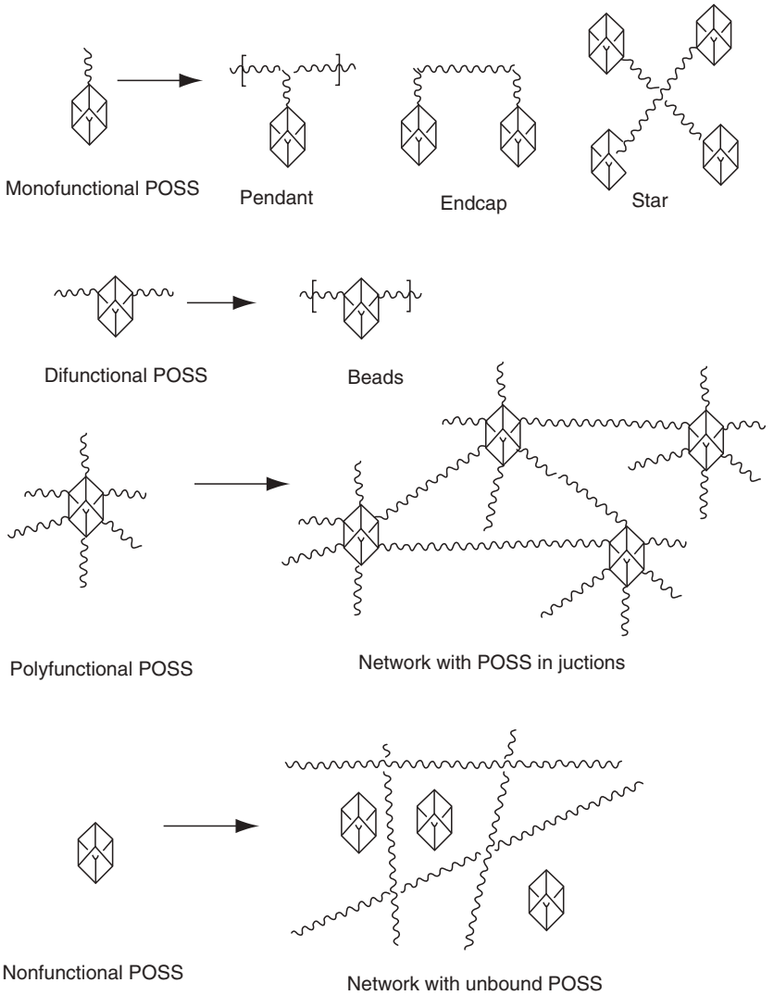

FIGURE 34.3. POSS/polymer architectures.

whether POSS moieties within a polymer matrix organize into lamellae, cylinders, or other hierarchical structures. Their visualization matches their TEM data, displaying the ''raft-like'' or lamellae structure of POSS within the polymer matrix (Fig. 34.5) [54,55].

Incorporation of multifunctional POSS into polymer systems has been investigated with different polymers [6,62–66]. In these cases, single-phase polymer networks with POSS molecularly dispersed are often formed. POSS acts as a polyhedral cross-link. But no definite effect of POSS on network properties has been established. Both a decrease [64,65] and no change in T_g [6] were reported. The rubbery modulus increases due to a high crosslink density, and thermal stability increases with POSS content.

A more convenient method of incorporating POSS into organic polymers is physical blending. Since each POSS molecule has a Si_8O_{12} core covered with alterable organic side groups, it is believed that better dispersion may result from increased interaction of compatible side groups and polymer [67–69]. Blanski *et al*. [69] studied the dispersion of POSS in polystyrene. They found that by altering the organic side groups to more compatible phenethyl groups, POSS molecules can be fully dispersed into high molecular weight polystyrene. The surface hardness of the styrenyl POSS/polystyrene film increased 30%. Molecularly dispersed POSS behave as a weak cross-linker in polymer melts and accelerate the crystallization rate of the host polymer [70]. Matejka *et al*. [64,65] studied the effect of POSS with various topological locations in a network on its structure and properties. These authors incorporated monofunctional, multifunctional, and nonfunctional POSS into epoxy networks and observe that that POSS pendant on a network chain showed a strong tendency toward aggregation and crystallization. The crystalline domains thus act as physical cross-links, leading to very strong reinforcement. The mechanical

TABLE 34.1. *POSS-contained polymer and copolymer systems.*

System	Components	Architecture	Property	References
POSS–Polystyrene	Styryl-POSS-*co*-4-methylstyrene	Pendants	T_g increases; T_d increases	[7,43–45]
POSS–Polynorbornene	Norbornyl-POSS; norbornene	Pendants	T_g increase; no effect on T_d; shape memory behavior	[47–49]
POSS–Epoxy	Epoxy–POSS; diglycidyl ether of bisphenol A	Pendants	T_g increases and broadens; the shape of viscoelastic spectrum not affected; slowing down of the chain relaxation in the glassy state	[39,46]
Siloxane–POSS	Hybrid–POSS; vinyl substituted dichlorosilanes	Beads, pendants	Thermal stability increased	[9,42]
POSS–Polyethelene	Vinyl–POSS; ethylene	Pendants	T_m decreases; thermostability increases; oxidative resistance increases	[57]
	Norbornyl–POSS	Pendants	Oxidative resistance increases; lamellae structure of POSS in polymer	[40,54,55,58,59]
Polyurethane–POSS	Hydrido–POSS; polytetramethylene glycol(PTMG); 4,4′-methyle nebis(phenylisocyanate) (MDI)	Pendants	Formation of POSS crystals	[50,51]
Acrylate–POSS	Methacrylate–POSS; *n*-butyl acrylate	Pendants, star, endcap	Effect of R on solubility; thermostability increase; T_d, T_g increase; oxygen permeability increases	[30,32,38]
Polyimide–POSS	Diamine–POSS with pyromellitic dianhydride	Pendants	Self assembly; lower dielectric constant	[60,61]

properties are affected mainly by POSS–POSS interactions while the POSS-network chain interactions are of minor importance.

34.3 POSS AS BUILDING BLOCKS FOR CONTROLLED STRUCTURED MATERIALS

Since a POSS molecule has both defined structure and specific functional groups, it provides the possibility of preparing nanocomposites with controlled structures. There has been considerable effort using POSS cages as building blocks to make controlled structure materials.

Laine *et al*. [35–37,71–78] have developed several routes to link POSS cubes by chemical reactions that lead to organic tethers (spacers) between the cages or cubes with the objective of determining whether well-defined composite nanostructure and periodically placed organic/inorganic components will offer novel and predictable properties. To date, macromonomers based on cubes functionalized with methacrylate [35,36], epoxide [76,77], alcohol [79], and aliphatic amine [78] groups have been generated and nanocomposites have been made from these octafunctional POSS molecules. Figure 34.6 illustrates the formation of nanocomposites from octafunctional POSS. Studies based on these materials suggested that nanocomposite with essentially completely defined inorganic and organic phase can be produced.

A large amount of work involves cages with vinyl and Si–H groups as links by hydrosilylation reactions [36,72,74,80–83]. Catalytic hydrosilylation is a well-studied method of forming Si–C linkages by adding Si–H moieties to C–C multiple bonds. The commonly used monomers are ${}^{R}T_8$ cages (R:H or Vinyl; T: $RSiO_{3/2}$) or ${}^{R}M_8Q_8$ (R:H or Vinyl; M: $R_3SiO_{1/2}$; Q: $SiO_{4/2}$). The chemical structures of those cages are shown in Fig. 34.7. Network structure as shown in Fig. 34.8 is formed from reactions combing these cages.

The Hoebbel and Hasegawa [80,82] research groups find that more than 60% and more commonly above 80% of the functionality Si–H and Si–Vinyl were consumed to make

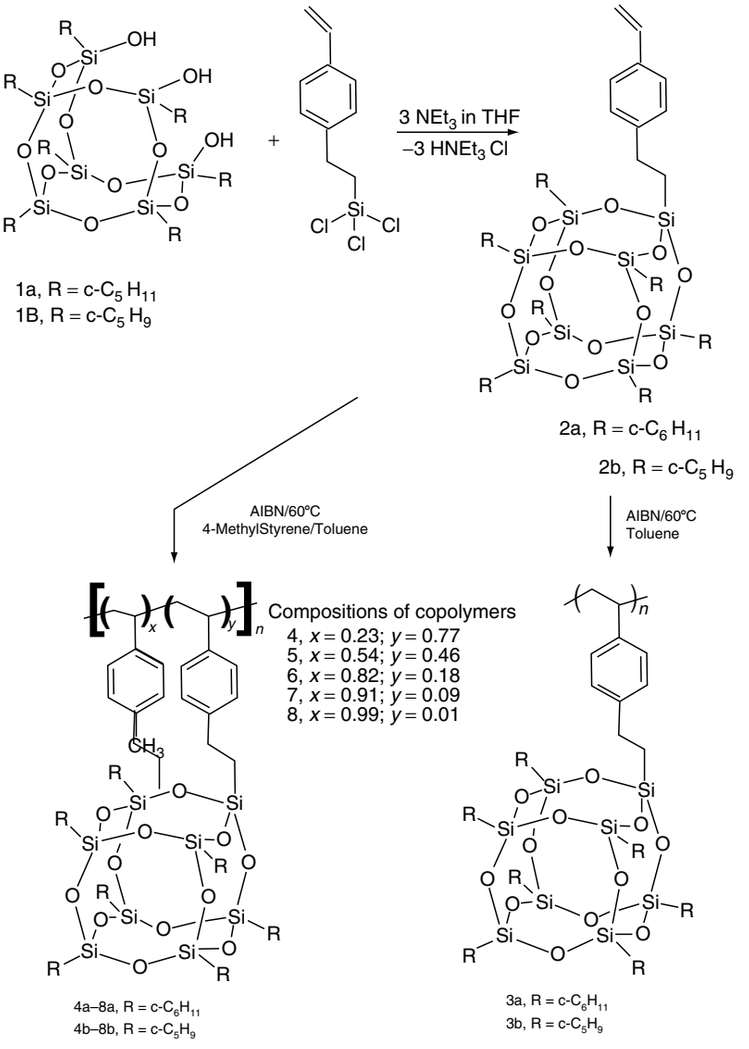

FIGURE 34.4. Styryl-POSS macromonomer synthesis and its polymerization and copolymerization [7]. Reprinted with permission from Macromolecules, 29(22), 7302–7304. Copyright (1996) American Chemical Society.

silethylene linkages by the hydrosilylation. With this type of conversion efficiency it is not surprising that none of the materials are soluble, since nearly all of the precursors are octafunctional.

Laine *et al*. [36,72,74] published a study that described both the synthesis and characterization of gels made by combining the ^{H}M8Q8, ^{V}iM8Q8, ^{H}T8, and^{Vi}T8. All of the materials were found to be a combination of micro- and mesoporous with specific surface areas between 380 and 530 m^2/g. Intercube pore size and size distribution are dominated by tether length and defects (missing cubes).

Some approaches have also been developed to make soluble controlled structure materials with T8 and M8Q8 cages by changing the stoichiometry of the reaction and limiting the extent of crosslinking [81,84,85].

Epoxy-based POSS nanocomposites have also been studied thoroughly by various groups [6,76–78,86]. In these systems, either POSS with an octaglycidyl group was connected by diaminodiphenyl methane (DDM), or POSS with an octaamino group is connected by diglycidyl ether of bisphenol A(DGEBA). The nanoarchitecture was tailored by changing the ratio between amine group and the epoxy group. Results suggest that the structure and rigidity of the organic tethers connecting the cubes strongly mediated thermal stabilities, glass transition temperatures, and consequently global mechanical properties. Aromatic tether structure and short lengths increased the char yields and decomposition temperature.

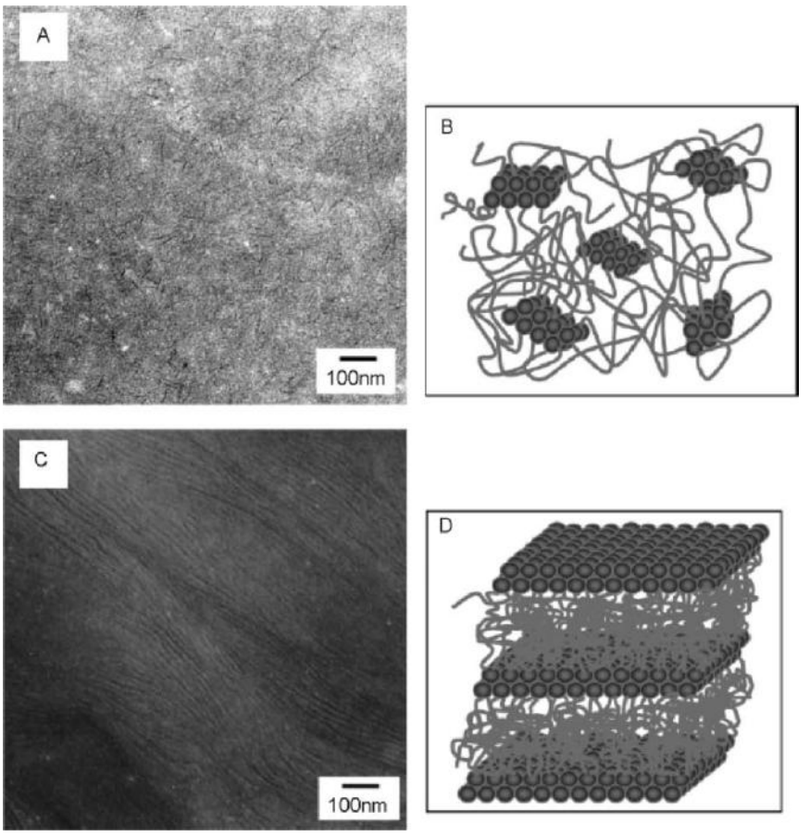

FIGURE 34.5. (A) TEM of PBD-POSS-1(10% POSS). The copolymers of low POSS concentration aggregate into short randomly oriented lamellae with lateral dimensions of approximately 50 nm. (B) Schematic drawing of PBD-POSS assembly at low POSS concentration. (C) TEM of PBD-POSS-4 (40% POSS). The copolymers of high POSS concentration form continuous lamellar morphologies with lateral lengths on the order of microns. (D) Schematic drawing of PBD-POSS assembly at high POSS concentration [56]. Reprinted with permission from Macromolecules 2004, 37(23), 8606–8611. Copyright 2004, American Chemical Society.

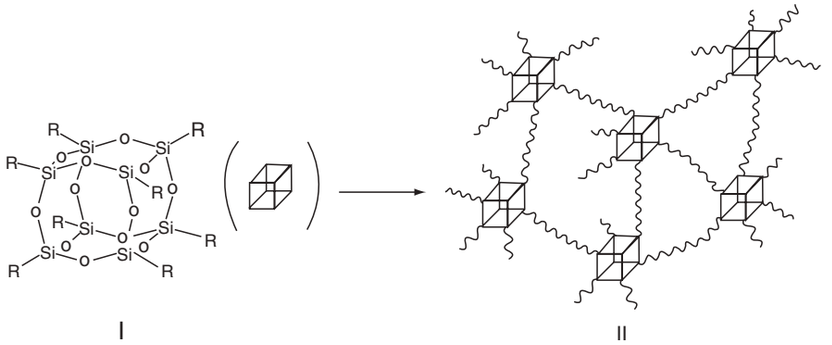

FIGURE 34.6. Nanocomposite formation (II) from octafunctional POSS (I) Via cross-linking of functional groups R [78]. Reprinted with permission from Macromolecules 2004, 37(1): 99–109. Copyright 2004, American Chemical Society.

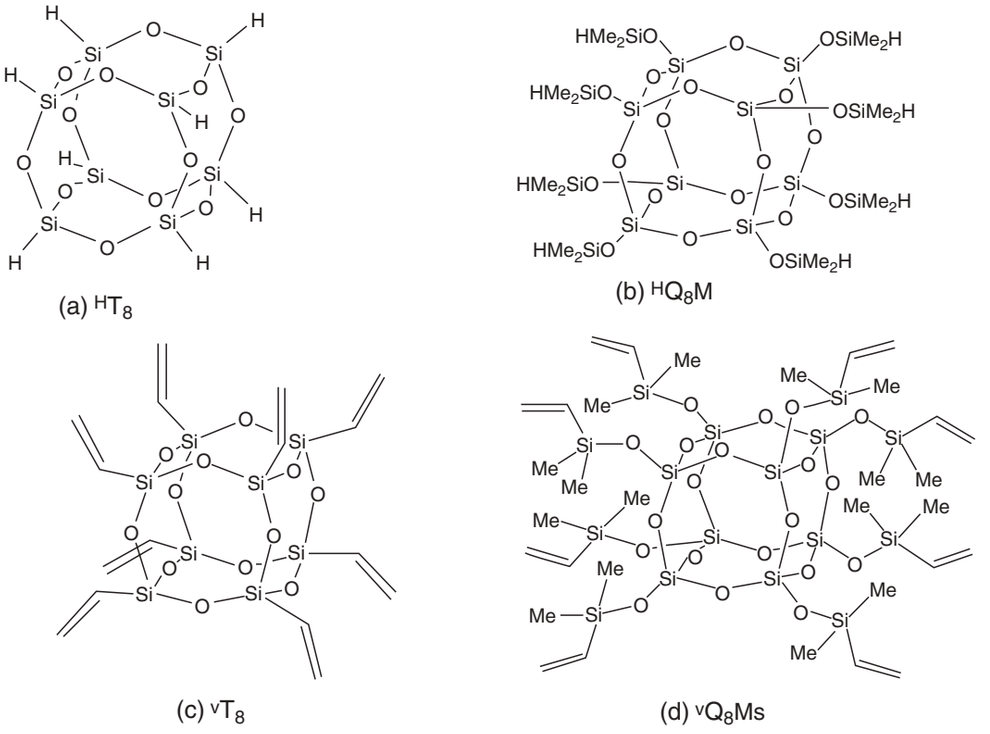

FIGURE 34.7. Hydrido (a–b) and vinyl cubes (c–d).

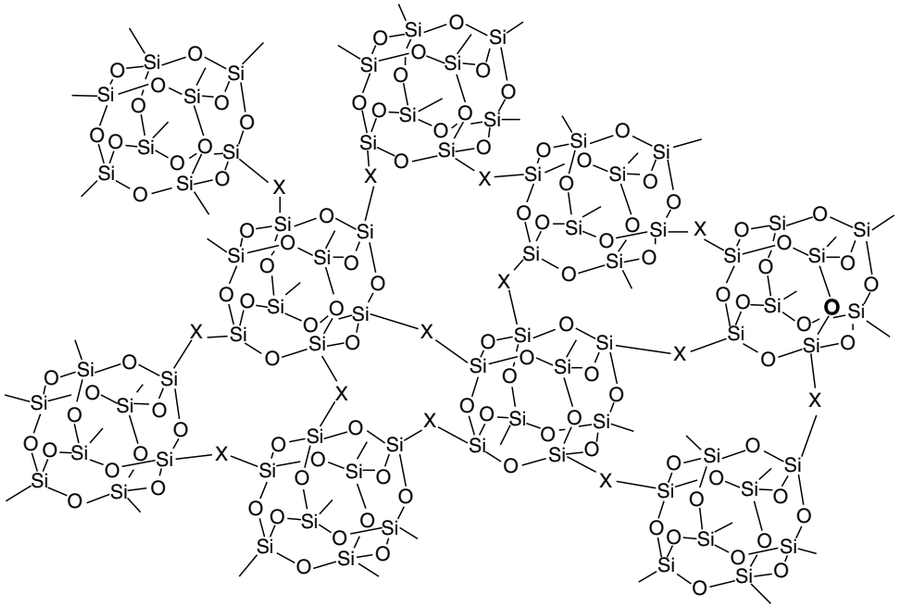

FIGURE 34.8. Network structures formed by combining hydrido (a–b) and vinyl cubes (c–d) [72]. Reprinted with permission from Journal of the American Chemical Society 1998, 120(33): 8380–8391. Copyright 1998, American Chemical Society.

REFERENCES

1. Schwab, J. J.; Lichtenhan, J. D. *Appl. Organometal. Chem.* **1998**, *12*, 707.
2. Voronkov, M. G.; Lavrent'ev, V. *Top. Curr. Chem.* **1982**, *102*, 199–236.
3. Feher, F. J.; Budzichowski, T. A. *J. Organometal. Chem.* **1989**, *379*, 33–40.
4. Feher, F. J.; Budzichowski, T. A. *J. Organometal. Chem.* **1989**, *373*, 153–163.
5. Lichtenhan, J. D.; Noel, C. J.; Bolf, A. G.; Ruth, P. N. In *Mat. Res. Soc. Symp. Proc.*, **1996**; *435*, 3.
6. Li, G. Z.; Wang, L. C.; Toghiani, H.; Daulton, T. L.; Koyama, K.; Pittman, C. U. *Macromolecules* **2001**, *34*, 8686–8693.
7. Haddad, T. S.; Lichtenhan, J. D. *Macromolecules* **1996**, *29*, 7302.
8. Chun, S. B.; Mather, P. T. In *Mat. Res. Soc. Symp. Proc.*, 2001; Vol. 661, p KK10.18.11.
9. Lichtenhan, J. D.; Vu, N. Q.; Carter, J. A. *Macromolecules* **1993**, *26*, 2141.
10. Schwab, J. J.; Reinerth Sr., W. A.; Lichtenhan, J. D. *Polymer Preprints* **2001**, *42*, 48.
11. Scott, D. W. *J. Am. Chem. Soc.* **1946**, *68*, 356.
12. Feher, F. J.; Budzichowski, T. A.; Weller, K. J. *J. Am. Chem. Soc.* **1989**, *111*, 7288–7289.
13. Feher, F. J.; Newman, D. A.; Walzer, J. F. *J. Am. Chem. Soc.* **1989**, *111*, 1741–1748.
14. Feher, F. J.; Blanski, R. L. *J. Chem. Soc.-Chem. Commun.* **1990**, 1614–1616.
15. Feher, F. J.; Newman, D. A. *J. Am. Chem. Soc.* **1990**, *112*, 1931–1936.
16. Feher, F. J.; Budzichowski, T. A.; Blanski, R. L.; Weller, K. J. *Organometallics* **1991**, *10*, 2526.
17. Feher, F. J.; Phillips, S. H.; Ziller, J. W. *J. Am. Chem. Soc.* **1997**, *119*, 3397–3398.
18. Feher, F. J.; Wyndham, K. D.; Knauer, D. J. *Chem. Commun.* **1998**, 2393–2394.
19. Feher, F. J.; Soulivong, D.; Nguyen, F.; Ziller, J. W. *Angew. Chem.-Int. Edit.* **1998**, *37*, 2663–2666.
20. Feher, F. J.; Wyndham, K. D.; Scialdone, M. A.; Hamuro, Y. *Chem. Commun.* **1998**, 1469–1470.
21. Feher, F. J.; Soulivong, D.; Nguyen, F. *Chem. Commun.* **1998**, 1279–1280.
22. Feher, F. J.; Wyndham, K. D. *Chem. Commun.* **1998**, 323–324.
23. Feher, F. J.; Soulivong, D.; Eklund, A. G. *Chem. Commun.* **1998**, 399–400.
24. Feher, F. J.; Terroba, R.; Ziller, J. W. *Chem. Commun.* **1999**, 2309–2310.
25. Feher, F. J.; Terroba, R.; Ziller, J. W. *Chem. Commun.* **1999**, 2153–2154.
26. Feher, F. J.; Nguyen, F.; Soulivong, D.; Ziller, J. W. *Chem. Commun.* **1999**, 1705–1706.
27. Feher, F. J.; Wyndham, K. D.; Soulivong, D.; Nguyen, F. *J. Chem. Soc.-Dalton Trans.* **1999**, 1491–1497.
28. Feher, F. J.; Terroba, R.; Jin, R.; Wyndham, K. D.; Lucke, S. *Polym. Mater. Sci. Eng.* **2000**, *82*, 301.
29. Bakhtiar, R.; Feher, F. J. *Rapid Commun. Mass Spectrom.* **1999**, *13*, 687–694.
30. Lichtenhan, J. D.; Otonari, Y. A.; Carr, M. J. *Macromolecules* **1995**, *28*, 8435.
31. Lichtenhan, J. D. *Comments Inorg. Chem.* **1995**, *17*, 115.
32. Lichtenhan, J. D.; Noel, C. J.; Bolf, A. G.; Ruth, P. N. *Mat. Res. Soc. Symp. Proc.* **1996**, *435*, 3.
33. Brown, J. F.; Vogt, L. H. *J. Am. Chem. Soc.* **1965**, *87*, 4313.
34. Frye, C. L.; Collins, W. T. *J. Am. Chem. Soc.* **1970**, *92*, 5586.
35. Sellinger, A.; Laine, R. M. *Chem. Mater.* **1996**, *8*, 1592.
36. Sellinger, A.; Laine, R. M. *Macromolecules* **1996**, *29*, 2327.
37. Zhang, C.; Laine, R. M. *J. Am. Chem. Soc.* **2000**, *122*, 6979.
38. Pyun, J.; Matyjaszewski, K. *Macromolecules* **2000**, *33*, 217.
39. Lee, A.; Lichtenhan, J. D. *Macromolecules* **1998**, *31*, 4970–4974.
40. Zheng, L.; Farris, R. J.; Coughlin, E. B. *J. Polym. Sci. Pt. B-Polym. Phys.* **2001**, *39*, 2920.
41. Haddad, T. S.; Mather, P. T.; Jeon, H. G.; Chun, S. B.; Phillips, S. H. In *Mat. Res. Soc. Symp. Proc.*, 2000; Vol. 628.
42. Manze, R. A.; Jones, P. F.; Chaffee, K. P.; Lichtenhan, J. D. *Chem. Mater.* **1996**, *8*, 1250.
43. Haddad, T. S.; Viers, B. D.; Phillips, S. H. *J Inorg Organomet Polym* **2002**, *11*, 155.
44. Romo-Uribe, A.; Mather, P. T.; Haddad, T. S.; Lichtenhan, J. D. *J. Polym. Sci. Pt. B-Polym. Phys.* **1998**, *36*, 1857–1872.
45. Xu, H. Y.; Kuo, S. W.; Lee, J. S.; Chang, F. C. *Macromolecules* **2002**, *35*, 8788–8793.
46. Lee, A.; Lichtenhan, J. D.; Reinerth Sr., W. A. *Polym. Mater. Sci. Eng.* **2000**, *82*, 235.
47. Mather, P. T.; Jeon, H. G.; Romo-Uribe, A.; Haddad, T. S.; Lichtenhan, J. D. *Macromolecules* **1999**, *32*, 1194–1203.
48. Jeon, H. G.; Mather, P. T.; Haddad, T. S. *Polym. Inter.* **2000**, *49*, 453.
49. Bharadwaj, B. K.; Berry, R. J.; Farmer, B. L. *Polymer* **2000**, *41*, 7209.
50. Fu, B. X.; Hsiao, B. S.; White, H. *Polym. Inter.* **2000**, *49*, 437.
51. Fu, B. X.; Hsiao, B.; Pagola, S.; Stephens, P. *Polymer* **2001**, *42*, 599.
52. Li, G. Z.; Wang, L. C.; Ni, H.; Pittman Jr., C. U. *J. Inorg. Organometal. Polym.* **2001**, *11*, 123.
53. Phillips, S. H.; Haddad, T. S.; Tomczak, S. J. *Curr. Opin. Solid State Mater. Sci.* **2004**, *8*, 21.
54. Zheng, L.; Hong, S.; Cardoen, G.; Burgaz, E.; Gido, S. P.; Coughlin, E. B. *Macromolecules* **2004**, *37*, 8606–8611.
55. Zheng, L.; Waddon, A. J.; Farris, R. J.; Coughlin, E. B. *Macromolecules* **2002**, *35*, 2375–2379.
56. Zhang, H. J.; Kulkarni, S.; Wunder, S. *Abstr. Pap. Am. Chem. Soc.* **2004**, *228*, 281.
57. Tsuchida, A.; Bolln, C.; Sernetz, F. G.; Frey, H. *Macromolecules* **1997**, *30*, 2818.
58. Zheng, L.; Farris, R. J.; Coughlin, E. B. *Polym. Prepr.* **2000**, *41*, 1929.
59. Zheng, L.; Farris, R. J.; Coughlin, E. B. *Macromolecules* **2001**, *34*, 8034–8039.
60. Leu, C. M.; Chang, Y. T.; Wei, K. H. *Chem. Mater.* **2003**, *15*, 3721.
61. Leu, C. M.; Chang, Y. T.; Wei, K. H. *Macromolecules* **2003**, *36*, 9122–9127.
62. Li, G. Z.; Wang, L.; Toghiani, H.; Pittman Jr., C. U. *Polymer* **2002**, *43*, 4167.
63. Li, G. Z.; Cho, H.; Wang, L. C.; Toghiani, H.; Pittman, C. U. *J. Polym. Sci. Pol. Chem.* **2005**, *43*, 355–372.
64. Matejka, L.; Strachota, A.; Plestil, J.; Whelan, P.; Steinhart, M.; Slouf, M. *Macromolecules* **2004**, *37*, 9449–9456.
65. Strachota, A.; Kroutilova, I.; Kovarova, J.; Matejka, L. *Macromolecules* **2004**, *37*, 9457–9464.
66. Lee, Y. J.; Huang, J. M.; Kuo, S. W.; Lu, J. S.; Chang, F. C. *Polymer* **2005**, *46*, 173–181.
67. Kim, K. M.; Adachi, K.; Chujo, Y. *Polymer* **2002**, *43*, 1171.
68. Yoon, K. H.; Polk, M. B.; Park, J. H.; Min, B. G.; Schiraldi, D. A. *Polym. Inter.* **2005**, *54*, 47.
69. Blanski, R. L.; Phillips, S. H.; Chaffee, K.; Lichtenhan, J. D. In *Mat. Res. Soc. Sym. Proc.*, 2000; Vol. 628.
70. Fu, B. X.; Yang, L.; Somani, R. H.; Zong, S. X.; Hsiao, B. *J. Polym. Sci. Pt. B-Polym. Phys.* **2001**, *39*, 2727.
71. Zhang, C.; Laine, R. M. *J. Organomet. Chem.* **1996**, *521*, 199.
72. Zhang, C. X.; Babonneau, F.; Bonhomme, C.; Laine, R. M. *J. Am. Chem. Soc.* **1998**, *120*, 8380.
73. Tamaki, R.; Tanaka, Y.; Asuncion, M. Z.; Choi, J. W.; Laine, R. M. *J. Am. Chem. Soc.* **2001**, *123*, 12416–12417.
74. Laine, R. M.; Zhang, C.; Sellinger, A.; Viculis, L. *Appl. Organomet. Chem.* **1998**, *12*, 715.
75. Laine, R. M.; Choi, J.; Lee, I. *Adv. Mater.* **2001**, *13*, 800.
76. Choi, J.; Harcup, J.; Yee, A. F.; Zhu, Q.; Laine, R. M. *J. Am. Chem. Soc.* **2001**, *123*, 11420–11430.
77. Choi, J.; Yee, A. F.; Laine, R. M. *Macromolecules* **2003**, *36*, 5666–5682.
78. Choi, J.; Kim, S. G.; Laine, R. M. *Macromolecules* **2004**, *37*, 99–109.
79. Costa, R. O. R.; Vasconcelos, W. L.; Tamaki, R.; Laine, R. M. *Macromolecules* **2001**, *34*, 5398–5407.
80. Hoebbel, D.; Endres, K.; Reinert, T.; Pitsch, I. *J. Non-Cryst. Solids* **1994**, *176*, 179.
81. Auner, N.; Bats, J. W.; Katsoulis, D. E.; Suto, M. *Chem. Mater.* **2000**, *12*, 3402.
82. Hasegawa, I. *J. Sol-Gel Sci. Technol.* **1995**, *5*, 93–100.
83. Pan, G.; Mark, J. E.; Schaefer, D. W. *J. Polym. Sci. Pt. B-Polym. Phys.* **2002**, *41*, 3314.
84. Hoebbel, D.; Pitsch, I.; Heldemann, D.; Jancke, H. *Z. Anorg. Allg. Chem.* **1990**, *583*, 133.
85. Tebeneva, N. G.; Rebrov, E. A.; Muzafarov, A. M. *Polym. Prepr.* **1998**, *39*, 503.
86. Kim, G. M.; Qin, H.; Fang, X.; Sun, F. C.; Mather, P. T. *J. Polym. Sci. Pt. B-Polym. Phys.* **2003**, *41*, 3299–3313.

CHAPTER 35

Carbon Nanotube Polymer Composites: Recent Developments in Mechanical Properties

M.C. Weisenberger, R. Andrews, and T. Rantell

University of Kentucky Center for Applied Energy Research
2540 Research Park Dr. Lexington, KY 40511

35.1 INTRODUCTION

Over the last decade, carbon nanotubes [1] have been the subject of intense investigation in both fundamental and applied sciences [2]. With single crystal graphite and fullerenes as a starting point, great strides have been made in understanding the properties of these materials at the nanoscale:the nature by which they transport electrons [3,4], and heat [5,6], and how they respond to applied forces and fields [7,8]. Results of these computations and experiments have demonstrated their truly remarkable properties, and have placed carbon nanotubes (CNTs) at the forefront of nanotechnology development. It is their unique and desirable properties at the nanoscale that serve as the basis and motivation for endeavors to create new advanced materials based on carbon nanotubes. For example, the use of CNTs as nanoscale reinforcing fibers in polymer matrices is an idea that is profoundly motivated by their mechanical properties. In concept, this is the nanoscale analogue to conventional carbon fiber composites, offering exciting possibilities for materials design given that CNTs have been measured to be more than 15 times stronger than the best available carbon fiber, have elastic moduli of single crystal graphite, and yet remain extremely flexible with aspect ratios of greater than 1,000 (Table 35.1). However, realizing the unique mechanical properties of CNTs in macroscale composites has proven to be a more complex issue. It is a multifaceted problem in which a number of competing factors must be considered, including: CNT diameter, length, crystalline defects, orientation, concentration, and dispersion; interfacial adhesion; composite processing method; matrix material; as well as their inter-relationships, in order to begin to optimize the final composite properties. The purpose of this paper is to discuss these issues within the scope of the recent literature, and to highlight advances and understanding in this emerging field.

35.1.1 Carbon Nanotubes:Properties and Types

The structure and properties of CNTs can be approached in many ways. Chemists and physicists may prefer to think of CNTs as linearly extended fullerenes. In fact, the most ideal carbon nanotube, a perfect, isolated single wall carbon nanotube (SWNT) is exactly that. But CNTs, in general, are not so simple, and tend to form in a range of morphologies from bundles of SWNTs [9], mats of multiwall nanotubes (MWNT) [10], to nonfullerene morphologies approaching vapor grown carbon fibers [11]. To those interested in composites, CNTs are essentially ultrafine carbon fibers capable of elastically withstanding unprecedented stresses and strains. Concurrently, they present new challenges in translating these properties to a practical length scale in a composite. Many technical hurdles exist; not the least of which is

TABLE 35.1. *On-axis mechanical properties of CNTs and graphitic materials.*

Material type	Young's modulus (GPa)		Break stress (GPa)		Strain to failure (%)	
SWNT	1,250 $\pm$ 400	[18]	$\sim$100	[20]	10–15	[21]
	$\sim$1,000	[19]				
SWNT Bundle	1,250	[22]	$>45 \pm 7$	[22]	1–6	[22]
MWNT	1,800 $\pm$ 900	[23]	11–63	[13]	5–12	[13,24,25]
	270–950	[13]	150	[24]		
	910	[24]				
Carbon Nanofiber	$\sim$100	[26]	2.7	[27]	$\sim$ 1	[27]
	400	[27]				
Graphite Whisker	700–1,000	[28]	19.6	[28]	$\sim$2	[28]
High strength Carbon fiber	220–580	[29,30]	4.3–6.4	[29,30]	1.5–2.2	[29,30]
High modulus Carbon fiber	520–827	[11]	1.9–3.3	[11]	0.3–0.6	[11]

The high strain to failure of nanotubes allows for very high break strengths.
Selected experimental mechanical testing methods reported for CNTs:[23] In situ TEM imaging of thermal vibrations of cantilevered MWNTs, [18] In situ TEM imaging of thermal vibrations of cantilevered SWNTs, [24] In situ TEM tensile testing of MWNTs, [13] In situ SEM tensile testing of MWNTs.

separating or dispersing the CNTs such that they can be individually loaded in a composite. SWNTs tend to form into bundles or ropes due to van der Waals forces, making them difficult to individually disperse into matrices [12]. Multiwall carbon nanotubes, or concentrically nested SWNTs, can be easier to disperse, but tensile stress transfer to inner walls is thought to be inefficient due to weak intershell bonding [13,14]. However it has been shown that some stress can transfer to the inner shells via fusion, or bond reforming, of a fractured outer shell to an adjacent inner shell [15].

CNTs are synthesized by various methods including electric arc discharge [1], laser ablation [16], and chemical vapor deposition [1,7,10,17], each yielding nanotubes with various characteristics such as diameter, defect density, entanglement and length. Just as using different carbon fibers yields different composite properties, using different CNT types results in varying CNT composite properties. Recent experiments have investigated the effect of the CNT type in composites for mechanical reinforcement (the results of which will be highlighted in the properties section). Typical mechanical properties of various CNT types are listed in Table 35.1. It must be acknowledged that CNTs, like oriented graphite, are very anisotropic materials. Their large strengths and elastic moduli relate only to the direction parallel to the axis of the nanotube.

35.2 NANOTUBE-POLYMER COMPOSITE PROCESSING

35.2.1 Dispersing Carbon Nanotubes

The most commonly studied matrices for CNT-reinforced composites are polymers. Fabricating composites of CNTs in polymer matrices almost invariably involves a dispersion process in which the nanotubes are incorporated into the polymer. Although the small size of CNTs precludes some conventional fiber composite fabrication techniques such as filament winding or hand lay-up, it does enable techniques such as composite fiber spinning, (discussed later). The goal of dispersion is to homogeneously distribute individual CNTs throughout the matrix material such that the applied load can be uniformly distributed among the nanotube population. For thermoplastic polymers, melt mixing the CNTs via high shear fields is often utilized [31]. In practice, this can be achieved by passing a nanotube/polymer blend though an extruder fitted with mixing screws in order to arrive at the desired level of dispersion [32]. Other methods of melt mixing invariably utilize the shearing forces generated during the mixing of molten polymer to disperse the nanotubes [33]. Nanotubes, however, are known to increase the viscosity of fluids due to their large aspect ratio, high stiffness, and ability to form entangled networks [34–36]. Therefore, achieving high loadings of CNTs in polymer melts is difficult even at high temperatures ($\sim$10–20 wt.% is a common upper limit to uniform dispersion attained with melt mixing [37]). Another method, sonication, uses high frequency sound waves to induce cavitation in low viscosity solvents in the presence of CNT agglomerates. The energy released upon cavity collapse breaks up CNT agglomerates dispersing the nanotubes into the solvent [38,39]. Matrix polymer can then be dissolved into the CNT/solvent dispersion rendering a solvent-processable dispersion. Alternatively, matrix polymer can be introduced by in situ polymerization of miscible liquid monomer in the presence of the CNT dispersion [15]. The viscosity of the final dispersion can be adjusted with both heat and solvent addition/evaporation making higher concentrations of CNTs in the final, solidified polymer possible. Loadings of up to 60 wt.% CNTs have been reported in PVA composite fibers using this method of dispersion [40]. In either case, it has

been shown that the quality of CNT dispersions has a profound impact on the resulting composite properties. Initial property enhancements at low loadings, ~1 wt.% CNTs, often do not continue or are reduced at higher loadings [32,41]. Agglomerates of CNTs can act as a stress concentrating points and reduce the mechanical properties of the matrix [42]. However, once dispersed in polymer melts or solutions, dispersions of CNTs can then be processed into composite parts via conventional polymer processing techniques such as injection molding, film casting, or fiber spinning, from which test specimens can be fashioned, and the composite properties determined.

35.2.2 Factors Influencing CNT Dispersion

The homogeneity of CNT dispersions, either via shear mixing or sonication, is not only a critical factor affecting composite properties, but an important parameter in the quality and stability of composite processing as well. The three most influential factors affecting the quality of the dispersion are the amount of dispersive energy input into system, the degree of entanglement of the bulk CNT material, and the interaction of the CNT surface with the continuous phase. The first factor was investigated by Andrews *et al*. [10] regarding melt mixing MWNTs into various thermoplastics. Dispersion quality was assessed via optical microscopy of relatively large areas of the composites (100 × 100 μm), and the observed homogeneity was correlated to the amount of mechanical energy input by the high shear melt mixer. A minimum value of approximately 1,000 J/ml, was found to effectively disperse a range of MWNT concentrations up to 5.0 vol.%. Higher loadings required higher amounts of mixing energy. A corresponding reduction in MWNT length was found to accompany shear mixing, but CNT aspect ratios of 200+ remained. CNT shortening is an unavoidable result in all dispersive processes, including sonication, given the forces that the CNTs are subjected to, and may in fact serve to enhance the dispersability of the CNTs themselves as their ability to entangle is dependent on their aspect ratio. However, excessive reduction of the CNT length may negatively impact its reinforcing capacity. Kearns and Shambaugh [43] report an optimum sonication time of 2 hr for a nanotube loading of 1wt.%; a compromise between achieving sufficient dispersion and minimizing CNT damage. The use of ultrasonic induced cavitation to disperse CNTs into low viscosity fluids is somewhat dependent on the frequency used. Ultrasonic instruments using a frequency of ~20 kHz have been shown to disperse MWNT mats very well [38]. Higher frequency sonication instruments, such as ultrasonic cleaning baths at ~40 kHz, have also shown to be effective [43]. The efficiency of ultrasonic dispersion depends upon an inverse relationship between frequency and particle size. Thus, it may be advantageous to employ a program of progressively increasing frequency to sequentially reduce bulk agglomerates of CNTs into individual tubes [44]. The degree of CNT entanglement prior to dispersing has been shown to severely limit the homogeneity of dispersion [45]. ''Bird's nest'', or highly entangled CNTs produced from floating catalyst CVD processes or bundles of SWNTs are very difficult to individually disperse by shear or sonication alone. MWNTs grown on substrates in aligned arrays with virtually no entanglement have been shown to be more easily dispersed [45].

35.2.3 Surface Treatment of CNTs

The ability to produce a homogeneous dispersion of CNTs in a polymer matrix or solution can be enhanced by chemically altering the nanotube surface to augment the solvent–nanotube or polymer–nanotube interaction. This may be accomplished by a variety of methods including the use of surfactants, chemical functionalization, and in situ polymerization. Treatment of SWNTs with a nonionic surfactant was shown to enhance the dispersion and resulting mechanical properties of epoxy-matrix composites relative to untreated SWNTs [46]. Other examples of CNT dispersions benefiting from the use of surfactants have been reported [40,47,48]. Oxidative treatments of CNTs have been widely reported as a means to improve dispersion [34,35], including the use of strong oxidizing agents such as nitric/sulfuric acids, $KMnO_4$ [49] and H_2O_2 [50], and by subjection to oxygen plasmas [51]. One of the most popular methods is the sonication of CNTs in a 3:1 solution of sulfuric:nitric acid [34,35,52,53]. Refluxing the acid/CNTs is also employed. The resulting oxygenated groups on the CNT surface, including hydroxyl and carboxylic groups counteract the van der Waals attractive forces between CNTs and enhance interaction with the matrix phase thus improving dispersion. Kim *et al*. [52] report that sonicating MWNTs for 8 hrs in 3:1 sulfuric:nitric acid, resulted in the addition of carboxylic groups at a concentration of approximately 1.3×10^{-3} mol/g. Tethering and wrapping of polymer chains to CNT surfaces by polymerizing monomers in situ with the CNTs has been shown to be effective in improving both dispersion quality and composite properties [15,49,54]. Eitan *et al*. [54] demonstrated evidence of epoxide functionalization of oxidized MWNTs, which can be used to covalently crosslink CNTs into epoxy matrices. Similarly, Valentini *et al*. [55] reported amine functionalized CNTs for crosslinking epoxy matrices. In another report, uniform dispersion and significantly enhanced moduli were observed using PMMA-grafted MWNTs in PMMA matrix composites [15]. Other methods of chemically functionalizing CNTs include the use of diazonium salts [56], radical species [57], photochemistry [58] and others [59,60] to derivitize a wide variety of organo-CNTs.

35.2.4 Processing CNT-Polymer Composite Films

CNT-polymer composites are commonly produced in the form of films for mechanical property analysis. The thicknesses of these films range from a few millimeters to

electron-transparent TEM samples. Once a suitable level of CNT dispersion is achieved in the matrix, films are easily processed by pressing CNT-polymer melts, casting CNT-polymer solutions/thermosets into molds and drying/curing, or spin casting from CNT-polymer solutions. Test specimens of precise dimensions can be cut or machined from these composite films for mechanical testing. Pressing CNT-thermoplastic films is well described in the literature and is a simple method of producing composite specimens [10,42,50,61–63]. Polymer containing dispersed CNTs is typically crushed or pelletized, placed between heated platens, and pressed at a pressure in the range of 10–30 MPa [61,62] such that molten CNT composite polymer flows outward constrained to some predetermined thickness by shims or a mold [10]. Upon solidification, test specimens are then cut from the film. For CNT-polymer solutions and CNT-thermoset matrices, composite films are typically processed utilizing a casting technique. Well-dispersed CNT-polymer fluids are transferred to molds and heated to evaporate the solvent or cure the thermoset [15,20,64–67]. In a similar method, dispersed CNTs in PVA-water solutions are allowed to settle followed by decanting the PVA solution containing well dispersed CNTs. These suspensions are then deposited dropwise onto substrates, and the solvent is evaporated. This process is repeated to build up to the desired thickness of film [12,68–71]. Very thin CNT-polymer composite films (thickness = 200 nm) [72] can be produced by means of spin casting in which suspensions of CNTs in low viscosity polymer solutions are deposited dropwise to the center of a rotating substrate. Spinning for 20–30 sec at 3,000 rpm has been reported to produce electron-transparent films [73]. The centrifugal forces induce radial flow of the drop resulting in thin films with some preferred orientation of the embedded CNTs along the direction of flow. Fabrication of continuous CNT-polymer composite films has been demonstrated by extrusion of CNT composite thermoplastic through a slit die followed by take-up onto a chilled roller [74]. Other techniques include resin infiltration into dry CNT preforms [25,75,76], polymer intercalation of aligned MWNT mats [77,78] and SWNT ''buckypaper'' [79], and complete in situ polymerization of thermoplastic matrices [49,80].

The orientation of the embedded CNTs relative to the loading conditions, as in all fiber composites, has an effect on the properties that are measured. The process of shear-mixing or sonication results in random orientation of the CNTs throughout the polymer matrix, which can be preserved throughout processing given the absence of strong uni-directional shear or elongational flow. For most CNT-polymer film processing, the CNT orientations are randomly arranged relative to the principal axes of the film. Exceptions occur when any degree of stretching or drawing of the film is implemented, which forces embedded CNTs into alignment with the direction of flow [50,64,67,74,81]. This is observed for CNT-polymer melt extrusions through slit dies [74], and injection moldings of carbon nanofiber-polymer composites [76]. Achieving the highest degrees of CNT alignment within a polymer matrix is achieved by spinning dispersions of CNTs in polymer fluids into fibers.

35.2.5 Processing CNT-Polymer Composite Fibers

Homogeneous dispersions of CNTs in viscoelastic polymer fluids can be spun into composite fibers. Melt spun, solution spun, and electro-spun CNT composite fibers have been produced. These methods have been shown to be very effective in aligning the CNTs with the direction of flow, i.e., the fiber axis. This class of oriented CNT composites is of particular interest since direct axial loading of the CNTs is possible. It is in this fashion that high-strength, lightweight CNT composites are envisioned. However, the ability to sustain stable CNT-polymer composite fiber spinning is largely dependent on the homogeneity of the dispersion. CNT agglomerates can disrupt the flow as fiber attenuation is applied leading to breakage during processing, or in the case of large agglomerates, complete blockage of the small diameter orifices through which the fibers are extruded. Achieving large attenuations or draw ratios, which serve to orient both the CNTs and the polymer chains with the fiber axis resulting in increased fiber properties, is primarily dependent on the quality of the initial CNT dispersion.

Melt spinning CNT/thermoplastic composite fibers has been investigated for numerous polymers including poly (methyl methacrylate) [32,33,50], polypropylene [43,82,83], polystyrene [10], polyamide [45], and engineering thermoplastics such as polyimide [31], and poly(ether ether ketone) [26]. In a typical process, the CNTs are dispersed in the molten polymer using a high shear mixer followed by extrusion through a cylindrical die orifice or spinneret. Before the composite fiber cools and solidifies, attenuation is accomplished by continuous collection on a rotating drum. Mechanical testing of the fibers can then be performed using a variety of techniques including single filament tensile testing. CNT composite fibers spun from polymer solutions involve a coagulation process to solidify the fibers in which the solvent is replaced by a second miscible solvent, often water, which acts as a nonsolvent to the polymer causing it to solidify. Complete removal of residual solvent in the fiber is done via a drying process. Reported solution spun CNT composite fibers include poly(vinly alcohol) [40,84,85], poly(acrylonitrile) [38,86] (an important precursor to commercially produced carbon fiber), and poly(*p*-phenylene benzobisoxazole) [87] (PBO). Electro-spun fibers are produced by generating a high voltage between a negatively charged spinning solution and a conductive collector. The advantage of this technique is the production of ultrafine fibers (<100 nm) as very fine jets of polymer are accelerated toward the collector, but unlike melt or solution spinning, the production of continuous filament is difficult. Fibers have been electrospun from dispersions of CNTs in poly(vinly alcohol) [88], poly (acrylonitrile) [89], and poly(vinylidene fluoride) [90].

35.2.6 CNT Orientation in Films and Fibers

The orientation of anisotropic reinforcing fibers relative to the loading conditions has a major impact on the measured properties. Composites containing fibers oriented in the direction of loading will display the highest properties. Tensor transformations can be used to predict the efficiency of the reinforcement for composites with fibers oriented at any arbitrary angle to the load [91]. An off-axis misalignment of 10° reduces the modulus of graphite from 1,020 GPa to 120 GPa [32]. The degree of CNT alignment within a composite structure is largely determined by the processing method used to fabricate the material. Pressed films demonstrate random alignment while drawn fibers and films exhibit some preferred alignment. Measurement of the degree of orientation of embedded CNTs with a principal axis of the composite is therefore an important consideration. The use of azimuthal or phi scanning x-ray diffraction and polarized micro-Raman spectroscopy have been shown to be effective in quantifying the CNT alignment within composite structures. The x-ray technique, analyzes the two symmetrically diffracted arcs produced by the CNTs about the azimuthal angle (Fig. 35.1). The integrated intensity of these diffracted arcs as a function of the azimuthal angle results in peaks. The breadth of a peak at half its maximum (FWHM) is inversely proportional to the degree of CNT alignment. That is, very sharp peaks correspond to a very high degree of CNT alignment. Whereas, random alignment, results in no discernable peaks as the diffracted x-rays intersect the detector in a ring of uniform intensity. This process is described by Lucas and Vigolo [92] regarding the degree of orientation of SWNTs in solution spun PVA composite fibers. It was also utilized by Kumar [86,87] to evaluate CNT alignment in PAN and PBO composite fibers, by Shaffer [26,45] in polyamide and PEEK composite fibers and by Zhou [93] in drawn poly(hydroxyaminoether) films.

Similarly, determination of CNT orientation by polarized micro-Raman spectroscopy was demonstrated by analysis of the intensity of the Raman peaks at 202 and 1,590 cm^{-1} as a function of the angle between the focused beam and the composite fiber axis [31,50]. Higher intensity peaks along the fiber axis correspond to a large degree of CNT alignment. Another technique of micro-Raman spectroscopy utilizes the principle of peak shifting as a function of the induced strain in the CNTs. Not only is this technique useful for elucidating the amount of stress transfer to the CNTs themselves [66,94,95], but the rate at which with peak shifts with respect to the applied strain correlates to the orientation of the CNTs to the load and thus their alignment [96]. Other techniques include light scattering microscopy to probe induced alignment of CNTs in shear fields [97,98]. In practice, limitations to perfecting uniaxial orientation of CNTs, even in highly drawn fiber matrices have been observed, and attributed to intrinsic ''waviness'' or graphitic misalignment within the CNT structures themselves [45].

35.3 NANOTUBE-POLYMER COMPOSITE PROPERTIES

35.3.1 CNT-Reinforced Polymers: Experimental Results

It is ultimately the properties demonstrated in the CNT composites that will determine the material's utility, while its proliferation will be determined by cost. The promise of a new class of high-performance composite materials, given the magnitude of CNT mechanical properties, remains. Selected experimental results can be used to highlight CNT-polymer composite properties, their relation to processing (dispersion, concentration, orientation), CNT type, and various matrix polymers.

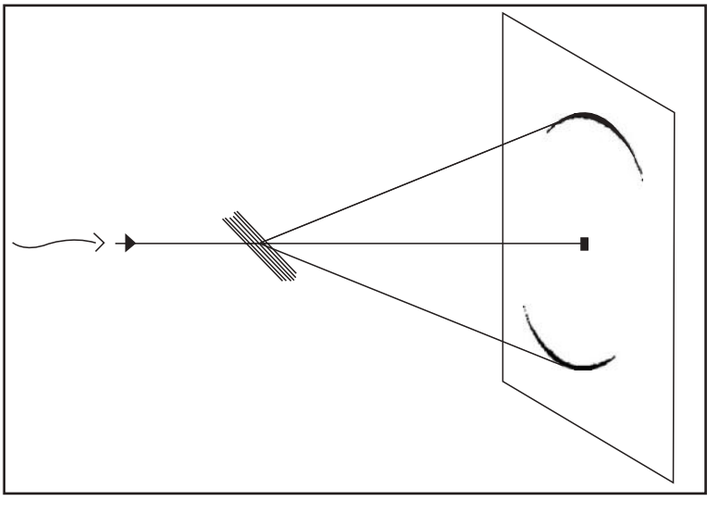

FIGURE 35.1. 2-D x-ray diffraction of aligned MWNTs.

35.3.2 Increases in Toughness

The work of Qian *et al*. [99] using in situ TEM straining of MWNT/polystyrene films demonstrated that nanotubes function to bridge crack opening by spanning the separating surfaces in the crack wake. Wagner *et al*. [100] report similar findings. At crack separations of ~800 nm, the MWNTs were observed to pull out of the crack face, especially those aligned perpendicular to the separating faces, indicative of nanotube/matrix interfacial failure [99]. Tube fracture was observed to occur for defective tubes, such as at catalyst inclusions, or for tubes aligned parallel to the crack. The mechanism of CNT crack bridging has been credited with enhancing the toughness of polymers primarily by increasing the strain to break of the material. This effect was shown by Lozano *et al*. [61]. Increases of 220% in elongation translated into a 290% increase in toughness, which was attributed to the embedded carbon nanofibers (CNFs) in HDPE arresting crack propagation from coalesced voids. Gorga and Cohen [33] report a similar result augmented by the presence of aligned MWNTs in PMMA fiber matrices. Increases in the toughness of 800% were reported in composite fiber containing 1 and 3 wt.% MWNTs, and attributed to the nanotubes bridging crazes and subsequent cracks in the matrix under uniaxial tension. They further elaborate that CNT pull-out provides energy dissipation by frictional slipping thus benefiting material toughness. Therefore aligned CNT systems, in agreement with Qian's observed pull-out of orthogonally oriented tubes, may provide for significantly enhanced toughnesses. In another report by Ruan *et al*. [66], the mechanism of toughness increase for aligned MWNTs in drawn UHMWPE films was attributed to an enhancement of chain mobility in the presence of the MWNTs. Indeed many other researchers have reported significant increases in toughness of aligned CNT composites [31,38,40,87,101], which may prove useful especially for enhancing the performance of impact resistant materials.

35.3.3 Increases in Elastic Modulus and Break Strength

Enhancement of the modulus of a polymer reflects the transfer of stress from the polymer matrix to the high-modulus embedded CNTs. Thus strong interfacial adhesion between the polymer and CNT is preferred for stiffening the composite. Enhancement in break strength also reflects strong interaction between the CNT and polymer, but strength is also profoundly affected by the presence of defects such as voids or agglomerate inclusions, which serve to initiate failure by stress concentration. Therefore, processing can have a major impact on the measured strength. Namely, poor CNT dispersion can be detrimental to strength, which may explain why increases in CNT composite strength are less often observed compared with increases in modulus. Typical increases in the elastic modulus and break strength of CNT-polymer composites are outlined in Table 35.2 for various polymer matrices. Other reported effects in CNT-polymer composites include increases in the matrix polymer glass transition temperature, and increases

TABLE 35.2. *Mechanical property enhancements of nano-composite materials.*

Matrix	Fiber	Loading wt.%	Form	E_c GPa	σ_c MPa	T_c J/g	Ref.
PEEK	CNFs	10	Fibers	+20%	+20%		[26]
PVA	SWNT	60	Fibers		1,800*	600*	[101]
	MWNT	< 1	Films	+370%	+430%	+170%	[69]
Cl-PP	MWNT	< 1	Films	+310%	+390%	+440%	[69]
PAN	SWNT	10	Fibers	+100%			[86]
	MWNT	3	Fibers	+36%	+31%	+80%	[38]
PP	SWNT	1	Fibers		+45%		[82]
	SWNT	1		+55%	+40%		[43]
	CNFs	5		+50%	+100%		[83]
	CNFs	15	Films	+90%			[42]
PBO	SWNT	10	Fibers		+50%		[87]
PMMA	MWNT	30	Films	+140%			[62]
		20		+1,100%			[15]
PMEA	MWNT	1	Films	+200%			[47]
PS	MWNT	5	Films	+10%			[74]
			Drawn Films	+49%			
		20	Films	+50%	+0%		[10]
UHMWPE	MWNT	1	Drawn Films	+25%	+48%	+150%	[66]
HDPE	CNFs	8	Films	+60%			[61]
PC	SWNT	0.06	Films	+29%			[104]

E_c = composite modulus; σ_c = composite break strength; T_c = composite toughness
* These are absolute values not increases compared to neat polymer.

in composite fatigue life. Kumar *et al*. [86] report that the T_g of PAN composite fibers increased from 103 °C to 143 °C with the inclusion of 10 wt.% SWNT into the matrix. Increases in T_g are often attributed to a restriction of interchain mobility by the presence of the CNTs [32]. Marrs *et al*. [102] reported significant increases in the fatigue life of MWNT/PMMA-based bone cement composites, an important consideration for the lifetime of joint replacements. Others compared the fatigue properties of aligned SWNT ropes in epoxy to carbon fiber/epoxy composite, and concluded the SWNT/epoxy allowed for much higher fatigue stresses while maintaining similar fatigue life as the carbon fiber/epoxy [103].

35.3.4 Factors Influencing CNT-Polymer Composite Mechanical Properties

Shaffer *et al*. [105] investigated the effect of the type of CNT reinforcement in polyamide fibers and concluded that the use of aligned substrate-grown MWNTs resulted in the best composite properties. An identical result was reached by Gorga *et al*. [33] for MWNTs in PMMA. The fact that the bulk MWNTs were not initially entangled provided for better dispersion. Other researchers reported that longer nanotubes, resulting in higher aspect ratios, improved composite properties [33,99]. A recurring inter-relation between processing and properties is dispersion. Many researchers have reported diminishing properties of their CNT composites as the concentration exceeds 1 wt.% [82], and others exceeding 5–10 wt.% [32,33]. The continuous increase in composite properties predicted by theory does not occur, and is likely due to a lack of homogeneous dispersion. The orientation of the CNTs relative to the load has also been shown to have an effect on the composite properties. Thostenson *et al*. [74] found a 50% improvement in the tensile modulus of aligned MWNT/PS composites compared to a 10% improvement for randomly oriented MWNT/PS composites. Others have shown that the strength of the interfacial bonding and other interfacial effects in CNT-polymer composites has a profound effect on the composite properties [69] (discussed later).

35.3.5 CNT-Reinforced Polymers: Theoretical Modeling of Experimental Results

The use of theoretical models to predict the properties of CNT composites has been useful in dealing with certain aspects of these nanocomposites. In particular, Brinson *et al*. [41,106] addressed the issue of CNT waviness or curvature and its effects on composite properties. TEM observations of embedded CNTs have shown that they are not rectilinear but have some degree of waviness [99], which may be due to their crystalline defects and elastic flexibility. A reduction in the modulus of wavy CNTs can be expected due to CNT anisotropy. Finite element analysis was used to calculate what the effective reinforcing modulus would be of a wavy CNT of wavelength, λ, relative to a straight CNT [41]. A second micromechanical model used this result to predict the properties of a bulk CNT composite considering a distribution of embedded CNT waviness, or amplitude of curvature to wavelength ratio. The results predicted significant reductions in effective modulus for wavy CNTs. For a waviness of 0.1, or a CNT that is 90% straight, a 40–50% reduction in modulus was predicted. This method, applied to experimental results of MWNT/PS composite films, provided a more accurate model than predicted with straight CNTs. This work and others [107,108] underscore the importance of CNT waviness to composite properties.

The issue of CNT diameter and its effects on composite properties has been modeled by Thostenson *et al*. [109]. For embedded MWNTs, the dilemma lies in the degree to which tensile stress is transferred from the outermost wall to the inner walls of the MWNT. They considered that although the MWNT acts as a solid fiber in a composite, tensile stress is only carried by the outermost tube wall due to weak interwall Van der Waals bonding. Therefore, accurately modeling the load bearing capacity of the MWNT must be calculated by averaging the stress in the outer wall over the complete cross-section of the MWNT. Thus larger diameter MWNTs containing many concentric shells, will have significantly lower effective reinforcing moduli. Experimental verification of this idea was tested by fabricating drawn films of MWNTs in polystyrene to align the MWNTs. Electron microscopy was used to measure the distribution of MWNT diameters, which was modeled in the composite by parallel partitioning of the MWNT volume fraction into discrete diameter ranges. A Halpin-Tsai based model was applied in which the effective moduli of the embedded MWNT diameter distribution was used to yield an overall composite modulus. The embedded lengths of the MWNTs were also considered, but did not play an important role considering large aspect ratios were maintained. The model was compared to experimental data for composite films with MWNT concentrations of 5 and 10 wt.% with very good agreement. Larger diameter MWNTs occupy a larger volume fraction of the composite, display lower effective moduli, and thus make a significantly reduced contribution to the composite properties.

Perhaps the most important issue in CNT-polymer composites is a good understanding of interfacial bonding between the embedded CNTs and the polymer matrix. Frankland *et al*. [110] used molecular dynamics simulations to study the interfacial forces involved with pulling a SWNT through a polyethylene matrix. Assuming a noncovalently bound interface, it was calculated that a force of 0.1 nN was required to initiate SWNT slippage. Higher forces resulted in a periodically increasing velocity of the SWNT relative to the matrix, indicative of atomistic interactions of the SWNT surface with the crystalline PE matrix. Averaging the increase in velocity and relating it to the frictional interfacial shearing stress led to an effective viscosity of 0.2 mPa s, about that of pentane at room temperature. Another molecular mechanics simulation of the pull-out of CNTs from a

polystyrene matrix resulted in quite high interfacial shear strength of 160 MPa for a noncovalently bound system, and concluded that the high strength was likely to be due to the intimate contact between the small diameter CNT and the PS chains [111]. The bonding between the CNTs and the polymer matrix is an important consideration, and could be considerably enhanced in covalently bonded systems through the use of functionalized CNTs to promote high interfacial shear strength. Sinnot *et al.* [112,113] have shown via molecular dynamics simulations that functionalization of CNT surfaces does not significantly decrease the mechanical properties of CNTs. Experimental determination of the interfacial shear strength of CNT-polymer composites has recently been demonstrated [114].

35.4 NANOTUBE–POLYMER INTERFACIAL EFFECTS

35.4.1 CNT–Polymer Interfacial Adhesion

Obviously the strength of the interfacial bonding between the CNTs and the polymer matrix will have a major impact upon their ability to reinforce the composite. Wagner *et al.* [114] studied this issue by conducting experiments in which a MWNT, attached to an AFM tip, was embedded in a polymer and pulled out. The force versus pull-out length was recorded for a poly(ethylene-butene) matrix resulting in an interfacial shear strength of 47 MPa. This value is consistent with other measurements where estimates of $\sim$50 MPa for various nanotube types were recorded [12].

35.4.2 Rule of Mixtures Inapplicability

The region of highest importance in any composite material is the interface between the reinforcing filler and the matrix material. Under an applied load, strains develop throughout the material, which can be envisioned, for the case of tension, as an overall increase in the displacement between two parallel planes of material orthogonal to the load. In the interphase region between the bulk matrix and the embedded, discontinuous fibers, these strains translate into shear stresses as the fibers are typically less compliant than the matrix, thus straining less. This scenario is applicable to CNTs in a polymer matrix. These interfacial shear stresses build along the length of the fibers acting in opposite directions from the fiber midpoint, and serve to transfer the applied load from the surrounding matrix to the embedded fibers. If the interface is strong and the volume fraction of fibers is sufficiently high, then the matrix is prevented from complying with the load and the tensile stress increases. The matrix is reinforced by the fibers. If the interface remains strong, and/or the embedded fibers are very long, the accumulated shear stresses can translate into tensile fracture of the embedded fibers representing the most efficient reinforcement possible for that composite system. This view of traditional composite micromechanics, underlies the widely accepted rule-of-mixtures approach to modeling fiber reinforced composite materials. It states that the modulus of the composite is a linear combination of the moduli of the materials from which it is composed, and weights each modulus with the volume fraction of that component. Its basis lies in continuity of parallel strain between the fibers and matrix provided a linearly elastic response of the composite occurs for small strains.

$$E_c = E_f V_f + E_m(1 - V_f),$$

where E_f is the fiber tensile modulus, E_m, the matrix modulus, and V_f is the volume fraction of fiber. This conclusion is based on some important assumptions. Some of which render it inapplicable to most CNT-polymer composites.

(1) ***The CNT-Matrix Interface is Strong (Continuity of Strain)***

This means that no slippage of the CNTs through the matrix occurs. In polymer–CNT composites, significant nanotube pull-out has been verified even at low strain indicating interfacial failure [38].

(2) ***The CNTs are all Aligned Parallel with the Direction of Load***

The fiber modulus, E_f, refers to the modulus of the fiber when loaded in pure tension. Embedded CNTs typically show some measure of curvature [115], waviness [41], and misalignment with any given material direction even for highly drawn matrices [50,64,86,105].

(3) ***The Length of CNTs is Sufficient for Maximum Interfacial Shear–Stress Build-up***

This implies that the average length of the embedded CNTs is long relative to the load transfer length (length required for complete interfacial shear–stress build-up). Embedded lengths of CNTs post sonication were measured to be primarily in the 1–10 μm range [116]. Pull-out of these CNTs was confirmed via TEM straining [38].

(4) ***The CNTs are Homogeneously Dispersed and Homogeneously Loaded***

This implies that each individual CNT is loaded homogeneously by stress transfer from the surrounding matrix. (No CNT–CNT interactions). Achieving homogeneous dispersion of CNTs, especially at concentrations $>$ 10 wt.% has been shown to be difficult [101].

(5) ***The Composite Modulus is Linearly Related to the Moduli of its Component Phases***

This implies that the modulus of each phase is independent and unchanged by the presence of the others. Nanotubes have been shown to induce polymer matrix crystallization near their surfaces thus altering the matrix [70]. In other words, the interfacial matrix potentially has different properties from the neat matrix.

More refined models of macroscale composite stiffness have been developed (such as the Halpin-Tsai equations [91]) that take into account some of the assumptions made above, e.g., fiber length, orientation, and inefficiencies in

stress transfer. These assumptions are often dealt with by giving the fiber an ''effective modulus'', which is lower than its ideal modulus, and have been applied to CNT–polymer composites with some success. Another example is the Krenchel rule of mixtures [105].

$$E_C = \eta_0 \eta_1 V_f E_f + (1 - V_f) E_m, \tag{35.1}$$

where η_0 is the CNT orientation factor [91]; η_1 is the CNT length factor [117]; and $E_f \eta_0 \eta_1$ is the CNT effective modulus. However, numerous publications citing observations of CNT-induced crystallinity in various semicrystalline polymer matrices have prompted the need to reconsider the validity of assumption (5) above [12,26,69,70,82,105].

35.4.3 CNT-Induced Polymer Crystallization

Within the past few years, many investigators have observed an increase in the degree of crystallinity or crystallite size of semicrystalline polymer–CNT composites due to the addition of CNTs. Differential scanning calorimetry (DSC) melting endotherms have been frequently employed to demonstrate this effect (Table 35.3). Recently, Coleman *et al.* [69] investigated this induced crystallization effect, and related it to the mechanical properties of the composite. The results highlight a fundamental difference between CNT–polymer composites and carbon fiber–polymer composites: with CNT composites the interface dominates all other effects due to the vast surface area/volume ratio that CNTs have relative to carbon fibers (Fig. 35.2).

Linear increases in crystallinity with increasing MWNT concentration of a MWNT/poly(vinyl alcohol) (PVA) composite were observed in DSC melting endotherms. This suggested that each CNT had a discrete crystalline polymer layer associated with it, which was supported by evidence from SEM imaging [69]. Indeed, others have observed polymer sheathing of CNTs protruding from fracture surfaces [39]. An equation for the composite crystallinity was deduced [69]:

TABLE 35.3. *Evidence of CNT-nucleated crystallinity in semicrystalline polymer matrices.*

Polymer matrix	Analytical method	Ref.
Polyamide-12	DSC	[105]
PEEK	DSC, XRD	[26]
PVA	DSC	[12,69]
PmPV	DSC, PL	[70]
PP	Density nonlinearity, DSC, XRD	[73,82]
UHMWPE	SEM	[66]

$$\chi = \frac{V_0 + N[\pi(R+b)^2 l_{NT} - \pi R^2 l_{NT}]}{V} \tag{35.2}$$

and given

$$V_{NT} = \frac{N \pi R^2 l_{NT}}{V}. \tag{35.3}$$

Substituting Eq. (35.3) into (35.2) and simplifying gives:

$$\chi = V_{NT}\left[\frac{b^2}{R^2} + 2\frac{b}{R}\right] + \frac{V_0}{V}. \tag{35.4}$$

This equation fit the DSC experimental data quite well resulting in a crystalline polymer interfacial layer thickness, b, of 21 ± 7 nm ($R = 7.5 \pm 2.5$ nm) (Figure 35.3). SEM measurement of MWNTs protruding from fractured surfaces agreed well with the DSC results indicating that $b = 25 \pm 10$ nm. It was also noted that the mean length of MWNTs protruding from the fracture surface was approximately $1.72 \pm 0.7\,\mu m \approx l_{NT}/4$. Mechanical testing of these MWNT/PVA composites yielded impressive mechanical property improvements, +370% in modulus and + 430% in strength at a loading of only 0.6 vol.% MWNTs.

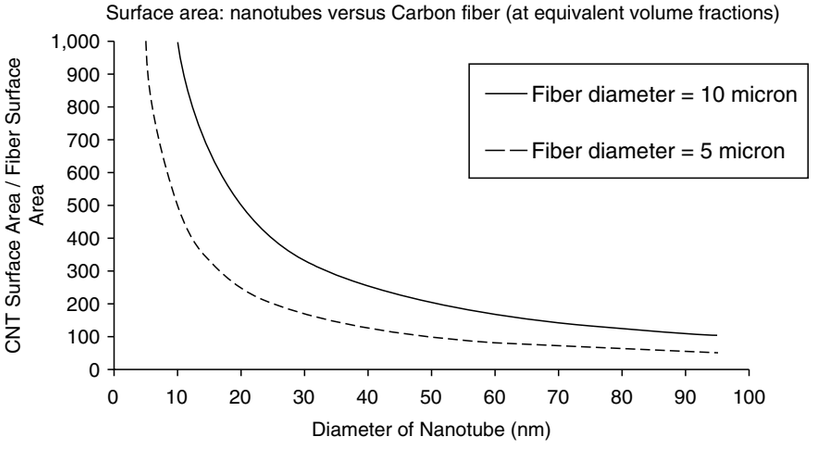

FIGURE 35.2. Increases in the ratio of CNT surface area to carbon fiber surface area as a function of the CNT diameter. Two typical carbon fiber diameters are compared.

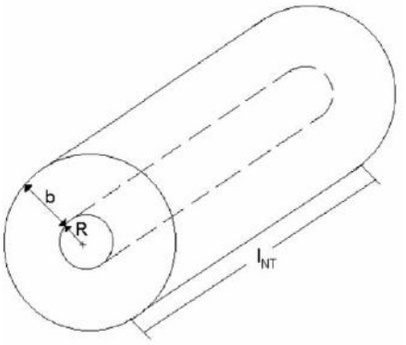

R = MWNT radius
b = crystalline polymer layer thickness
l_{NT} = MWNT length
χ = Total volume fraction polymer crystallinity
V_0 = Initial volume of neat polymer crystallinity
V_{NT} = MWNT volume fraction
N = Number of MWNTs
V = Total volume of composite

FIGURE 35.3. Crystalline Polymer Sheathing of carbon nanotube.

Inspection of the fracture surfaces of these and other composites [39,69] supports the contention that failure occurs at the interface between a crystalline polymer layer bound to the nanotube surface and the bulk polymer. This implies that the MWNTs are not being strained to failure, and that the nanotube interface with the matrix is strong enough to stay intact (i.e., the MWNT + crystalline polymer sheath are acting as a single unit). As a first approximation, short fiber composite theory has been used to model this effect since it generally applies to composites containing short fibers that cannot be strained to failure by stress transfer from the matrix. Composite strength can then be represented by:

$$\sigma_C = \left(\frac{l_{NT}\tau}{2R} - \sigma_P\right)V_{NT} + \sigma_P, \tag{35.5}$$

where τ is the interfacial shear strength between the fiber surface and the matrix.

Applying this model to MWNT/PVA composites resulted in a predicted interfacial shear strength, τ, of 348 $\pm$ 231 MPa, about an order of magnitude higher than expected. Thus, Eq. (35.5) was modified to allow for the observed interfacial failure at the boundary between the bulk polymer and the crystalline polymer layer (thickness = b) adhering to the MWNT surface.

The argument from Coleman *et al*. [69] proceeded as follows. The stress required to break the MWNT/PVA composite is the sum of the stress required to fracture the matrix and the shear stress required to fail the bulk polymer–crystalline polymer layer interface.

$$\sigma_C A = \sigma_{poly}A_{bulk} + \sigma_{shear}A_{Interface}. \tag{35.6}$$

To determine the cross-sectional areas A_{bulk} and $A_{Interface}$, the number of nanotubes, n, in a given cross-section of the composite was calculated assuming all of the MWNTs were oriented perpendicular to the fracture surface, and that each had a cylindrical volume of matrix associated with it (diameter = $2a$) such that $n(\pi a^2) = A$, the total cross-sectional area. To determine a, characterizing ideal aerial dispersion of the nanotubes, the volume fraction of nanotubes in the composite, V_{NT}, was related to the volume of matrix per nanotube, $V_{matrix/NT}$:

$$V_{matrix/NT} = \frac{V}{N} \text{ with } V_{NT} = \frac{N\pi R^2 l_{NT}}{V} \tag{35.7}$$

$$V_{matrix/NT} = \frac{\pi R^2 l_{NT}}{V_{NT}} = \pi a^2 l_{NT} \; a = \frac{R}{\sqrt{V_{NT}}} \tag{35.8}$$

and

$$A = \frac{n\pi R^2}{V_{NT}}. \tag{35.9}$$

The area of the interface and the bulk area were then calculated:

$$A_{Interface} = n2\pi(R+b)1_{pullout} \tag{35.10}$$

and

$$A_{bulk} = A - n\pi(R+b)^2. \tag{35.11}$$

Substituting Eqs. (35.9), (35.10), and (35.11) into Eq. (35.6), and allowing $l_{pullout} = l_{NT}/4$ (consistent with SEM observations) produces an expression for the composite strength:

$$\sigma_C = \sigma_{poly} + V_{NT}\left[\frac{\sigma_{shear}l_{NT}}{2R} - \sigma_{poly}\left(1+\frac{b}{R}\right)\right]\left(1+\frac{b}{R}\right). \tag{35.12}$$

This expression reduces to Eq. (35.5) for $b = 0$ and $\sigma_{shear} = \tau$, validating the form. Fitting experimental data to Eq. (35.12), yields a value for the interfacial polymer-bulk polymer shear strength, σ_{shear}, of 95 $\pm$ 64 MPa. This is consistent with the crystalline polymer layer remaining intact with the MWNT surface. It is worth noting that as b gets large relative to the nanotube radius, then $A_{bulk} \rightarrow 0$. This implies that the matrix can become all interfacial polymer at some volume fraction of nanotubes, V^*_{NT}, less than one.

$$V^*_{NT} = \frac{1}{\left(1+\frac{b}{R}\right)^2}. \tag{35.13}$$

Clearly, the key issue is that for nanotube–polymer composites in which an increase in crystallinity is observed, fundamental changes in the way traditional micromechanical composite theory is applied may be necessary.

Consideration must be given to the formation of crystalline polymer coatings, which strongly adhere to the nanotubes. Promoting the growth of this layer, perhaps by using smaller diameter nanotubes capable of seeding thick crystalline coatings, may optimize reinforcement for particular polymer matrices [69]. Small diameter, easily dispersed multiwall carbon nanotubes grown in aligned arrays have been cited numerous times as being efficient at mechanical reinforcement, and may thus fill this role [12,33,68,105].

Changes in the elastic modulus of polymers initiated by the introduction of dispersed CNTs can be equally revealing about the mechanism of material reinforcement in which they participate. These are again related to the fundamental importance of increased surface area/volume ratio of CNTs [12]. Composites of PVA containing various types of carbon nanotubes were produced, and the increase in tensile modulus of each were analyzed. Neither a rule-of-mixture nor Halpin-Tsai approach to modeling the data worked well. However, it was recognized that the rate at which the composite modulus increased with increasing nanotube volume fraction was related to the mean diameter of the nanotubes used. This rate decreased as the diameter increased. A log–log plot of the rate of modulus increase versus nanotube diameter resulted in a straight line with a slope of -1, suggesting that the efficiency of reinforcement of the PVA is inversely proportional to the nanotube diameter, or directly proportional to the ratio of the surface area to volume of the nanotubes.

$$\frac{E_C - E_m}{E_m} = k\frac{N}{V}(2\pi R l_{NT}). \tag{35.14}$$

Plotting E_C/E_m versus the nanotube surface area per total volume, $(N/V)(2\pi R l_{NT})$ did indeed result in almost all of the data falling on one master straight line of slope k. (SWNT bundles did not follow the trend due to difficulty in dispersing individual SWNTs [12])

Using Eq. (35.7) in (35.14) yields,

$$\frac{E_C}{E_m} = \frac{2kV_{NT}}{R} + 1, \tag{35.15}$$

where k is the constant of proportionality relating the increase in CNT surface area per unit volume to the increase in composite modulus. The relationship between the composite modulus and the CNT surface area was shown to be linked to crystallization of the matrix polymer at the CNT surface, independent of the CNT type or concentration of lattice defects. From DSC results a differentiated form of Eq. (35.4) was shown to predict the composite crystallinity. Another group reported that the inclusion of Carbon nanofibres (CNFs) in PEEK only nucleated crystal growth when aligned in a drawn fiber matrix, and proposed that the induced strains and changes in polymer orientation due to the presence of the CNFs led to the development of crystallinity, not simply surface heteronucluation [26]. They furthermore report that the PEEK crystallinity is not enhanced by doubling the CNF concentration from 5 to 10 wt.%, a consequence alluded to, in part, by Eq. (35.13).

35.5 CONCLUSIONS

CNT-polymer composites are an emerging new class of composite materials with unique and promising mechanical properties. Considering the problems of CNT dispersion, orientation and processing, significant progress has been made in realizing their potential to enhance the properties of matrices to which they are added. The dependence of the CNT–polymer composite properties on these issues, as well as others such as CNT diameter, length, and interfacial matrix crystallization, has been recognized and used to develop models to predict and optimize the variables for maximum composite performance. The results presented by Coleman *et al.* [69] represent the most efficient enhancements in matrix mechanical properties published to date. An effective modulus of the embedded MWNTs in PVA films of 1984 ± 239 GPa was observed resulting in enhancement of the composite by 370% in modulus, 430% in strength, and 170% in toughness at only 0.6 vol.% loading of small diameter (15 ± 5 nm) MWNTs. These enhancements represent the level of performance researchers have hoped to see since the inception of CNT composites. It remains to be seen if similar effects can be demonstrated in other, perhaps more useful, polymer matrices. However, given the mechanical properties of CNTs, realization of the full potential of CNT-reinforced polymers has yet to be achieved. Further advances in this field, especially when coupled with other properties such as enhanced thermal and electrical conductivity, have promise to result in wide application of truly multifunctional materials. This ultimately represents the greatest potential of CNT–polymer composites; allowing for the possibility of reinforced polymers that can operate at high heat loads, conduct electricity, and shield EMI radiation simultaneously. CNT–polymer composites enabling these applications, while offering lighter weights and increased manufacturability over current materials, will undoubtedly advance the engineering capabilities of polymer composites.

ABBREVIATIONS

CNT	Carbon nanotube
MWNT	Multiwall carbon nanotube (diameter $\sim$ 10–100 nm)
SWNT	Singlewall carbon nanotube (diameter $\sim$ 1 nm)
CNF	Carbon nanofiber (diameter $\sim$ 200 nm)
PAN	poly(acrylonitrile)
PE	poly(ethylene)
HDPE	high density poly(ethylene)
UHMWPE	ultra-high molecular weight poly(ethylene)
PS	poly(styrene)
PMMA	poly(methyl methacrylate)
PMEA	poly(methyl ethyl methacrylate)
PVA	poly(vinylalcohol)
PEEK	poly(ether ether ketone)
PP	poly(propylene)

cl-PP	chlorinated poly(propylene)
PBO	poly(*p*- phenylene benzobisoxazole)
PC	poly(carbonate)
PmPV	poly(*m*-phenylenevinylene-*co*-2,5-dioctyloxy-*p*-phenylenevinylene)
FWHM	full peak width at half-maximum

REFERENCES

1. Iijima, S. Helical Microtubules of Graphitic Carbon. *Nature* **354**, 56–58 (1991).
2. Sinnott, S. B. & Andrews, R. Carbon Nanotubes: Synthesis, Properties, and Applications. *Crit. Rev. Solid State Mater. Sci.* **26**, 145–249 (2001).
3. Lambin, P. Electronic structure of carbon nanotubes. *Comptes Rendus Physique* **4**, 1009–1019 (2003).
4. Kaneto, K., Tsuruta, M., Sakai, G., Cho, W. Y. & Ando, Y. Electrical conductivities of multi-wall carbon nano tubes. *Synth. Metals* **103**, 2543–2546 (1999).
5. Berber, S., Kwon, Y. K. & Tomanek, D. Unusually high thermal conductivities of carbon nanotubes. *Phys. Rev. Lett.* **84**, 4613–4616 (2000).
6. Kim, P., Shi, L., Majamdar, A. & McEuen, P. L. Thermal transport measurments of individual multiwalled nanotubes. *Phys. Rev. Lett.* **87**, 215502–1 (2001).
7. Saito, R., Dresselhaus, G. & Dresselhaus, M. S. *Physical Properties of Carbon Nanotubes* (Imperial College Press, London, 1998).
8. Salvetat-Delmotte, J.-P. & Rubio, A. Mechanical properties of carbon nanotubes: a fiber digest for beginners. *Carbon* **40**, 1729–1734 (2001).
9. Thess, A. *et al*. Crystalline ropes of metallic carbon nanotubes. *Science* **273**, 483–487 (1996).
10. Andrews, R., Jacques, D., Qian, D. & Rantell, T. Multiwall carbon nanotubes: synthesis and application. *Acc. Chem. Res.* **35**, 1008–1017 (2002).
11. Donnet, J.-B., Wang, T. K., Peng, J. C. M. & Rebouillat, S. (eds.) *Carbon Fibers Third Edition, Revised and Expanded* (Marcel Dekker Inc., New York, 1998).
12. Cadek, M. *et al*. Reinforcement of polymers with carbon nanotubes: The role of nanotube surface area. *Nano Lett.* **4**, 353–356 (2004).
13. Yu, M.-F. *et al*. Strength and breaking mechanism of multiwalled carbon nanotubes under tensile load. *Science* **287**, 637–640 (2000).
14. Yu, M.-F., Yakobson, B. I. & Ruoff, R. Controlled sliding and pullout of nested shells in individual multiwalled carbon nanotubes. *J. Phys. Chem.* **104**, 8764–8767 (2000).
15. Hwang, G. L., Shieh, Y.-T. & Hwang, K. C. Efficient load transfer to polymer-grafted multiwalled carbon nanotubes in polymer composites. *Adv. Funct. Mater.* **14**, 487–491 (2004).
16. Zhang, Y., Gu, H. & Lijima, S. Single-wall carbon nanotubes synthesized by laser ablation in a nitrogen atmosphere. *Appl. Phys. Lett.* **73**, 3827–3829 (1998).
17. Andrews, R. *et al*. Continuous production of aligned carbon nanotubes: a step closer to commercial realization. *Chem. Phys. Lett.* **303**, 467–474 (1999).
18. Krishnan, A., Dujardin, E., Ebbesen, T. W., Yianilos, P. N. & Treacy, M. M. J. Young's modulus of single-walled nanotubes. *Phys. Rev. B* **58**, 14013–14019 (1998).
19. Lier, G. V., Alsenoy, C. V., Doren, V. V. & Geerlings, P. Ab initio study of the elastic properties of single-walled carbon nanotubes and graphene. *Chem. Phys. Lett.* **326**, 181–185 (2000).
20. Schadler, L. S., Giannaris, S. C. & Ajayan, P. M. Load transfer in carbon nanotube epoxy composites. *Appl. Phys. Lett.* **73**, 3842–3844 (1998).
21. Nardelli, M. B., Yakobson, B. I. & Bernholc, J. Brittle and ductile behavior in carbon nanotubes. *Phys. Rev. Lett.* **81**, 4656–4659 (1998).
22. Walters, D. A. *et al*. Elastic strain of freely suspended single-wall carbon nanotube ropes. *Appl. Phys. Lett.* **74**, 3803–3805 (1999).
23. Treacy, M. M. J., Ebbesen, T. W. & Gibson, J. M. Exceptionally high Young's modulus observed for individual carbon nanotubes. *Nature* **381**, 678–680 (1996).
24. Demczyk, B. G. *et al*. Direct mechanical measurement of the tensile strength and elastic modulus of multiwalled carbon nanotubes. *Mater. Sci. Eng.* **A334**, 173–178 (2002).
25. Wagner, H. D., Lourie, O., Feldman, Y. & Tenne, R. Stress-induced fragmentation of multiwall carbon nanotubes in a polymer matrix. *Appl. Phys. Lett.* **72**, 188–190 (1998).
26. Sandler, J. *et al*. Carbon-nanofibre-reinforced poly(ether ether ketone) fibres. *J. Mater. Science* **38**, 2135–2141 (2003).
27. Applied Sciences (2005). Properties of Pyrograf I, http://www.apsci.com/ngm-pyro1.html
28. Bacon, R. Growth, structure, and properties of graphitic whiskers. *J. Appl. Phys.* **31**, 283–290 (1960).
29. Hexcel. (2005). Continuous carbon fiber data, http://www.hexcelfibers.com/ Markets/Products/Continuous/ _Productlist.htm
30. Toray (2005). Carbon fiber data, http://www.torayca.com/index2.html
31. Siochi, E. J. *et al*. Melt processing of SWCNT-polyimide nanocomposite fibers. *Compos. Part B: Eng.* **35**, 439–446 (2004).
32. Zeng, J., Saltysiak, B., Johnson, W. S., Schiraldi, D. A. & Kumar, S. Processing and properties of poly(methyl methacrylate)/carbon nano fiber composites. *Compos. Part B: Eng.* **35**, 173–178 (2004).
33. Gorga, R. E. & Cohen, R. E. Toughness enhancements in poly(methyl methacrylate) by addition of oriented multiwall carbon nanotubes. *J. Polym. Sci.: Part B: Polym. Phys.* **42**, 2690–2702 (2004).
34. Advani, S. G. & Fan, Z. in *Materials Processing and Design: Modeling, Simulation, and Applications, NUMIFORM 2004* (eds. Ghosh, S., Castro, J. C. & Lee, J. K.) 1619–1623 (American Institute of Physics, 2004).
35. Shaffer, M. S. P., Fan, X. & Windle, A. H. Dispersion and packing of carbon nanotubes. *Carbon* **36**, 1603–1612 (1998).
36. Shaffer, M. S. P. & Windle, A. H. Analogies between polymer solutions and carbon nanotube dispersions. *Macromolecules* **32**, 6864–6866 (1999).
37. Zeng, J., Saltysiak, B., Johnson, W. S., Schiraldi, D. A. & Kumar, S. Processing and properties of poly(methyl methacrylate)/carbon nano fiber composites. *Compos. Part B: Eng.* **35**, 173–178 (2004).
38. Weisenberger, M. C., Grulke, E. A., Jacques, D., Rantell, T. & Andrews, R. Enhanced mechanical properties of polyacrylonitrile/multiwall carbon nanotube composite fibers. *J. Nanosci. Nanotechnol.* **3**, 535–539 (2003).
39. Ding, W. *et al*. Direct observation of polymer sheathing in carbon nanotube-polycarbonate composites. *Nano Lett.* **3**, 1593–1597 (2003).
40. Dalton, A. B. *et al*. Super-tough carbon-nanotube fibres. *Nature* **423**, 703 (2003).
41. Fisher, F. T., Bradshaw, R. D. & Brinson, L. C. Fiber waviness in nanotube-reinforced polymer composites-I: Modulus predictions using effective nanotube properties. *Compos. Sci. Technol.* **63**, 1689–1703 (2003).
42. Hammel, E. *et al*. Carbon nanofibres for composite applications. *Carbon* **42**, 1153–1158 (2004).
43. Kearns, J. C. & Shambaugh, R. L. Polypropylene fibers reinforced with carbon nanotubes. *J. Appl. Polym. Sci.* **86**, 2079–2084 (2002).
44. Fuchs, F. J. In *45th Annual Technical Conference of Society of Vacuum Coaters* ISSN 0737–5921, 64–67 (2002).
45. Sandler, J. K. W. *et al*. A comparative study of melt spun polyamide-12 fibres reinforced with carbon nanotubes and nanofibres. *Polymer* **45**, 2001–2015 (2004).
46. Gong, X., Liu, J., Baskaran, S., Voise, R. D. & Young, J. S. Surfactant-assisted processing of carbon nanotube/polymer composites. *Chem. Mater.* **12**, 1049–1052 (2000).
47. Velasco-Santos, C., Martinez-Hernandex, A. L., Fisher, F. T., Ruoff, R. S. & Castano, V. M. Dynamical-mechanical and thermal analysis of carbon nanotube-methyl-ethyl methacrylate nanocomposites. *J. Phys. D: Appl. Phys.* **36**, 1423–1428 (2003).
48. Poulin, P., Vigolo, B. & Launois, P. Films and fibers of oriented single wall nanotubes. *Carbon* **40**, 1741–1749 (2002).
49. Velasco-Santos, C., Martinez-Hernandez, A. L., Fisher, F. T., Ruoff, R. S. & Castano, V. M. Improvement of thermal and mechanical properties of carbon nanotube composites through chemical functionalization. *Chem. Mater.* **15**, 4470–4475 (2003).
50. Haggenmueller, R., Gommans, H. H., Rinzler, A. G., Fischer, J. E. & Winey, K. I. Aligned single-wall carbon nanotubes in composites by melt processing methods. *Chem. Phys. Lett.* **330**, 219–225 (2000).

51. Bubert, H. *et al*. Characterization of the uppermost layer of plasma-treated carbon nanotubes. *Diamond Related Mater*. **12**, 811–815 (2003).
52. Kim, B. & Sigmund, W. M. Functionalized multiwall carbon nanotube/gold nanoparticle composites. *Langmuir* **20**, 8239–8242 (2004).
53. Esumi, K., Ishigami, A., Nakajima, A., Sawadi, K. & Honda, H. *Carbon* **34**, 279 (1996).
54. Eitan, A., Jiang, K., Dukes, D., Andrews, R. & Schadler, L. S. Surface modification of multiwalled carbon nanotubes: toward the tailoring of the interface in polymer composites. *Chem. Mater*. **15**, 3195–3201 (2003).
55. Valentini, L., Armentano, I., Puglia, D. & Kenny, J. M. Dynamics of amine functionalized nanotubes/epoxy composites by dielectric relaxation spectroscopy. *Carbon* **42**, 323–329 (2004).
56. Kyke, C. A., Stewart, M. P., Maya, F. & Tour, J. M. Diazonium-based functionalization of carbon nanotubes: XPS and GC–MS analysis and mechanistic implications. *Synlett* **1**, 155–160 (2004).
57. Holzinger, M. *et al*. Sidewall functionalization of carbon nanotubes. *Angew. Chem. Int., Ed*. **40**, 4002–4005 (2001).
58. Moghaddam, M. J. *et al*. Highly efficient binding of DNA on the sidewalls and tips of carbon nanotubes using photochemistry. *Nano Lett*. **4**, 89–93 (2004).
59. Pantarotto, D. *et al*. Synthesis, structural characterization and immunological properties of carbon nanotubes functionalized with peptides. *J. Am. Chem. Soc*. **125**, 6160–6164 (2003).
60. Dyke, C. A. & Tour, J. M. Solvent-free functionalization of carbon nanotubes. *J. Am. Chem. Soc*. **125**, 1156–1157 (2003).
61. Lozano, K., Yang, S. & Jones, R. E. Nanofiber toughened polyethylene composites. *Carbon* **42**, 2329–2331 (2004).
62. Jin, Z., Pramoda, K. P., Xu, G. & Goh, S. H. Dynamic mechanical behavior of melt-processed multi-walled carbon nanotube/poly (methyl methacrylate) composites. *Chem. Phys. Lett*. **337**, 43–47 (2001).
63. Kashiwagi, T. *et al*. Thermal degradation and flammability properties of poly(propylene)/carbon nanotube composites. *Macromol. Rapid Commun*. **23**, 761–765 (2002).
64. Jin, L., Bower, C. & Zhou, O. Alignment of carbon nanotubes in a polymer matrix by mechanical stretching. *Appl. Phys. Lett*. **73**, 1197–1199 (1998).
65. Shaffer, M. S. P. & Windle, A. H. Fabrication and characterization of carbon nanotube/poly(vinyl alcohol) composites. *Adv. Mater*. **11**, 937–941 (1999).
66. Ruan, S. L., Gao, P., Yang, X. G. & Yu, T. X. Toughening high performance ultrahigh molecular weight polyethylene using multiwalled carbon nanotubes. *Polymer* **44**, 5643–5654 (2003).
67. Ajayan, P. M., Stephan, O., Colliex, C. & Traught, D. Aligned carbon nanotube arrays formed by cutting a polymer resin–nanotube composite. *Science* **265**, 1212–1214 (1994).
68. Cadek, M. *et al.* in *Molecular Nanostructures: XVII Int'l. Winterschool/Euroconference on Electronic Properties of Novel Materials* (eds. Kuzmany, H., Fink, J., Mehring, M. & Roth, S.) 269–272 (American Institute of Physics, 2003).
69. Coleman, J. N. *et al*. High-performance nanotube-reinforced plastics: understanding the mechanism of strength increase. *Adv. Funct. Mater*. **14**, 791–798 (2004).
70. Ryan, K. P. *et al*. Carbon-nanotube nucleated crystallinity in a conjugated polymer based composite. *Chem. Phys. Lett*. **391**, 329–333 (2004).
71. Cadek, M., Coleman, J. N., Barron, V., Hedicke, K. & Blau, W. J. Morphological and mechanical properties of carbon-nanotube-reinforced semicrystalline and amorphous polymer composites. *Appl. Phys. Lett*. **81**, 5123–5125 (2002).
72. Stephan, C. *et al*. Characterization of singlewalled carbon nanotubes–PMMA composites. *Synth. Metals* **108**, 139–149 (2000).
73. Assouline, E. *et al*. Nucleation ability of multiwall carbon nanotubes in polypropylene composites. *J. Polym. Sci.: Part B: Polym. Phys*. **41**, 520–527 (2003).
74. Thostenson, E. T. & Chou, T.-W. Aligned multi-walled carbon nanotube-reinforced composites: processing and mechanical characterization. *J. Phys. D: Appl. Phys*. **35**, L77–L80 (2002).
75. Lourie, O., Cox, D. M. & Wagner, H. D. Buckling and collapse of embedded carbon nanotubes. *Phys. Rev. Lett*. **81**, 1638–1641 (1998).
76. Tibbetts, G. & McHugh, J. J. Mechanical properties of vapor-grown carbon fiber composites with thermoplastic matrices. *J. Mater. Res*. **14**, 2871–2880 (1999).
77. Koratkar, N., Wei, B. & Ajayan, P. Carbon nanotube films for damping applications. *Adv. Mater*. **14**, 997–1000 (2002).
78. Koratkar, N. A., Wei, B. & Ajayan, P. M. Multifunctional structural reinforcement featuring carbon nanotube films. *Compos. Sci. Technol*. **63**, 1525–1531 (2003).
79. Coleman, J. N. *et al*. Improving the mechanical properties of single-walled carbon nanotube sheets by intercalation of polymeric adhesives. *Appl. Phys. Lett*. **82**, 1682–1684 (2003).
80. Wang, Z. J. Z. *et al*. Study on poly(methyl methacrylate)/carbon nanotube composites. *Mater. Sci. Eng*. **A271**, 395–400 (1999).
81. Ajayan, P. M. Aligned carbon nanotubes in a thin polymer film. *Adv. Mater*. **7**, 489–491 (1995).
82. Moore, E. M., Ortiz, D. L., Marla, V. T., Shambaugh, R. L. & Grady, B. P. Enhancing the strength of polypropylene fibers with carbon nanotubes. *J. Appl. Polym. Sci*. **93**, 2926–2933 (2004).
83. Kumar, S., Doshi, H., Srinivasarao, M., Park, J. O. & Schiraldi, D. A. Fibers from polypropylene/nano carbon fiber composites. *Polymer* **43**, 1701–1703 (2002).
84. Vigolo, B., Poulin, P., Lucas, M., Luanois, P. & Bernier, P. *Appl. Phys. Lett*. **81**, 1210–1212 (2002).
85. Barisci, J. N. *et al*. Properties of carbon nanotube fibers spun from DNA-stabilized dispersions. *Adv. Funct. Mater*. **12**, 133–138 (2004).
86. Sreekumar, T. V. *et al*. Polyacrylonitrile single-walled carbon nanotube composite fibers. *Adv. Mater*. **16**, 58–61 (2004).
87. Kumar, S. *et al*. Synthesis, structure, and properties of PBO/SWNT composites. *Macromolecules* **35**, 9039–9043 (2002).
88. Ding, B., Kim, H. Y., Lee, S. C., Lee, D. R. & Choi, K. J. Preparation and characterization of nanoscaled poly(vinyl alcohol) fibers via electrospinning. *Fibers Polym*. **3**, 73–79 (2002).
89. Ko, F. *et al.* Electrospinning of continuous carbon nanotube-filled nanofiber yarns. *Adv. Mater*. **15**, 1161–1165 (2003).
90. Seoul, C., Kim, Y.-T. & Berk, C.-K. Electrospinning of poly(vinylidence fluoride)/dimethylformamide solutions with carbon nanotubes. *J. Polym. Sci.: Part B: Polym. Chem*. **41**, 1572–1577 (2003).
91. Mallick, P. K. *Fiber Reinforced Composites: Materials, Manufacturing, and Design* (Marcel Dekker, Inc., New York, 1993).
92. Lucas, M. *et al*. in *Structural and Electronic Properties of Molecular Nanostructures* (ed. Kuzmany, H.) 579–582 (American Institute of Physics, 2002).
93. Bower, C., Rosen, R., Jin, L., Han, J. & Zhou, O. Deformation of carbon nanotubes in nanotube–polymer composites. *Appl. Phys. Lett*. **74**, 3317–3319 (1999).
94. Ajayan, P. M., Schadler, L. S., Giannaris, C. & Rubio, A. Single-walled carbon nanotube–polymer composites: strength and weakness. *Adv. Mater*. **12**, 750–753 (2000).
95. Cooper, C. A., Young, R. J. & Halsall, M. Investigation into the deformation of carbon nanotubes and their composites through the use of Raman spectroscopy. *Compos. Part A: Appl. Sci. Manufact*. **32**, 401–411 (2001).
96. Wood, J. R., Zhao, Q. & Wagner, H. D. Orientation of carbon nanotubes in polymers and its detection by Raman spectroscopy. *Compos. Part A: Appl. Sci. Manufact*. **32**, 391–399 (2001).
97. Hobbie, E. K., Wang, H., Kim, H., Lin-Gibson, S. & Grulke, E. A. Orientation of carbon nanotubes in a sheared polymer melt. *Phys. Fluids* **15**, 1196–1202 (2003).
98. Lin-Gibson, S., Pathak, J. A., Grulke, E. A., Wang, H. & Hobbie, E. K. Elastic flow instability in nanotube suspensions. *Phys. Rev. Lett*. **92**, 0483021–0483024 (2004).
99. Qian, D., Dickey, C., Andrews, R. & Rantell, T. Load transfer and deformation mechanisms in carbon nanotube–polystyrene composites. *Appl. Phys. Lett*. **76**, 1–4 (2000).
100. Lourie, O. & Wagner, H. D. Transmission electron microscopy observations of fracture of single-wall carbon nanotubes under axial tension. *Appl. Phys. Lett*. **73**, 3527–3529 (1998).
101. Dalton, A. B. *et al*. Continuous carbon nanotube composite fibers: properties, potential applications, and problems. *J. Mater. Chem*. **14**, 1–3 (2004).
102. Marrs, B., Andrews, R., Pienkowski, D. & Rantell, T. in *Orthopaedic Research Society* (San Francisco, 2004).

103. Ren, Y., Li, F., Cheng, H.-M. & Liao, K. Tension–tension fatigue behavior of unidirectional single-walled carbon nanotube reinforced epoxy composite. *Carbon* **41**, 2159–2179 (2003).
104. Singh, S., Pei, Y., Miller, R. & Sundararajan, P. R. Long-range, entangled carbon nanotube networks in polycarbonate. *Adv. Funct. Mater.* **13**, 868–872 (2003).
105. Sandler, J. K. W. *et al*. A comparative study of melt spun polyamide-12 fibres reinforced with carbon nanotubes and nanofibres. *Polymer* **45**, 2001–2015 (2004).
106. Bradshaw, R. D., Fisher, F. T. & Brinson, L. C. Fiber waviness in nanotube-reinforced polymer composites. II. Modeling via numerical approximation of the dilute strain concentration tensor. *Compos. Sci. Technol.* **63**, 1705–1722 (2003).
107. Berhan, L., Li, Y. B. & Sastry, A. M. Effect of nanorope waviness on the effective moduli of nanotube sheets. *J. Appl. Phys.* **95**, 5027–5034 (2004).
108. Yi, Y. B., Berhan, L. & Sastry, A. M. Statistical geometry of random fibrous networks, revisited: waviness, dimensionality, and percolation. *J. Appl. Phys.* **96**, 1318–1327 (2004).
109. Thostenson, E. T. & Chou, T.-W. On the elastic properties of carbon nanotube-based composites: modelling and characterization. *J. Phys. D: Appl. Phys.* **36**, 573–582 (2003).
110. Frankland, S. J. V. & Harik, V. M. Analysis of carbon nanotube pull-out from a polymer matrix. *Surf. Sci.* **525**, L103–L108 (2003).
111. Liao, K. & Li, S. Interfacial characteristics of a carbon nanotube–polystyrene composite system. *Appl. Phys. Lett.* **79**, 4225–4227 (2001).
112. Garg, A. & Sinnott, S. B. Effect of chemical functionalization on the mechanical properties of carbon nanotubes. *Chem. Phys. Lett.* **295**, 273–278 (1998).
113. Namilae, S., Chandra, N. & Shet, C. Mechanical behavior of functionalized nanotubes. *Chem. Phys. Lett.* **387**, 247–252 (2004).
114. Barber, A. H., Cohen, S. R. & Wagner, H. D. Measurement of carbon nanotube–polymer interfacial strength. *Appl. Phys. Lett.* **82**, 4140–4142 (2003).
115. Narh, K. A. & Zhu, L. Numerical simulation of the effect of nanotube orientation on tensile modulus of carbon-nanotube-reinforced polymer composites. *Polym. Int.* **53**, 1461–1466 (2004).
116. Hilding, J., Grulke, E. A., Zhang, Z. G. & Lockwood, F. Dispersion of carbon nanotubes in liquids. *J. Dispers. Sci. Technol.* **24**, 1–41 (2003).
117. Cox, H. L. The elasticity and strength of paper and other fibrous materials. *Br. J. Appl. Phys.* **3**, 72–79 (1952).

CHAPTER 36

Reinforcement Theories

Gert Heinrich*, Manfred Klüppel†, and Thomas Vilgis‡

*Leibniz-Institut für Polymerforschung Dresden eV, Hohe Str. 6, D-01069 Dresden, Germany;
†Deutsches Institut für Kautschuktechnologie eV, Eupener Str. 33, D-30519 Hannover, Germany;
‡Max-Planck-Institut für Polymerforschung Postfach 3148, D-55021 Mainz, Germany

36.1 INTRODUCTION

The use of fillers—especially, carbon black or precipitated silica—, together with accelerated sulfur vulcanization, has remained the fundamental technique for achieving the incredible range of mechanical properties required for a great variety of modern rubber products. Increased reinforcement of the rubber material has been defined as increased stiffness, modulus, rupture energy, tear strength, tensile strength, cracking resistance, fatigue resistance, and abrasion resistance. Accordingly, a practical definition of reinforcement is the improvement in the service life of rubber articles that fail in a variety of ways, one of the most important being rupture failure accelerated by fatigue processes, such as occurs during the wear of a tire tread.

The main intention of the present contribution is to gain further inside into the relationship between disordered filler structures and the reinforcement of elastomers which is discussed mainly for the static and dynamic (shear or tensile) modulus. We will recognize that the classical approaches to (filled) rubber elasticity are not sufficient to describe the physics of such disordered systems. Instead, different theoretical methods have to be employed to deal with the various interactions and, consequently, reinforcing mechanisms on different length scales (see [1] and references therein).

36.2 HYDRODYNAMIC REINFORCEMENT AND THE ROLE OF POLYMER–FILLER INTERFACE

In the case of a dilute suspension of spherical inclusions the increase of the shear modulus G of filled rubbers is:

$$f = \frac{G}{G_0} = 1 - \frac{15(1-\nu_m)\left(1-\frac{G_i}{G_0}\right)\Phi}{7-5\nu_m+2(4-5\nu_m)\frac{G_i}{G_0}}, \qquad (36.1)$$

where ϕ is the volume fraction of the inclusions, ν_m is the Poisson ratio of the matrix, and the subscripts i and *0* refer to the inclusions and the matrix, respectively. With the assumption of perfectly rigid inclusions ($G_i \gg G_0$) and an incompressible matrix, $\nu_m = 1/2$, Eq. (36.1) becomes the Einstein-Smallwood equation:

$$f = 1 + \frac{5}{2}\Phi. \qquad (36.2)$$

Guth and Gold extended relationship in Eq. (36.2) to higher concentrations taking inter-particle disturbances into account. They found:

$$f = 1 + \frac{5}{2}\Phi + 14.1\Phi^2. \qquad (36.3)$$

However, for typical loadings of fillers up to volume fraction $\Phi \approx 0.35$, a Padé approximation of the expansion of f up to second order in the volume fraction,

$$f \approx 1 + \frac{5}{2}\Phi + 5.0\Phi^2 + \cdots \approx 1 + \frac{2.5\Phi}{1 - 2\Phi} \qquad (36.4)$$

turned out to be a suitable and theoretically founded expression for f. If the hypothesis of spherical particles is released, Eqs. (36.3), (36.4) do not have anymore a univocal formulation. For active fillers, however, f no longer depends on the simple filler volume fraction Φ but on some effective volume fraction Φ_{eff}. Medalia [2] added ''occluded rubber'' volume to the actual carbon black filler volume to obtain the ''effective'' volume of the rigid phase. ''Occluded rubber'' was defined as the rubber part of the elastomeric matrix which penetrated the void space of the individual carbon aggregates, partially shielding it from deformation. Mullins and Tobin [3] have recommended the use of the same strain amplification factor of the modulus, f, to relate the external strain ε_μ of the sample in spatial direction μ to the internal strain ratio λ_μ of the filled rubber matrix

$$\lambda_\mu = 1 + f\varepsilon_\mu \quad \text{for } \mu = 1,2,3. \qquad (36.5)$$

Very recently, Westermann *et al*. gave the first direct microscopic insights into the mechanisms of strain enhancement in reinforced networks [4]. They investigated the matrix chain deformation by small-angle neutron scattering (SANS) using a special designed filler-matrix system, a triblock copolymer of the type PI-PS-PI with a polystyrene middle block of $\Phi_{\text{PS}} = 0.18$ and two symmetric polyisoprene wings. Due to the repulsive interaction between the PS and PI blocks, this block copolymer undergoes a thermodynamically driven microphase separation; i.e., for this composition spherical PS domains are formed that can be considered as model fillers. The degree of the in situ filling was adjusted by blending the PI-PS-PI starlike micelles with a PI homopolymer matrix as the soft rubbery phase.

Extrapolation of the SANS data in [4] to the isotropic state confirms, indirectly, the presence of a diffuse PS–PI transition layer between filler and rubbery matrix with thickness $\Delta \sim 0.5$ nm around the PS domain with a mean filler radius of about 84 Å. Excellent agreement between measured reinforcing factor and corresponding model predictions could be realized within a very recent approach of Huber and Vilgis [5] for the hydrodynamic reinforcement of rubbers filled with spherical fillers of core-shell structures [6].

These ideas provide some insight, though we assume that the particles are freely dispersed, but have themselves elastic properties, which is different from the matrix. Examples for such filler particles are elastic microgels. The general result for the effective shear modulus Eq. (36.1) can be written as:

$$\frac{G}{G_0} = 1 + \frac{[\mu]\Phi}{1 - \frac{2}{5}[\mu]\Phi}, \qquad (36.1')$$

where $[\mu]$ is the intrinsic modulus of the filled matrix, i.e.,

$$[\mu] \equiv \lim_{\Phi \to o} \frac{1}{\Phi}\left[\frac{G - G_0}{G_0}\right].$$

Hence this equation is a natural generalization of the Einstein-Smallwood reinforcement law. For rigid and spherical filler particles at low volume fraction, the Einstein-Smallwood formula is recovered, since in this case the intrinsic modulus $[\mu] = 5/2$ (the intrinsic modulus $[\mu]$ follows from the solution of a single-particle problem). Exact analytical results can be obtained for the most relevant cases, such as uniform soft spheres, which describe the softening of the material in a proper way, as well as in the case of soft cores and hard shells [5].

For the reinforcement the case of hard core/soft shell filler particles appears more relevant. To some extend this case can be even viewed as the simplest model of filler particles (hard core with large modulus) coated with a soft layer (bound rubber with a slightly larger modulus compared to the matrix). For this case the intrinsic modulus can be calculated exactly as well and the resulting reinforcement can be computed. Figures 36.1 and 36.2 show the effective modulus for the filled system. Most interesting is the strong increase in reinforcement even for small bound rubber thickness. The curves have quite realistic features. Unfortunately, for comparison with experimental data still values for the effective bound rubber thickness and strength are lacking.

Vieweg *et al*. [7] estimated an interface thickness of $\Delta \sim 1.5$ nm for polymeric fillers (microgels) consisting of cured polybutadiene with a glass transition temperature (shear loss factor maximum at frequency 1 Hz) of about 100°C. The filler particles diameters were in between ~24 and 75 nm; and the sample matrices were commercial statistical styrene–butadiene emulsion copolymers vulcanized with dicumylperoxide. The method they used in [7] was to

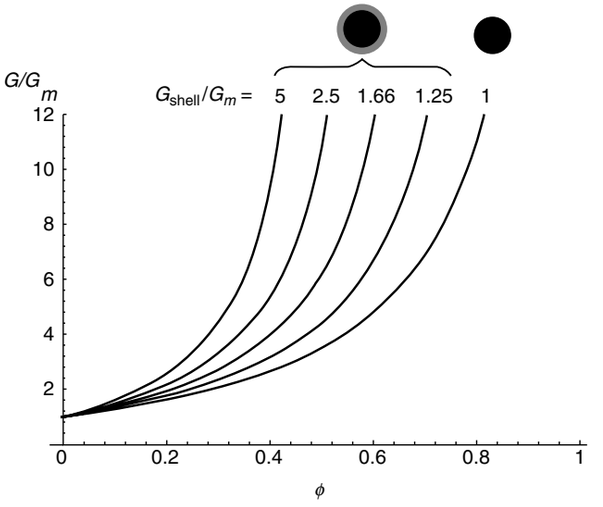

FIGURE 36.1. Filler particles with hard core: relative increase of the elastic modulus as a function of filler volume fraction for different values of the ratio shell modulus to matrix modulus The ratio between shell (total) and core radius is taken as 4/3.

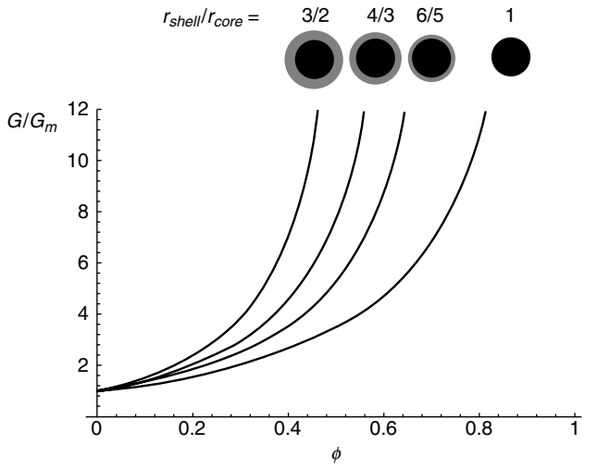

FIGURE 36.2. Filler particles with hard core: relative increase of the elastic modulus as a function of filler volume fraction for different values of the ratio between shell and core radius. The ratio shell modulus to matrix modulus of the individual particle is taken to be fixed as 2.

find the lengths of immobilized interfacial modes from optimum collapsing of (dynamic shear) data points in a scaling procedure; i.e., reinforcement in the dynamical experiments is explained by loss of mobility for longer polymer modes caused by too short lengths available. The glassy layer idea was recently improved in introducing the concept that there is a gradient of glass-transition temperature around each filler particle. This was suggested in [11] and quantified, on model filled elastomers, using both NMR and mechanical data [12–14]. Further theoretical explanations were proposed recently [15].

So far we reported some experimental determinations of the overstrain factor and filler–matrix interfaces for spherical model fillers. As already noted, active fillers like carbon black or silica are of special interest in rubber industry. First direct results of SANS measurements of the form factor of matrix chains in a cross-linked, silica filled elastomers in the isotropic state were reported, very recently, by Botti et al. [8]. Preliminary results show the influence of reinforcing agent, Si 69 in this case, on the reinforcing factor [9]. Si 69 is a bifunctional polysulfidic organosilane for the rubber industry defined chemically as *bis*(3-triethoxysilylpropyl)-tetrasulfane. It is used to improve the reinforcing capacity of fillers with silanol groups on their surface. Using this technology of precipitated silica and reinforcing agent, together with special solution polymerized statistically styrene–butadiene copolymers (S-SBR) as hydrocarbon polymer matrix, the *green tire tread* could be developed. The green tire technology dramatically improves fuel economy (rolling resistance) and overall performance (especially, antibraking-system supported wet skid behavior) over conventional tires [10].

36.3 FILLER NETWORKING AND REINFORCEMENT AT SMALL STRAIN

Filler networking in elastomer composites can be analyzed by applying TEM-flocculation- and dielectric investigations. This provides information on the fractal nature of filler networks as well as the morphology of filler–filler bonds. From the two dimensional graph in Fig. 36.3 it becomes obvious that TEM analysis gives a limited microscopic picture of the filler network morphology. This is mainly due to the spatial interpenetration of neighboring flocculated filler clusters.

Flocculation studies, considering the small strain mechanical response of the uncross-linked composites during heat treatment (annealing), demonstrate that a relative movement of the particles takes place that depends on particle size, molar mass of the polymer as well as polymer–filler and filler–filler interaction (Fig. 36.4). This provides strong experimental evidence for a kinetic cluster–cluster aggregation (CCA) mechanism of filler particles in the rubber matrix to form a filler network.

The ac-conductivity in the high frequency regime is related to an anomalous diffusion mechanism of charge carriers on fractal carbon black clusters, implying a power law behavior of the conductivity with frequency. This scaling behavior of the conductivity is observed in many carbon black filled elastomer systems. It confirms the fractal nature of filler networks in elastomers below a certain length scale, though it gives no definite information on the particular network structure [16–18]. From the dielectric investigations it becomes obvious that charge transport above the percolation threshold is limited by a hopping or tunneling mechanism of charge carriers over small gaps of order 1 nm between adjacent carbon black particles. From this finding

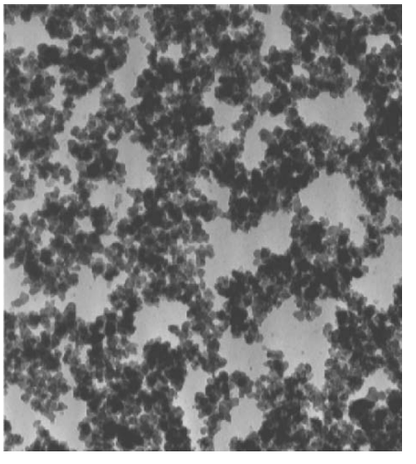

FIGURE 36.3. TEM micrograph of a carbon black network obtained from an ultrathin cut of a filled rubber sample. Reproduced from M. Klüppel and G. Heinrich, *Kautschuk, Gummi, Kunstsoffe* **58**, 217–224 (2005) with permission from Hüthig.

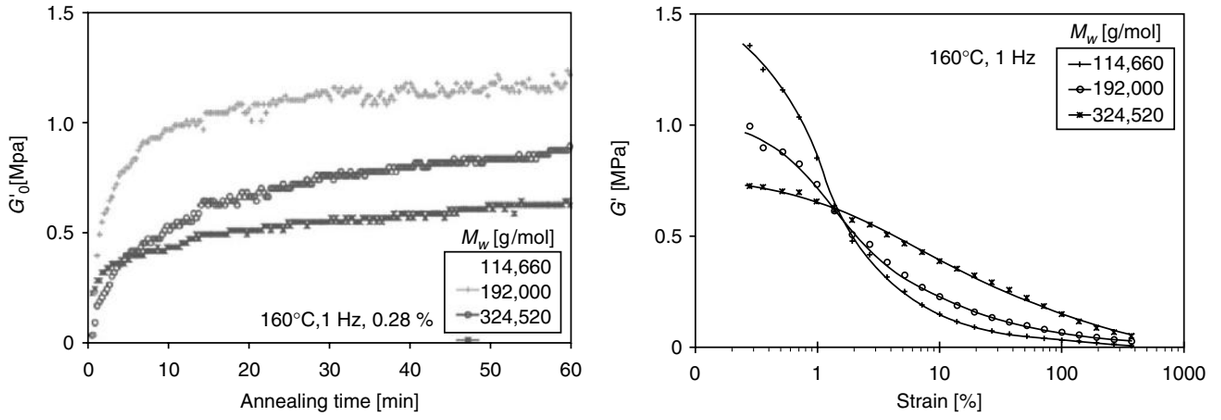

FIGURE 36.4. Flocculation behavior of the small strain modulus at 160°C of uncross-linked S-SBR-composites of various molar mass with 50 phr N234, as indicated (left) and strain dependence of the annealed samples after 60 min (right). Reproduced from M. Klüppel and G. Heinrich, *Kautschuk, Gummi, Kunstsoffe* **58**, 217–224 (2005) with permission from Hüthig.

and the observed dependency of the flocculation dynamics on the molar mass or the amount of bound rubber (Fig. 36.4), a model of filler–filler bonds in elastomers has been developed [16]. The morphological details of this model are shown schematically in Fig. 36.5.

In the framework of this approach, the mechanical stiffness of filler–filler bonds can be related to the remaining gap size between the filler particles that decreases during annealing (cross-linking) of filled rubbers. Consequently, stress between adjacent filler particles in a filler cluster is transmitted by nanoscopic, flexible bridges of glassy polymer, implying that a high flexibility and strength of filler clusters in elastomers is reached. This picture of filler–filler bonds allows for a qualitative explanation of the observed flocculation effects in Fig. 36.4 by referring to the amount of bound rubber and it is impact on the stiffness and strength of filler–filler bonds [16].

The flocculation results give strong evidence that kinetically aggregated filler clusters or networks are formed in elastomer composites, as shown schematically in Fig. 36.6. Accordingly, the model of rubber reinforcement by flexible filler clusters refers to the kinetic cluster–cluster aggregation (CCA) approach of filler networking in elastomers, which represents a reasonable theoretical basis for understanding the linear viscoelastic properties of reinforced rubbers. The CCA-model assumes that filler networks consists of a space-filling configuration of CCA-clusters with characteristic mass fractal dimension $d_f \approx 1.8$ and backbone dimension $d_{f,B} \approx 1.3$. A schematic view of this structure is shown on the right hand side of Fig. 36.6 ($\Phi > \Phi^*$). The mechanical response of this kind of filler networks depends mainly on the fractal connectivity of the CCA-clusters. It can be evaluated by referring to the Kantor-Webman model of flexible chain aggregates [19]. For the small strain modulus a power law behavior with filler concentration is predicted. The evaluated exponent $3 + d_{f,B}/(3 - d_f) \approx 3.5$ is in good agreement with the experimental data of Payne [20] for carbon black filled butyl rubber (Fig. 36.7). The predicted universal power-law behavior of the small strain modulus of filler reinforced rubbers is confirmed by a variety of experimental data, including carbon black and silica filled rubbers as well as composites with microgels (Fig. 36.8).

For a deeper understanding of the strongly nonlinear viscoelastic behavior of filler reinforced elastomers it is

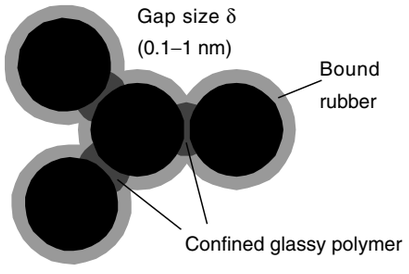

FIGURE 36.5. Schematic view of a small filler cluster in elastomers with stabilizing bound rubber and nanoscopic bridges of confined glassy polymer, implying the flexible properties of filler–filler bonds in a bulk rubber matrix. Reproduced from M. Klüppel and G. Heinrich, *Kautschuk, Gummi, Kunstsoffe* **58**, 217–224 (2005) with permission from Hüthig.

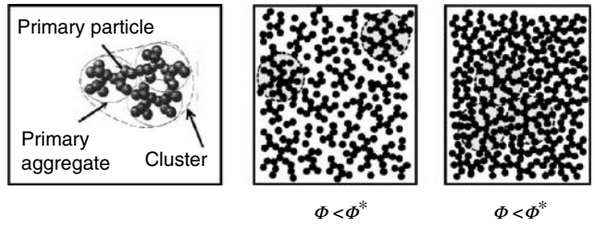

FIGURE 36.6. Schematic view of kinetically aggregated filler clusters in elastomers below and above the gel point Φ^*. The left side characterizes the local structure of carbon black clusters, build by primary particles and primary aggregates. (Every black disc in the center figure ($\Phi < \Phi^*$) and on the right hand side ($\Phi > \Phi^*$) represents a primary aggregate.) Reproduced from M. Klüppel and G. Heinrich, *Kautschuk, Gummi, Kunstsoffe* **58**, 217–224 (2005) with permission from Hüthig.

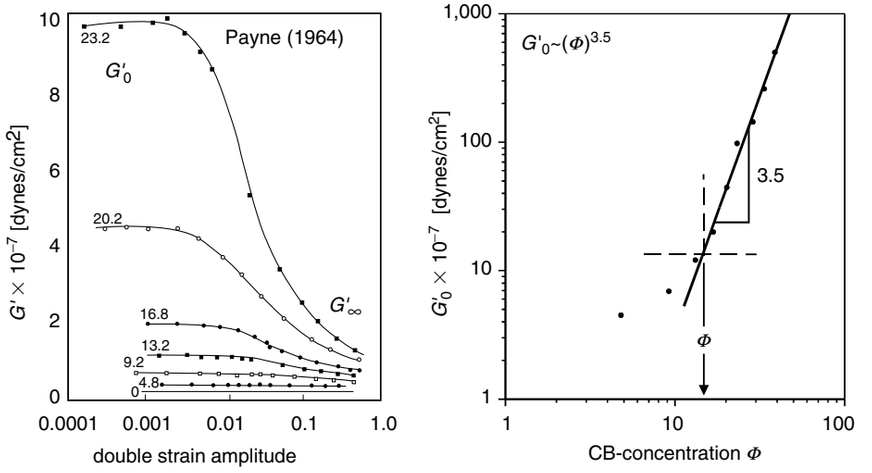

FIGURE 36.7. Payne effect of butyl composites with various amounts Φ of N330, as indicated (left) [19]. Scaling behavior of the small strain modulus of the same composites (right). Reproduced from M. Klüppel and G. Heinrich, *Kautschuk, Gummi, Kunstsoffe* **58**, 217–224 (2005) with permission from Hüthig.

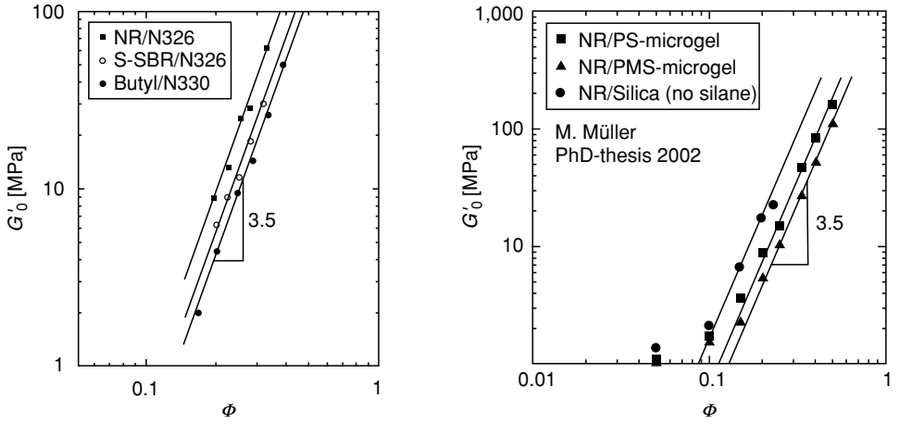

FIGURE 36.8. Scaling behavior of the small strain modulus of carbon black composites (left) and microgel or silica composites (right). In all cases an exponent close to 3.5 is found, indicating the universal character of the cluster–cluster aggregation model. Reproduced from M. Klüppel and G. Heinrich, *Kautschuk, Gummi, Kunstsoffe* **58**, 217–224 (2005) with permission from Hüthig.

necessary to consider the combined effect of immobilized polymer close to the filler interface (glassy layer) and the spatial arrangement of filler particles in the rubber matrix to form clusters [16]. A schematic view of the increased solid volume of a filler cluster due to an immobilized rubber layer is shown schematically in Fig. 36.9. The effect of a hard, glassy layer of immobilized polymer on the elastic modulus of CCA-clusters leads to the following power law dependency of the elastic storage shear modulus G′ on filler concentration Φ, particle size d, and layer thickness Δ [9]:

$$G' \cong G_p \left(\frac{(d+2\Delta)^3 - 6d\Delta^2}{d^3} \Phi \right)^{\frac{3+d_{f,B}}{3-d_f}}, \qquad (36.6)$$

where G_P is the averaged elastic bending–twisting modulus of different kinds of angular deformations of the cluster units, i.e., filler particles or bonds between filler particles. The exponent in Eq. (36.6) contains the fractal dimension d_f

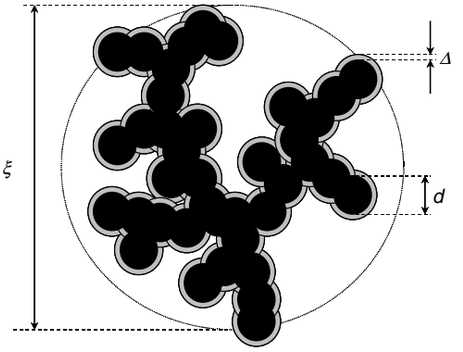

FIGURE 36.9. Schematic view of a filler cluster of size ξ in elastomers, consisting of particles (primary aggregates) of size d. The glassy layer of immobilized polymer attached to the filler surface with characteristic thickness Δ is indicated. Reproduced from G. Heinrich, M. Klüppel and T. A. Vilgis, Current Opinion in Solid State and Materials Science **6** 195–203 (2002) with permission from ELSEVIER.

of the filler cluster and the fractal dimension of its backbone $d_{f,B}$, respectively. This equation predicts a strong impact of the layer thickness Δ on the elastic modulus G′. Furthermore, the influence of particle size d becomes apparent. Using Eq. (36.6), a master procedure was applied for the small strain modulus of E-SBR samples with spherical microgel fillers of different size, yielding a layer thickness of $\Delta \sim 2$ nm [9].

Obviously, the value of G′ increases significantly if d becomes smaller, i.e., if the specific surface of the filler increases. Equation (36.6) describes the modulus G′ of the clusters as a local elastic bending–twisting term G_P times a scaling function that involves the size and geometrical structure of the clusters. Consequently, the temperature-or frequency dependency of G′ is controlled by the front factor G_P. As already pointed out, this local elastic constant is governed by the immobilized, glassy polymer between adjacent filler particles, implying that the temperature- or frequency dependence of G′ is given by that of the glassy polymer.

The model of glassy polymer bridges between adjacent filler particles of the filler network yields a physical understanding of the temperature dependence of Payne effect, i.e., the decrease of storage modulus with increasing strain amplitude. It is generally known that the amplitude of Payne effect, $G'_0 - G'_\infty$, decreases with increasing temperature. The low-strain modulus, G'_0, gradually decreases with the temperature whereas the high-strain modulus, G'_∞, remains roughly constant [9]. Hereby, two distinct mechanisms with different activation energies can be observed [21]. The low temperature one arises from the α-relaxation of the polymer which is confirmed by very large apparent activation energies, in agreement with the apparent activation energies associated to a glass transition. The high temperature one—well above the bulk glass transition temperature of the polymer system—gives activation energies in the order of ∼10 kJ/mol, which is within the range of physical (van der Waals) interactions.

In the following, we expect an Arrhenius-like temperature behavior for highly filled rubbers that is typically found for polymers in the glassy state. Therefore, we measure—far above the polymer bulk glass transition temperature—the modulus G′ for small deformation amplitudes (0.2% in our case). This is depicted schematically in Fig. 36.10. One obtains a straight line of slope E_A/R by plotting log G′(T) (or in the tensile mode log E′(T)) vs. 1/T well above the bulk glass–rubber transition region (i.e., in the range ∼20–100 °C) of the filled rubber sample. The quantity R being the gas constant.

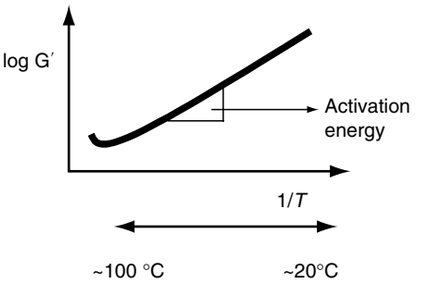

FIGURE 36.10. Schematic representation of the Arrhenius-like temperature dependency of G' and evaluation of the activation energy.

The estimation of the activation energy according to the described procedure was realized for a set of four differently filled rubber samples according to the design that is roughly sketched in Table 36.1. We note that the order of magnitude of activation energies in our systems are close to that generally presented in the literature [21].

Shore A hardness of all vulcanized samples was adjusted to approximately 70. Compounding, accelerated sulfur vulcanization and rubber physical testing was done according to standard procedures and will be described in a separate paper. As rubbers, we used standard emulsion polymerized styrene–butadiene copolymer (E-SBR 1500) and a solution polymerized styrene–butadiene copolymer (S-SBR) with a different amount of styrene and vinyl groups in comparison to the E-SBR. The used carbon black was N121 according ASTM classification. The used silica from Degussa AG was VN3 together with the coupling agent Si 69. All compounds contain a certain amount of an aromatic oil for reasons of processing. The temperature sweeps were performed with a dynamical testing device RDA from Rheometrics at frequency $f = 1$ Hz and at dynamical deformation of 0.2% in the shearing mode. The slope of the linear relation between log G' and the inverse temperature (corresponding to a temperature range T ∼ 20–80 °C) gives an estimate of the activation energy (Table 36.1). In both cases of polymers we find a lower value of the silica filled systems in comparison to the corresponding carbon black systems. Recently it was

TABLE 36.1. *Results on the variation of activation energy with filler- and polymer type, e.g., carbon black and silica filled E-SBR- and S-SBR-composites.*

Compound	E-SBR (phr)	S-SBR (phr)	Carbon black (phr)	Silica (phr)	E_A (kJ/mol)
1	100		80		13.3
2	100			80	10.2
3		100	80		12.5
4		100		80	9.3

found that the energies for silica systems were remarkably unrelated to the nature, amount and even presence of an interface agent [21].

36.4 THE DYNAMIC FLOCCULATION MODEL: STRESS SOFTENING AND FILLER INDUCED HYSTERESIS

The consideration of flexible chains of filler particles, approximating the elastically effective backbone of the filler clusters, allows for a micromechanical description of the elastic properties of tender CCA-clusters in elastomers. The main contribution of the elastically stored energy in the strained filler clusters results from the bending–twisting deformation of filler–filler bonds, which is taken into account by the elastic constant $\bar{G} = d^3 G_p$. For a consideration of filler network break-down with increasing strain, the failure properties of filler–filler bonds and filler clusters have to be evaluated in dependence of cluster size. This allows for a micromechanical description of tender but fragile filler clusters in the stress field of a strained rubber matrix [16]. A schematic view of the mechanical equivalence between a CCA-filler cluster and a series of soft and hard springs is presented in Fig. 36.11. The two springs with force constants k_s and k_b correspond to bending–twisting- and tension deformations of the filler–filler bonds with elastic constants $\bar{G}$ and Q, respectively.

The dynamic flocculation model of stress softening and filler induced hysteresis assumes that the breakdown of filler clusters during the first deformation of the virgin samples is totally reversible, though the initial virgin state of filler–filler bonds is not recovered. This implies that, on the one side, the fraction of rigid filler clusters decreases with increasing prestrain, leading to the pronounced stress softening after the first deformation cycle. On the other side, the fraction of already damaged, fragile filler clusters increases with increasing prestrain, which impacts the filler-induced hysteresis [16]. A schematic representation of the decomposition of filler clusters in rigid and fragile units for preconditioned samples is shown in Fig. 36.12.

By assuming a specific cluster size distribution $\phi(\xi_\mu)$ in reinforced rubbers, a constitutive material model of filler reinforced rubbers can be derived. As considered more closely in [16] or [22], this model is based on a nonaffine tube model of rubber elasticity, including hydrodynamic amplification of the rubber matrix by a fraction of rigid filler clusters with filler–filler bonds in the unbroken, virgin state. The filler-induced hysteresis is described by an anisotropic free energy density, considering the cyclic breakdown and reaggregation of the residual fraction of more soft, fragile filler clusters with already broken (damaged) filler–filler bonds. Accordingly, the free energy density of filler reinforced rubber consists of two contributions:

$$W(\varepsilon_\mu) = (1 - \Phi_{\text{eff}}) W_R(\varepsilon_\mu) + \Phi_{\text{eff}} W_A(\varepsilon_\mu). \tag{36.7}$$

The first addend is the equilibrium energy density stored in the extensively strained rubber matrix, including hydrodynamic reinforcement by a fraction of rigid filler clusters. The second addend considers the energy stored in the strained filler clusters (see below). The free energy density of the nonaffine tube model of rubber elasticity reads

$$W_R(\varepsilon_\mu) = \frac{G_c}{2}\left\{\frac{\left(\sum_{\mu=1}^{3}\lambda_\mu^2 - 3\right)\left(1 - \frac{T_e}{n_e}\right)}{1 - \frac{T_e}{n_e}\left(\sum_{\mu=1}^{3}\lambda_\mu^2 - 3\right)} + \ln\left[1 - \frac{T_e}{n_e}\left(\sum_{\mu=1}^{3}\lambda_\mu^2 - 3\right)\right]\right\} + 2G_e\left(\sum_{\mu=1}^{3}\lambda_\mu^{-1} - 3\right). \tag{36.8}$$

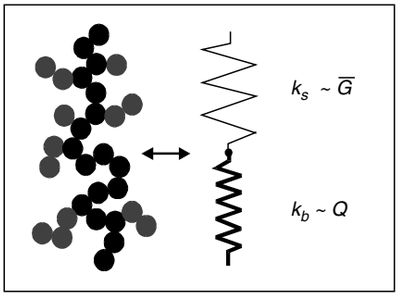

FIGURE 36.11. Schematic view demonstrating the mechanical equivalence between a filler cluster and a series of soft and stiff molecular springs, representing bending-twisting-, and tension deformation of filler–filler bonds, respectively.

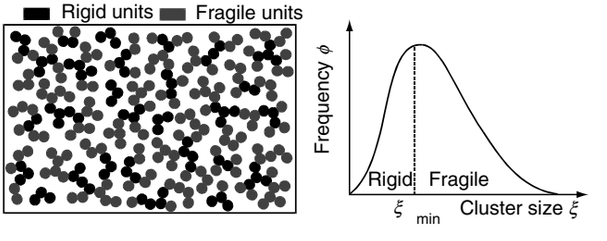

FIGURE 36.12. Schematic view of the decomposition of filler clusters in rigid and fragile units for preconditioned samples. The right side shows the cluster size distribution with the prestrain dependent boundary size ξ_{min}.

Here, n_e is the number of statistical chain segments between two successive entanglements and T_e is the trapping factor ($0 < T_e < 1$), characterizing the portion of elastically active entanglements. The first bracket term of Eq. (36.8) considers the constraints due to interchain junctions, with an elastic modulus G_c proportional to the density of network junctions. The second addend is the result of tube constraints, whereby G_e is proportional to the entanglement density of the rubber. The parenthetical expression in the first addend considers the finite chain extensibility of polymer networks by referring to a proposal of Edwards and Vilgis [23]. For the limiting case $n_e/T_e = \Sigma\lambda_\mu^2 - 3$, a singularity is obtained for the free energy W_R, indicating the maximum strain of the network, which is reached when the chains between successive trapped entanglements are fully stretched out. In the limit $n_e \to \infty$ the original Gaussian formulation of the nonaffine tube model, derived by Heinrich et al. [24] for infinite long chains, is recovered.

The presence of rigid filler clusters, with bonds in the virgin, unbroken state of the sample, give rise to hydrodynamic reinforcement of the rubber matrix. This is specified by the strain amplification factor f, which relates the external strain ε_μ of the sample to the internal strain ratio λ_μ of the rubber matrix (Eq. (36.5)). In the case of a preconditioned sample and for strains smaller than the previous straining ($\varepsilon_\mu < \varepsilon_{\mu,\max}$), the strain amplification factor f is independent of strain and determined by $\varepsilon_{\mu,\max}(f = f(\varepsilon_{\mu,\max}))$. For the first deformation of virgin samples it depends on the external strain ($f = f(\varepsilon_\mu)$). By applying a relation derived by Huber and Vilgis [25,26] for the amplification factor of overlapping fractal clusters, $f(\varepsilon_{\mu,\max})$ or $f(\varepsilon_\mu)$ can be evaluated by averaging over the size distribution of rigid clusters in all space directions. In the case of preconditioned samples this yields

$$f(\varepsilon_{\mu,\max}) = 1 + c\Phi_{\text{eff}}^{\frac{2}{3-d_f}} \sum_{\mu=1}^{3} \frac{1}{d} \left\{ \int_0^{\xi_{\mu,\min}} \left(\frac{\xi'_\mu}{d}\right)^{d_w - d_f} \phi(\xi'_\mu)\mathrm{d}\xi'_\mu + \int_{\xi_{\mu,\min}}^{\infty} \phi(\xi'_\mu)\mathrm{d}\xi'_\mu \right\}, \tag{36.9}$$

where c is a constant of order one and Φ_{eff} is the effective filler volume fraction of the structured filler particles, i.e., primary aggregates of carbon black or silica. ξ_μ is the cluster size, d is the particle size, $\phi(\xi_\mu)$ is the normalized size distribution, $d_f \approx 1.8$ is the mass fractal dimension and $d_w \approx 3.1$ is the anomalous diffusion exponent on fractal CCA-clusters [18].

The second addend in Eq. (36.7) considers the energy stored in the substantially strained fragile filler clusters

$$W_A(\varepsilon_\mu) = \sum_{\mu}^{\varepsilon_\mu/\partial t>0} \frac{1}{2d} \int_{\xi_{\mu,\min}}^{\xi_\mu(\varepsilon_\mu)} G_A(\xi'_\mu)\varepsilon_{A,\mu}^2(\xi'_\mu,\varepsilon_\mu)\phi(\xi'_\mu)\mathrm{d}\xi'_\mu, \tag{36.10}$$

where G_A is the elastic modulus and $\varepsilon_{A,\mu}$ is the strain of the fragile filler clusters in spatial direction μ. The dependency of these quantities on cluster size ξ and external strain ε_μ can be derived from basic micromechanical considerations about elasticity and fracture mechanics of tender filler clusters imbedded into a strained rubber matrix. This also allows for a specification of the strain dependent integral boundaries $\xi_\mu = \xi_\mu(\varepsilon_\mu)$ and $\xi_{\mu,\min} = \xi_\mu(\varepsilon_{\mu,\max})$. A detailed presentation of the morphological and mechanical properties of filler clusters in elastomers is found in [16].

It is demonstrated in Fig. 36.13 that the quasistatic stress–strain data (up-cycles) at different prestrains of silica filled rubbers can be well described in the scope of the above dynamic flocculation model of stress softening and filler-induced hysteresis up to large strain. Thereby, the size distribution $\phi(\xi_\mu)$ has been chosen as an isotropic logarithmic normal distribution ($\phi(\xi_1) = \phi(\xi_2) = \phi(\xi_3)$)

$$\phi(x_\mu) = \frac{\exp\left(-\frac{\ln(x_\mu/x_0)^2}{2b^2}\right)}{\sqrt{\pi/2}bx_\mu} \quad \mu = 1,2,3 \tag{36.11}$$

with the mean cluster size $x_0 \equiv \xi_0/d$ and distribution width b. A similar good agreement between experimental data and simulation as shown in Fig. 36.13 can be obtained for carbon black filled elastomers and for biaxial tension data [16]. The obtained microscopic material parameter appear reasonable, providing information on the mean cluster size ξ_0 and distribution width b, the tensile strength of filler–filler bonds Q_{ε_b}/d^3 and the polymer network chain density $\nu_c(\nu_c \sim G_c)$.

Beside the characteristic stress softening up to large strains (Mullins effect) as shown in Fig. 36.13, the model also considers the hysteresis behavior of reinforced rubbers (Payne effect). Obviously, since the sum in Eq. (36.10) is taken over stretching directions with $\partial\varepsilon/\partial t > 0$, only, up- and down cycles are described differently. An example considering a fit of the hysteresis cycles of silica filled EPDM rubber in the medium strain regime up to 50% is shown in Fig. 36.14. For these adaptations an alternative form of the cluster size distribution has been assumed, which allows for an analytical solution of the integrals in Eqs. (36.9) and (36.10):

$$\phi(x_\mu) = \frac{4x_\mu}{x_0} \exp\left(-\frac{2x_\mu}{x_0}\right) \quad \mu = 1,2,3. \tag{36.11'}$$

It must be noted that the topological constraint modulus G_e has been considered as a fixed parameter in the simulations shown in Figs. 36.11 and 36.12 and was not used as a fitting parameter. The chosen values $G_e = 0.2$ MPa and $G_e = 0.6$ MPa correspond to the known entanglement densities of the

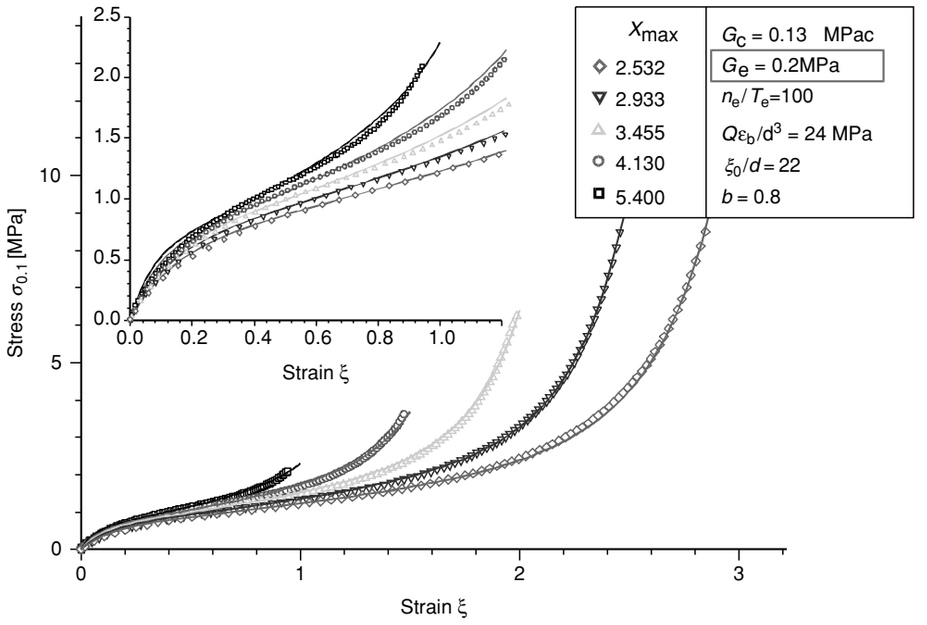

FIGURE 36.13. Uniaxial stress–strain data of S-SBR samples with 60 phr silica at different prestrains $\varepsilon_{max} = 100$, 150, 200, 250, and 300% (symbols) and fittings (lines) with the stress softening model Eqs. (36.7)–(36.11). The fitting parameters are indicated. The insert shows a magnification of the small strain data.

S-SBR- and EPDM rubber matrix, respectively, which is about three times larger in the case of EPDM.

In particular it can be shown that the dynamic flocculation model of stress softening and hysteresis fulfils a ''plausibility criterion'', important e.g., for finite element (FE) applications. Accordingly, any deformation mode can be predicted based solely on uniaxial stress–strain measurements, which can be carried out relatively easily. From the simulations of stress–strain cycles at medium and large strain it can be concluded that the model of cluster breakdown and reaggregation for prestrained samples represents a fundamental micromechanical basis for the description of nonlinear viscoelasticity of filler reinforced rubbers. Thereby, the mechanisms of energy storage and dissipation are traced back to the elastic response of tender but fragile filler clusters [16].

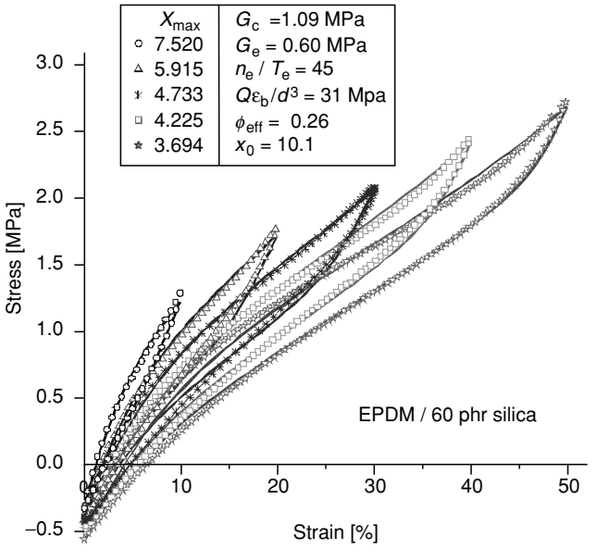

FIGURE 36.14. Uniaxial stress–strain cycles of EPDM samples with 60 phr silica at different prestrains $\varepsilon_{max} = 10$, 20, 30, 40, and 50% (symbols) and fittings (lines) with the stress softening model Eqs. (36.7)–(36.10). Here, the cluster size distribution Eq. (36.11) has been used. The obtained fitting parameters are listed in the insert.

36.5 SUMMARY AND CONCLUSIONS

During dynamic-mechanical deformation at certain (high) frequencies the silica systems are dynamically softer. This is related to ''dynamically softer'' hinge-like filler–filler interactions via the partially immobilized rubbery interfacial layers between neighboring silica aggregates within the agglomerates or the (infinite) filler network, respectively. Figure 36.3 demonstrates the structure of filler–filler bonds in a bulk rubber matrix. The gap size of neighboring filler particles with confined glassy polymer and the bound rubber layer, governing the stiffness and strength of filler–filler bonds are indicated. In general, the black discs represent primary carbon black aggregates. The finding that the silica systems are dynamically softer might explain an improved (dynamical) interlocking between

sliding tire tread rubber materials and rough road surfaces during ABS-braking on wet road surfaces where the braking process leads to a high frequency (kHz–MHz range) dynamic-mechanical deformation of the tread rubber material [10]. As a practical result, an improved wet skid performance of passenger car tires is expected with the silica technology [10].

A deeper understanding of molecular mechanisms of filler flocculation and reinforcement by active fillers like carbon black or silica represent a fundamental tool for problem solving in engineering praxis. In particular, the implementation of micromechanical models into FE-codes will open a new way for more precise simulations of the dynamic deformation and damping behavior of rubber goods, including stress softening effects and filler induced hysteresis. Even investigations and simulations of the filler cluster kinetics are of increasing interest [27,28]. This might be useful for a better understanding and prediction of complex time-dependent rubber deformations like, for example, tire tread deformations under combined driving and cornering conditions.

ACKNOWLEDGMENTS

The authors are indebted to Dr J. Meier (DIK) and Dr J. Schramm (Continental AG) for the fruitful cooperation and to the DFG (FOR 492) for financial support.

REFERENCES

1. G. Heinrich, M. Klüppel, T. A. Vilgis, Curr. Opin. Solid State Mater. Sci. **6**, 195 (2002).
2. A. Medalia, Rubber Chem. Technol. **51**, 437 (1978).
3. L. Mullins, N. R. Tobin, Rubber Chem. Technol. **39**, 799 (1966).
4. S. Westermann, M. Kreitschmann, W. Pyckhout-Hintzen, D. Richter, E. Straube, B. Farago, G. Goerigk, Macromolecules **32**, 5793 (1999).
5. G. Huber, T. A. Vilgis, Macromolecules **35**, 9204 (2002).
6. S. Westermann, W. Pyckhout-Hintzen, M. Kreitschmann, D. Richter, E. Straube, "Microscopic Deformations in Filled Polymer Networks", Proceedings Kautschuk-Herbst-Kolloquium 2002, Hannover (FRG), 99–107, 30 October–1 November 2002.
7. S. Vieweg, R. Unger, E. Hempel, E. Donth, J. Non-Cryst. Solids **235/237**, 470 (1998).
8. A. Botti, W. Pyckhout-Hintzen, D. Richter, E. Straube, V. Urban, J. Kohlbrecher, Physica B **276–278** (2000), 371; A. Botti, W. Pyckhout-Hintzen, D. Richter, E. Straube, Physica A **304**, 230 (2002); A. Botti, Microscopic deformations in filled networks. PhD thesis, University Muenster, Germany, 2001.
9. G. Heinrich, M. Klüppel, Adv. Polym. Sci. **160**, 1 (2002).
10. G. Heinrich, J. Schramm, A. Müller, M. Klüppel, N. Kendziorra, S. Kelbch, "Zum Einfluss der Straßenoberflächen auf das Bremsverhalten von Pkw-Reifen beim ABS-nass und ABS-trocken Bremsvorgang", Fortschritt-Berichte VDI, Reihe 12 (Verkehrstechnik/Fahrzeugtechnik), 69–86, 2002, Nr. 511.
11. M. J. Wang, Rubber Chem. Technol. **71**, 520 (1998).
12. H. Montes, F. Lequeux, J. Berriot, Macromolecules **36**, 8107 (2003).
13. J. Berriot, F. Lequeux, L. Monnerie, H. Montes, D. Long, P. Sotta, J. Non-Cryst. Solids **310**, 719 (2002).
14. J. Berriot, H. Montes, F. Lequeux, D. Long, P. Sotta, Macromolecules **35**, 9756 (2002); ibid. Europhys. Lett. **64**, 50 (2003).
15. G. Migliorini, V.G. Rostiashivili, T.A. Vilgis, Eur. Phys. J. **B33**, 61 (2003).
16. M. Klüppel, Adv. Polym. Sci. **164**, 1–86 (2003).
17. M. Klüppel and G. Heinrich, Rubber Chem. Technol. **68**, 623 (1995).
18. M. Klüppel, R.H. Schuster and G. Heinrich, Rubber Chem. Technol. **70**, 243 (1997).
19. Y. Kantor and I. Webman, Phys. Rev. Lett. **52**, 1891 (1984).
20. A.R. Payne, J. Appl. Polym. Sci. **8**, 2661 (1964).
21. L. Ladouce, Y. Bomal, L. Flandin, D. Labarre, "Dynamic mechanical properties of precipitated silica filled rubber: Influence of morphology and coupling agent", Paper No. 33, 157th meeting of the Rubber Division, American Chemical Society, Dallas, Texas, April 4–6, 2000.
22. M. Klüppel and J. Schramm, Macromol. Theory Simul. **9**, 742 (2000).
23. S.F. Edwards and T.A. Vilgis, Rep. Prog. Phys. **51**, 243 (1988); Polymer **27**, 483 (1986).
24. G. Heinrich, E. Straube, G. Helmis, Adv. Polym. Sci. **85**, 33 (1988).
25. G. Huber, PhD-Thesis, University Mainz, Germany (1997).
26. G. Huber and T.A. Vilgis, Euro. Phys. J. **B3**, 217 (1998); ibid. Kautschuk Gummi Kunstst. **52**, 102 (1999).
27. G. Heinrich, V. Härtel, J. Tschimmel, M. Klüppel, "Kinetics of filler structures in reinforced polymer networks", in Michler, G.H. (Hrsg.): Polymeric Materials 2004 (Halle/Saale, 29.09. – 01.10.2004), A17.
28. G. Heinrich, F.R. Costa, M. Abdel-Goad, U.Wagenknecht, B. Lauke, V. Härtel, J. Tschimmel, M. Klüppel, and A.L. Svistkov, Kautschuk, Gummi, Kunstst. **58**, 163 (2005)